

DCO⁺ and DCN 1-0 survey toward a sample of Planck cold clumps

Fu Mo¹, Junzhi Wang¹, Shu Liu², Yan Duan^{3,2}, Huanxue Feng⁴, Yuqiang Li^{5,6}, Zhe Lu^{1,7}, Rui Luo¹, Chao Ou¹, Yani Xu¹, and Zhuoying Yan¹

¹ Guangxi Key Laboratory for Relativistic Astrophysics, School of Physical Science and Technology, Guangxi University, Nanning 530004, People's Republic of China

e-mail: junzhiwang@gxu.edu.cn

² National Astronomical Observatories, Chinese Academy of Sciences, Beijing 100101, People's Republic of China

³ Space Engineering University, Beijing 101416, People's Republic of China

⁴ School of Physics and Astronomy, Sun Yat-sen University, Zhuhai, 519082, People's Republic of China

⁵ Shanghai Astronomical Observatory, Chinese Academy of Sciences, No. 80 Nandan Road, Shanghai, 200030, People's Republic of China

⁶ School of Astronomy and Space Sciences, University of Chinese Academy of Sciences, No. 19A Yuquan Road, Beijing 100049, People's Republic of China

⁷ Department of Electrical and Electronic Engineering, Guilin University of Technology at Nanning, Nanning 530001, People's Republic of China

Received xx; accepted xx

ABSTRACT

Context. Deuterated molecules can be used to study the physical conditions and the astro-chemical evolution of molecular clouds.

Aims. large-sample surveys for deuterated molecules are needed to understand the enhancement of deuterated molecules from diffuse molecular gas to cold cores.

Methods. A single-pointing survey toward the 559 Planck cold clumps of the Early Cold Core Catalogue (ECC) has been conducted using the Arizona Radio Observatory 12-meter telescope, focusing on the $J=1-0$ transitions of DCO⁺ and DCN. The survey included observations of 309 cores for DCO⁺ and DCN 1-0 simultaneously, followed by 71 of these cores where DCO⁺ 1-0 was detected for H¹³CO⁺ and H¹³CN 1-0 simultaneously, aiming to determine the deuterated fraction (D_{frac}). Additionally, 250 cores were observed for DCO⁺, DCN, H¹³CO⁺ and H¹³CN 1-0 simultaneously.

Results. Among the 309 sources, DCO⁺ and DCN 1-0 were detected in 79 and 11 sources, with a detection rates of 25.6% and 3.6% respectively. In the 250 sources observed for all four species, DCO⁺, DCN, H¹³CO⁺ and H¹³CN 1-0 were detected in 58, 9, 57 and 13 sources, with a detection rate of 23.2%, 3.6%, 22.8% and 5.2% respectively. The $D_{\text{frac}}(\text{HCO}^+)$ values in 112 sources range from 0.89% to 7.4% with a median value of 3.1%, while $D_{\text{frac}}(\text{HCN})$ values in 11 sources range from 1.5% to 5.5% with a median value of 2.3%. The line widths of DCO⁺ and H¹³CO⁺ 1-0 detections are mostly within 1 km s⁻¹.

Conclusions. The similarity in D_{frac} values between HCO⁺ and HCN indicates that the higher detection rate of DCO⁺ 1-0 compared with DCN 1-0 is due to the lower critical density of DCO⁺ 1-0. We suggest that the enhancement of DCO⁺ and DCN likely begins in the early diffuse stage of the molecular cloud, rather than during the cold core formation stage.

Key words. methods: observational – ISM: abundances – ISM: clouds – ISM: molecules – radio lines: ISM

1. Introduction

Deuterated molecules are useful tools for studying the physical conditions and astro-chemical evolution of molecular clouds (Roberts et al. 2002; Guilloteau et al. 2006). Deuterium fractionation, i.e., the abundance ratios of deuterated molecules to their hydrogenated counterparts are much enhanced over the cosmic D/H elemental abundance ratio $\sim 1.5 \times 10^{-5}$ (Roberts & Millar 2000). Due to the lower zero-point energy of deuterated molecules compared to their non-deuterated counterparts which ensures that deuterium is preferentially bonded into molecules compared to hydrogen, deuterated molecules can be synthesized effectively in the cold gas phase during the early stage of the evolution of molecular clouds (Roberts & Millar 2000). The process of deuterium fractionation is sensitive to various physical conditions such as temperature, density, CO depletion (Millar et al. 1989; Feng et al. 2020), ionization (Caselli 2002), etc., with low temperatures and high densities having particularly significant effects (Fontani et al. 2011; Pillai et al. 2011). Therefore,

deuterated molecules are considered as excellent tracers for cold ($T \sim 10$ K) and dense ($n \geq 10^4$ cm⁻³) regions within molecular clouds (Roberts & Millar 2007).

After the detection of DCN in the Orion Nebula molecular cloud (Jefferts et al. 1973), many other deuterated species have been identified in molecular clouds over the past decades. These include DCO⁺ (Hollis et al. 1976; Tiné et al. 2000; Caselli 2002), DNC (Snell & Wootten 1977; van der Tak et al. 2009; Yang et al. 2024), N₂D⁺ (Snyder et al. 1977; Crapsi et al. 2005; Fontani et al. 2006), deuterated NH₃ (Turner et al. 1978; Roueff et al. 2005; Pillai et al. 2007; Li et al. 2022), and deuterated H₂CO (Watson et al. 1975; Roberts et al. 2002; Roberts & Millar 2007). Among these deuterated molecules, DCO⁺ and DCN are particularly valuable for studying the physical conditions and astro-chemical evolution of molecular clouds. This is due to their relatively high abundances, simple rotational spectra, accessible rotational transitions (Yang et al. 2024), and their synthetic pathways, which are closely linked to the deuterium fractionation process (Millar et al. 1989). Observational studies (Watson 1973; Roberts

et al. 2002; Feng et al. 2020) and theoretical models (Herbst 1982; Millar et al. 1989) of deuterium chemistry suggest that DCO⁺ and DCN are important for understanding the evolution of molecular cloud.

The deuterated fraction (D_{frac}) is defined as the abundance ratio of a deuterated molecule to its hydrogenated counterpart. This ratio has been studied for many deuterated species (Hirota et al. 2001; Turner 2001; Caselli 2002; Roberts et al. 2002), including DCO⁺ and DCN. DCO⁺ was first detected in the molecular clouds NGC 2264 and DR (OH) with H¹³CO⁺/DCO⁺ abundance ratios of 0.54 and 1.18 (Hollis et al. 1976). The DCO⁺/HCO⁺ ratio was found to be ~ 0.18 in the dark cloud L134N and 0.02 in TMC1-N (Tin   et al. 2000). For massive starless clump candidates, the DCO⁺/HCO⁺ and DCN/HCN ratios were estimated to be 0.011-0.040 and 0.004-0.045, respectively (Yang et al. 2024). The DCN/HCN ratio increases from 0.001 in the hot core gas close to the infrared source IRc2 to values of 0.01-0.06 in the OMC-1 ridge region (Schilke et al. 1992). The abundance of deuterated molecules is considered crucial for understanding both the physical conditions and deuterium chemistry in the cold gas phase of molecular clouds.

However, large-sample surveys of DCO⁺ and DCN lines toward cold dense cores are still lacking in the literature. This gap limits our understanding of the enhancement of deuterated molecules in the phase from diffuse molecular gas to cold cores, including the measurements of D_{frac} for these molecules. The Planck cold clumps from the Early Cold Core Catalogue (ECC), which were selected from Wu et al. (2012), lack feedback from star formation, represent some of the most quiescent regions, and are ideal for such large-sample surveys. These Planck cold clumps have a typical mass of $\sim 5 M_{\odot}$, a size of ~ 0.5 pc (Planck Collaboration et al. 2016), and an excitation temperature of ~ 10 K (Wu et al. 2012).

In this paper, we present a single-pointing survey of DCO⁺ and DCN 1-0 toward the 559 Planck cold clumps observed to date. The observational details are described in Section 2, the results are presented in Section 3, and the discussion and summary are provided in Section 4 and Section 5 respectively.

2. Observations

In total, 559 sources selected from the 674 Planck cold clumps with CO line detections (Wu et al. 2012) were observed using the Arizona Radio Observatory (ARO) 12-meter telescope in 2020 and 2023. Among the 559 observed sources, the masses of 83 sources can be found from Planck Collaboration et al. (2016), with mass values ranging from 0.29 to $1.85 \times 10^4 M_{\odot}$. There are 75 sources with masses below $100 M_{\odot}$, 6 sources with masses between 100 and $1000 M_{\odot}$, and only 2 sources with masses exceeding $1000 M_{\odot}$. The kinematic distances of these 559 sources range from 0.10 to 21.58 kpc, while the excitation temperatures derived from CO 1-0 ($T_{\text{ex}}(\text{CO})$ hereafter) range from 3.9 to 27.1 K (Wu et al. 2012). The beam size at 72 GHz is $\sim 87''$. The focus was checked at the beginning of each observing block. Pointing was checked every two hours on a nearby quasar or planet. The main beam brightness temperature (T_{mb}) is calculated from $T_{\text{A}}^* = T_{\text{mb}} \times \eta$, where T_{A}^* is the antenna temperature and η is the average beam efficiency of the 4 mm receiver, with a value of 0.92 ± 0.06 .

In early 2020, 258 sources were observed in DCO⁺ and DCN 1-0 using the 4 mm receiver (66-90 GHz) with dual polarizations and ARO Wideband Spectrometer (AROWS) with mode 3, which provides 78.125 kHz channel spacing (~ 0.32 km s⁻¹ at 72GHz) and 500 MHz bandwidth, covering DCO⁺ 1-0 at

72.039312 GHz and DCN 1-0 at 72.414927 GHz simultaneously. Due to the limited velocity resolution of ~ 0.32 km s⁻¹ with AROWS mode 3, accurate measurements of full width at half maximum (FWHM) for sources with narrow line widths were challenging. To address this, high spectral resolution supplementary observations were conducted for 32 sources with narrow DCO⁺ 1-0 lines using AROWS mode 5, which provides 19.531 kHz channel spacing (~ 0.081 km s⁻¹ at 72 GHz) and 125 MHz bandwidth. To derive D_{frac} , 41 sources with DCO⁺ 1-0 detections were observed for H¹³CO⁺ 1-0 at 86.754288 GHz and H¹³CN 1-0 at 86.3401764 GHz simultaneously, using AROWS mode 3 with a velocity resolution ~ 0.27 km s⁻¹ at 86 GHz. Standard position switching mode was used with 3 minutes on and 3 minutes off for each source. The typical system temperatures (T_{sys}) were 150 K at 72 GHz and 120 K at 86 GHz, resulting in a root-mean-square (rms) noise level of ~ 50 mK at 78.125 kHz channel spacing for the final spectrum after averaging both polarizations.

In 2023, 51 sources were observed for DCO⁺ and DCN 1-0, with 30 sources additionally observed for H¹³CO⁺ and H¹³CN 1-0, using the same setup as in 2020.

In 2023, 250 sources were observed using the 4 mm receiver and the newly updated AROWS multi-window mode 13, which provides up to eight spectral windows of the same size with 19.53 kHz channel spacing (~ 0.081 km s⁻¹ at 72 GHz) and 40 MHz bandwidth. This setup covers DCO⁺ and DCN 1-0 in the lower sideband (LSB) and H¹³CO⁺ and H¹³CN 1-0 in the upper sideband (USB) simultaneously. The standard position switching mode was used with 30 seconds on and 30 seconds off, repeating 6 times for each source. The typical T_{sys} values are 150 K at 72 GHz and 120 K at 86 GHz, resulting in an rms noise level of ~ 100 mK at 19.53 kHz channel spacing for the final spectrum after averaging both polarizations. In observations using AROWS mode 13 in 2023, due to a software bug in the multi-window configuration code during shared risk period for the wrong sign of Doppler correction for the second sideband, even though all the parameters obtained for the lines in the first sideband, which is the LSB including DCO⁺ and DCN 1-0, the H¹³CO⁺ and the V_{LSR} measurements of H¹³CN 1-0 in USB exhibit offsets of 1 to 7 km s⁻¹, while all the other parameters are right. Therefore, the V_{LSR} values of H¹³CO⁺ and H¹³CN 1-0 are not provided in Section 3 and not used for scientific discussions.

Data reduction was performed using the CLASS package in GILDAS¹ software. After checking each scan, bad scans (fewer than 3%) were discarded. A first-order baseline was applied to all spectral lines, and a single-component Gaussian fitting was applied to obtain parameters, including velocity-integrated intensity ($\int T_{\text{mb}} dv$ denoted as W hereafter), V_{LSR} and FWHM for each source.

3. Results

Sources considered with detections were judged by W greater than 3σ , where both W and σ were obtained from the Gaussian fitting in CLASS. W of the DCO⁺ 1-0 line is denoted as $W(\text{DCO}^+)$ hereafter, with analogous notation applied to the DCN, H¹³CO⁺, and H¹³CN 1-0 lines. Examples of detections for the DCO⁺ and DCN 1-0 lines toward G091.73+04.3 observed in 2020 using the low velocity resolution mode (AROWS mode 3), are shown in Figure 1. While detections toward G159.21-20.1 observed in 2023 using high resolution mode (AROWS mode 13), are shown in Figure 2. Since each source was observed for

¹ <http://www.iram.fr/IRAMFR/GILDAS>

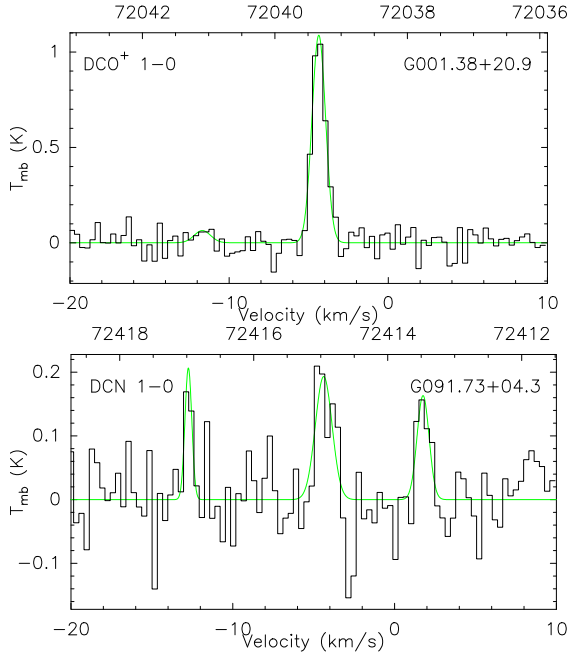


Fig. 1: Spectral lines of DCO⁺ and DCN 1-0 (black line) overlaid with Gaussian fitting results (green line) toward G091.73+04.3, observed in 2020 using the low velocity resolution mode (AROWS mode 3) with velocity resolution ~ 0.32 km s⁻¹. The hyperfine components of DCN 1-0 are visible.

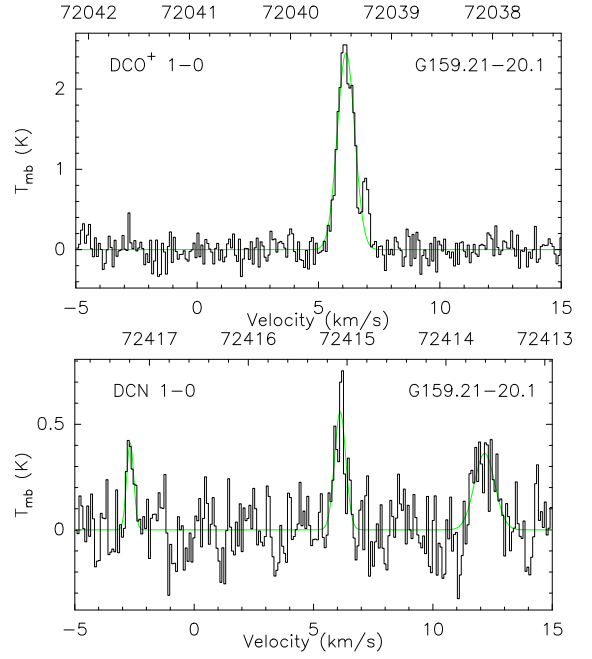


Fig. 2: Spectral lines of DCO⁺ and DCN 1-0 (black line) overlaid with Gaussian fitting results (green line) toward G159.21-20.1, observed in 2023 using the high velocity resolution mode (AROWS mode 13) with velocity resolution ~ 0.081 km s⁻¹. The hyperfine components of DCN 1-0 are visible.

approximately the same duration of six minutes, the noise levels of the spectra are similar, though the different rms levels are caused by different velocity resolution. DCN and H¹³CN $J=1-0$ exhibit hyperfine splitting into $F=1-0$, $2-1$, and $0-0$ components, with $F=2-1$ being the strongest. For the results and discussion in this paper, $J=1-0$, $F=2-1$ lines of DCN and H¹³CN are focused on, which are written as DCN 1-0 and H¹³CN 1-0 hereafter.

3.1. Detection rates of DCO⁺, DCN, H¹³CO⁺ and H¹³CN 1-0

Using the low velocity resolution mode (AROWS mode 3), DCO⁺ and DCN 1-0 were detected in 79 and 11 out of 309 sources with detection rates of 25.6% and 3.6%, respectively. Using the high velocity resolution mode (AROWS mode 13), DCO⁺, DCN, H¹³CO⁺, and H¹³CN 1-0 were detected in 58, 9, 57, and 13 out of 250 sources with detection rates of 23.2%, 3.6%, 22.8% and 5.2%, respectively. The detection rates of DCO⁺ and DCN 1-0 are similar between the two AROWS modes. Overall, the detection rates for DCO⁺ and DCN 1-0 are 24.5% and 3.6%, with detections in 137 and 20 out of 559 sources, respectively. The detection rates are summarized in Table 1. The detailed detection status is presented in Table 2.

Among the 250 sources observed with the high velocity resolution mode (AROWS mode 13), the detection rates of DCO⁺ and H¹³CO⁺ 1-0 are similar, and detections of these two lines occurred simultaneously in most sources. There are 46 sources where both DCO⁺ and H¹³CO⁺ 1-0 were detected, with a median $W(\text{DCO}^+)$ of 6.0σ and a median $W(\text{H}^{13}\text{CO}^+)$ of 7.0σ . While 12 sources showed detections of DCO⁺ 1-0 only, with a median $W(\text{DCO}^+)$ of 4.0σ . These sources include G168.85-15.8, G161.85-08.6, G163.32-08.4, G165.69-09.1, G178.48-06.7, G195.00-16.9, G177.14-01.2, G200.34-10.9, G185.33-02.1, G181.84+00.3, G199.88+00.9, and G201.13+00.3. There were 11 sources with only H¹³CO⁺ 1-0 detections, suggest-

ing that deuterium enhancement may not occur, with median a $W(\text{H}^{13}\text{CO}^+)$ of 6.6σ . These sources are G159.23-34.4, G162.64-31.6, G168.00-15.6, G170.13-16.0, G170.99-15.8, G165.16-07.5, G195.09-16.4, G159.34+11.2, G191.00-04.5, G215.00-15.1, and G216.18-15.2.

3.2. Derived parameters of detected DCO⁺ and DCN 1-0

The parameters for sources with DCO⁺ 1-0 detections are listed in Table 3, while those with DCN 1-0 detections are in Table 4. DCO⁺ and DCN 1-0 were detected in 137 and 20 out of 559 sources, respectively. There were 16 sources with detections of both DCO⁺ and DCN 1-0, 121 sources with DCO⁺ but without DCN, 4 sources with DCN but without DCO⁺, and 418 sources with neither detection. The distributions of $W(\text{DCO}^+)$ and $W(\text{DCN})$ are shown in Figure 3. $W(\text{DCO}^+)$ ranges from 0.06 to 2.40 K km s⁻¹ with a median value of 0.35 K km s⁻¹, while the FWHM ranges from 0.2 to 2.5 km s⁻¹ with a median value of 0.7 km s⁻¹. $W(\text{DCN})$ ranges from 0.10 to 0.44 K km s⁻¹ with a median value of 0.15 K km s⁻¹, while the FWHM ranges from 0.2 to 1.2 km s⁻¹ with a median value of 0.4 km s⁻¹.

In G209.28-19.6 and G206.10-15.7, multiple velocity components of DCO⁺ 1-0 were found. In G209.28-19.6, W was derived by directly integrating the velocity range of the line. In G206.10-15.7, two components are shown in Figure 4, with W values derived from a double-components Gaussian fitting.

3.3. Derived parameters of detected H¹³CO⁺ and H¹³CN 1-0

A total of 71 sources, selected from 79 sources with DCO⁺ 1-0 detections using the low velocity resolution mode (AROWS mode 3), were observed for H¹³CO⁺ and H¹³CN 1-0 simultaneously in the low velocity resolution mode (AROWS mode 3). H¹³CO⁺ 1-0 was detected in 66 sources out of these 71 observed

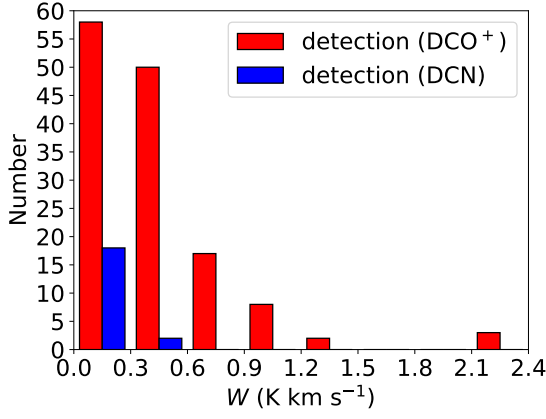


Fig. 3: Distribution of $W(\text{DCO}^+)$ (red bars) and $W(\text{DCN})$ (blue bars).

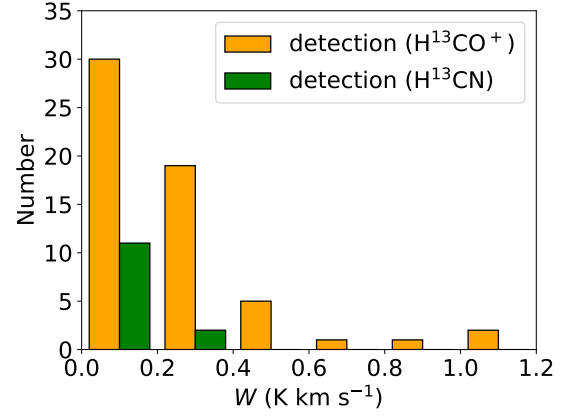


Fig. 5: Distribution of $W(\text{H}^{13}\text{CO}^+)$ (orange bars) and $W(\text{H}^{13}\text{CN})$ (green bars).

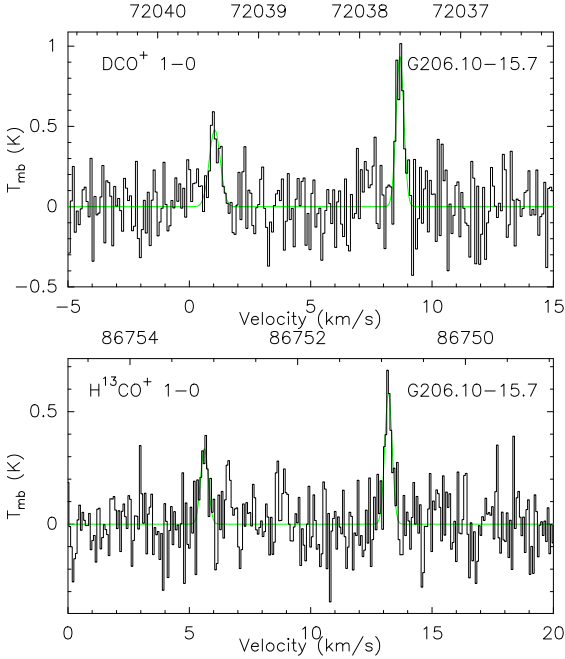


Fig. 4: Spectral lines of DCO^+ 1-0 (black line) overlaid with Gaussian fitting results (green line) toward G206.10-15.7. Double velocity components in DCO^+ and H^{13}CO^+ 1-0 were detected.

sources. Among these 66 sources with H^{13}CO^+ 1-0, there were 20 sources with H^{13}CN 1-0 detections.

H^{13}CO^+ and H^{13}CN 1-0 were detected using the high velocity resolution mode (AROWS mode 13) in 57 and 13 out of 250 sources respectively, with 12 sources showing detections of both H^{13}CO^+ and H^{13}CN 1-0. The distributions of $W(\text{H}^{13}\text{CO}^+)$ and $W(\text{H}^{13}\text{CN})$ with this mode are shown in Figure 5.

The parameters for H^{13}CO^+ and H^{13}CN 1-0 are listed in Table 5 and Table 6, respectively. $W(\text{H}^{13}\text{CO}^+)$ ranges from 0.06 to 1.11 K km s^{-1} with a median value of 0.24 K km s^{-1} , while the FWHM ranges from 0.1 to 2.4 km s^{-1} with a median value of 0.5 km s^{-1} . $W(\text{H}^{13}\text{CN})$ ranges from 0.05 to 0.28 km s^{-1} with a median value of 0.10 K km s^{-1} , while the FWHM ranges from 0.2 to 1.5 km s^{-1} with a median value of 0.4 km s^{-1} .

As mentioned in Section 3.2, G206.10-15.7 and G209.28-19.6 also exhibited multiple velocity components of H^{13}CO^+ 1-

0. For G209.28-19.6, $W(\text{H}^{13}\text{CO}^+)$ was derived by directly integrating the velocity range of the line. For G206.10-15.7, parameters for H^{13}CO^+ 1-0 with two velocity components were both listed in Table 5.

3.4. Deuterated fraction of HCO^+ and HCN

The D_{frac} values of HCO^+ and HCN are estimated by calculating the column density ratios of deuterated molecules to their hydrogenated counterparts, using their ^{13}C -isotopologue counterparts. Column densities are derived from Equation (1), assuming local thermodynamic equilibrium (LTE) and that both deuterated molecules and their ^{13}C -isotopologue counterparts are optically thin.

$$N_{\text{tot}} = \frac{8\pi k \nu^2 Q(T_{\text{ex}})}{hc^3 g_u A_{ul}} e^{\frac{E_l + h\nu}{kT_{\text{ex}}}} \int T_{\text{mb}} dv (\text{cm}^{-2}) \quad (1)$$

Where, $k = 1.38 \times 10^{-13} \text{ erg K}^{-1}$ is the Boltzmann constant, ν is the frequency of the transition, $h = 6.624 \times 10^{-27} \text{ erg s}$ is the Planck constant, $c = 2.998 \times 10^{10} \text{ cm s}^{-1}$ is the speed of light, T_{ex} is the excitation temperature (assumed to be 9.375 K), $Q(T_{\text{ex}})$ is the partition function dependent on the T_{ex} , A_{ul} is the Einstein emission coefficient, g_u is the upper level degeneracy, E_l is the energy of the ground state. $Q(T_{\text{ex}})$, A_{ul} , g_u , and E_l for the four transitions are given by the CDMS (van der Tak et al. 2009). Since all the four lines are the transitions between $J=1$ and $J=0$, E_l for each line is 0.

According to Equation (1), the column density ratios of deuterated molecules to their ^{13}C -isotopologue counterparts are given by: $N(\text{DCO}^+)/N(\text{H}^{13}\text{CO}^+) \approx 1.33 \times W(\text{DCO}^+)/W(\text{H}^{13}\text{CO}^+)$ and

$N(\text{DCN})/N(\text{H}^{13}\text{CN}) \approx 1.30 \times W(\text{DCN})/W(\text{H}^{13}\text{CN})$. $T_{\text{ex}}=9.375 \text{ K}$ is a reasonable assumption, since these sources are cold cores. Even if the gas density is below the critical densities of these lines, which might invalidate the LTE assumption, the derived column densities of DCO^+ and H^{13}CO^+ may have large uncertainties. However, the relative abundance ratio of $\text{DCO}^+/\text{H}^{13}\text{CO}^+$ estimated by there $J=1-0$ lines does not vary much, because the two molecules do have similar excitation conditions which can cancel the bias in column density estimation. It is the same for estimating the relative abundance ratio of $\text{DCN}/\text{H}^{13}\text{CN}$.

Kinematic distances of Planck cold clumps are obtained for 741 ^{13}CO components, with 51% ranging from 0.5 to 1.5 kpc

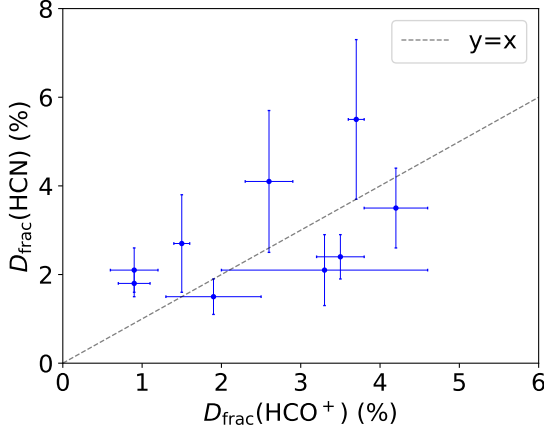


Fig. 6: $D_{\text{frac}}(\text{HCO}^+)$ v.s. $D_{\text{frac}}(\text{HCN})$ for 9 source with both deuterated fractions obtained.

(Wu et al. 2012), indicating that these sources are in the solar neighborhood. The corresponding physical scale of the beam size $87''$ for source at 1 kpc is ~ 4 pc. The $^{12}\text{C}/^{13}\text{C}$ ratio as a function of Galactocentric distance D_{GC} , $^{12}\text{C}/^{13}\text{C} = 6.21D_{\text{GC}} + 18.71$, provided in Milam et al. (2005), where the D_{GC} of the sun is 8.15 kpc (Reid et al. 2019). A $^{12}\text{C}/^{13}\text{C}$ ratio of 68, representative of the local interstellar medium, is used for these Planck cold clumps. D_{frac} values are derived from the $^{12}\text{C}/^{13}\text{C}$ ratios and column density ratios: $D_{\text{frac}}(\text{HCO}^+) = 1/68 \times N(\text{DCO}^+)/N(\text{H}^{13}\text{CO}^+)$ and $D_{\text{frac}}(\text{HCN}) = 1/68 \times N(\text{DCN})/N(\text{H}^{13}\text{CN})$, which are listed in Table 7. The 3σ upper limit values are also provided, calculated as $3\text{rms} \sqrt{\delta v \cdot \Delta v}$ ($\text{K} \cdot \text{km} \cdot \text{s}^{-1}$), where δv is the channel spacing of velocity as well as Δv is the FWHM.

$D_{\text{frac}}(\text{HCO}^+)$ are derived for 113 components from 112 sources, including two velocity components in G206.10-15.7, ranging from 0.89% to 7.4% with a median of 3.1%. $D_{\text{frac}}(\text{HCN})$ are derived for 11 sources, ranging from 1.5% to 5.5% with a median of 2.3%. Among the 9 sources with both $D_{\text{frac}}(\text{HCO}^+)$ and $D_{\text{frac}}(\text{HCN})$ values, 4 show $D_{\text{frac}}(\text{HCO}^+)$ greater than $D_{\text{frac}}(\text{HCN})$, while the remaining 5 show the opposite (see Figure 6).

3.5. FWHMs of DCO⁺ and H¹³CO⁺ 1-0

Among the 250 sources observed using the high velocity resolution mode (AROWS mode 13), the number distributions of the FWHM of DCO⁺ and H¹³CO⁺ 1-0 in 46 sources with detections of both molecules are shown in the top of Figure 7. The FWHMs of these detections are mainly below 1 km s^{-1} , with the peak at 0.3 to 0.4 km s^{-1} corresponding to 11 and 12 out of 46 detections for DCO⁺ and H¹³CO⁺ respectively. The number distributions of FWHM of DCO⁺ and H¹³CO⁺ 1-0 in the 12 sources with only DCO⁺ 1-0 detections and the 11 sources with only H¹³CO⁺ 1-0 detections are shown in the bottom of Figure 7. The FWHM of sources with single detections shows no significant difference compared to those with both DCO⁺ and H¹³CO⁺ 1-0 detections. A comparison of the FWHMs between DCO⁺ and H¹³CO⁺ is shown in Figure 8, which demonstrates that the line widths are roughly similar within the error bars, with DCO⁺ 1-0 having a slightly larger line width than H¹³CO⁺ 1-0. Figure 9 displays the comparisons between FWHM of DCO⁺ and $D_{\text{frac}}(\text{HCO}^+)$, as well as between FWHM of H¹³CO⁺ and $D_{\text{frac}}(\text{HCO}^+)$, without clear trend. The FWHM of DCO⁺ 1-0 seem to be larger than that of H¹³CO⁺ 1-0 in sources with D_{frac} greater than 5%. How-

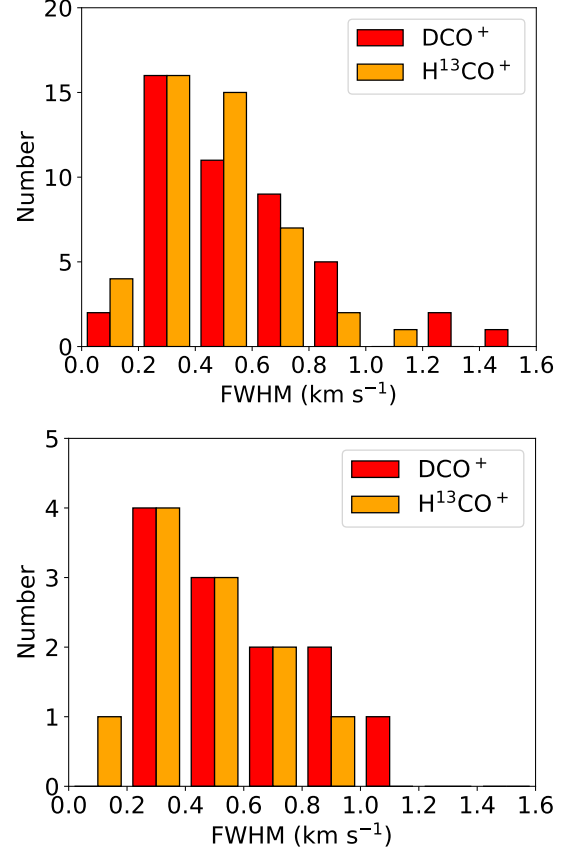


Fig. 7: Top: Distributions of FWHM for DCO⁺ (red bars) and H¹³CO⁺ (orange bars) 1-0 in 46 sources where DCO⁺ and H¹³CO⁺ 1-0 were detected using the high velocity resolution mode (AROWS mode 13). Bottom: Distribution of FWHM of DCO⁺ in sources with only DCO⁺ 1-0 detections (red bars) and distribution of FWHM of H¹³CO⁺ in sources with only H¹³CO⁺ 1-0 detections (orange bars).

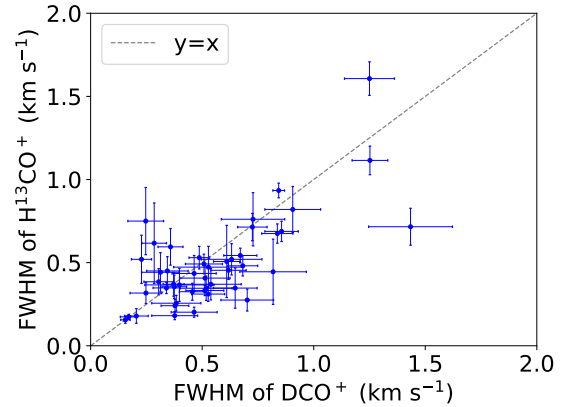


Fig. 8: FWHM of DCO⁺ 1-0 v.s. H¹³CO⁺ 1-0 of 46 sources, in which both lines were detected with the high velocity resolution mode (AROWS mode 13).

ever, it is hard to make a solid conclusion for such differences, since signal to noise ratios of H¹³CO⁺ 1-0 are not good enough in these sources.

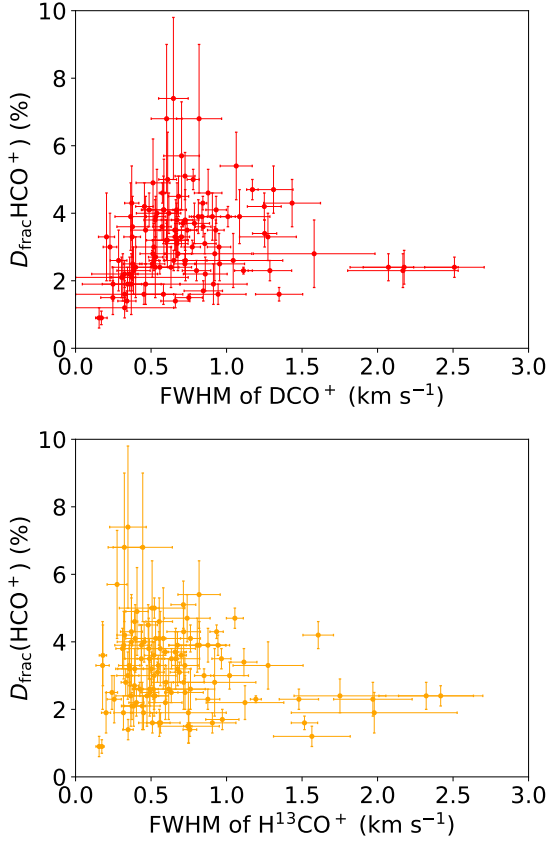


Fig. 9: Top: Comparison between the FWHM of DCO^+ and $D_{\text{frac}}(\text{HCO}^+)$. Bottom: Comparison between the FWHM of H^{13}CO^+ and $D_{\text{frac}}(\text{HCO}^+)$. Each plot contains 113 data points.

4. Discussion

4.1. The properties of these Planck cold clumps with and without DCO^+ 1-0 detection

In order to determine whether the properties of sources with DCO^+ 1-0 detections differ from those without detections, the distributions of $T_{\text{ex}}(\text{CO})$ and $W(\text{HCO}^+)$ for sources with and without DCO^+ 1-0 detections are provided, where $W(\text{HCO}^+)$ data are from Yuan et al. (2016). The distributions of $T_{\text{ex}}(\text{CO})$ for sources with and without DCO^+ 1-0 detection are similar, as shown in Figure 10. The $T_{\text{ex}}(\text{CO})$ s of these Planck cold clumps are below 30 K, mainly ranging from 7 to 12 K. The distributions of $W(\text{HCO}^+)$ for sources with and without DCO^+ 1-0 detection are also similar (see Figure 11). The detection rates of DCO^+ 1-0 is slightly higher in sources with higher $W(\text{HCO}^+)$ compared to those with lower $W(\text{HCO}^+)$. The similarity of distributions suggests that detection/non-detection status of DCO^+ 1-0 is not limited by $T_{\text{ex}}(\text{CO})$ and $W(\text{HCO}^+)$.

4.2. Possible reason of different detection rates and similar D_{frac} s of HCO^+ and HCN in Planck cold clumps

The detection rates for DCO^+ and H^{13}CO^+ 1-0 are 24.5% and 22.8%, respectively, whereas those for DCN and H^{13}CN 1-0 are 3.6% and 5.2%. This indicates that both the deuterated and ^{13}C -isotopologue counterparts of HCO^+ are detected more frequently than their HCN counterparts. The higher detection rates of DCO^+ compared to DCN 1-0, are consistent with the studies

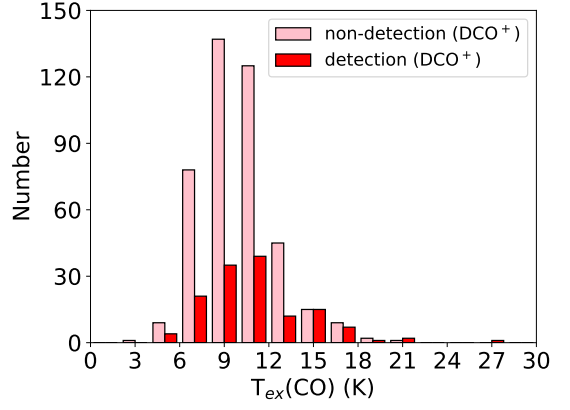


Fig. 10: Distribution of $T_{\text{ex}}(\text{CO})$ of sources where DCO^+ 1-0 is detected (red bars) and not (pink bars).

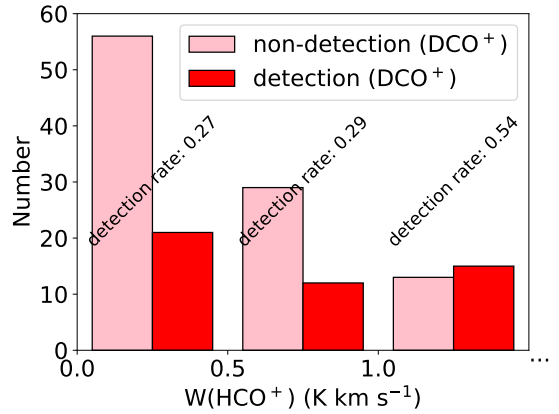


Fig. 11: Distribution of $W(\text{HCO}^+)$ of sources where DCO^+ 1-0 is detected (red bars) and not (pink bars)

of 70 μm dark high-mass clumps (Li et al. 2022) and massive starless clump candidates (Yang et al. 2024).

$D_{\text{frac}}(\text{HCO}^+)$ values in 112 sources range from 0.89% to 7.4% with a median value of 3.1%, while $D_{\text{frac}}(\text{HCN})$ values in 11 sources range from 1.5% to 5.5% with a median value of 2.3%. These values do not show a significant difference between the two molecular pairs. The D_{frac} values are consistent with those observed in molecular clouds (e.g. Hollis et al. 1976), low-mass starless cores (e.g. Tafalla et al. 2006), and massive starless clump candidates (e.g. Yang et al. 2024). Among the 9 sources where both $D_{\text{frac}}(\text{HCO}^+)$ and $D_{\text{frac}}(\text{HCN})$ were estimated, 4 sources show $D_{\text{frac}}(\text{HCO}^+)$ greater than $D_{\text{frac}}(\text{HCN})$, while the remaining 5 sources show the opposite (see Figure 6). Therefore, the significantly lower detection rate of DCN 1-0 compared to DCO^+ 1-0, despite similar noise levels, cannot be attributed to differences in D_{frac} values.

Deuterium fractionation is generally regarded as starting from the molecules-ions reaction primarily at temperature below 30 K. At these low temperatures, the reaction, $\text{HD} + \text{H}_3^+ \rightleftharpoons \text{H}_2 + \text{H}_2\text{D}^+ + \Delta E$ (where $\Delta E = 232$ K), proceeds forward, enhancing the abundance of H_2D^+ , which is a precursor to many deuterated molecules (Millar et al. 1989). DCO^+ is thought to form in the gas phase and to be abundant below ~ 30 K, while DCN is thought to form through multiple pathways in the interstellar medium, with its abundance peaking at higher temperatures compared to DCO^+ (Millar et al. 1989). Consequently,

deuterated molecules are often used as chemical clocks to trace evolutionary stages during star formation (Fuentes et al. 2005; Busquet et al. 2010; Fontani et al. 2014; Sakai et al. 2022). For example, in Kim et al. (2020), the detection rates of deuterated molecules suggest chemical evolutionary stages, while the D_{frac} s should be used for such study.

Given the similar D_{frac} values for HCO⁺ and HCN in Planck cold clumps, we propose that the disparity in detection rates between DCO⁺ and DCN 1-0 is primarily due to differences in their critical densities. This explanation was also suggested for massive starless clump candidates (Yang et al. 2024). Ignoring background emission, the optically thin critical density can be approximated by $n_{\text{crit}}^{\text{thin}} \sim A_{jk}/\gamma_{jk}$, where A_{jk} (s⁻¹) is the Einstein A and γ_{jk} (cm³ s⁻¹) is collision rate out of upper level j to level k (Shirley 2015). At 10 K, the critical densities for DCO⁺ and DCN 1-0 are 3.2×10^4 and 2.6×10^5 cm⁻³ (Feng et al. 2020), while those for H¹³CO⁺ and H¹³CN 1-0 are 6.2×10^4 and 5.3×10^5 cm⁻³ (Shirley 2015). Although the A_{jk} values for DCO⁺ and DCN 1-0 are similar, γ_{jk} related to the collision cross section for collisions with H₂ for DCO⁺ (a molecular ion) is larger than DCN (a neutral molecule), resulting in a critical density for DCO⁺ that is an order of magnitude lower than DCN (Shirley 2015). It is the same for H¹³CO⁺ and H¹³CN as that for DCO⁺ and DCN.

4.3. Origin of deuterium fractionation

The comparison between $T_{\text{ex}}(\text{CO})$ and $D_{\text{frac}}(\text{HCO}^+)$ are found to be without any trend including upper and lower limits of $D_{\text{frac}}(\text{HCO}^+)$ (see Figure 12). Most upper and lower limits of $D_{\text{frac}}(\text{HCO}^+)$ fall within expected ranges, suggesting that most sources with detections of only DCO⁺ or H¹³CO⁺ do not exhibit significantly different properties compared to sources with both detections. The small range of $T_{\text{ex}}(\text{CO})$ s for these sources makes it challenging to discuss a relationship between $T_{\text{ex}}(\text{CO})$ and deuterium fractionation. Observations of deuterium fractionation in late stages of star-forming regions are needed for further study. Chemical models suggest that deuterated molecules can be destroyed in hot molecular gas (Millar et al. 1989; Hatchell et al. 1998). Observations suggest that, in hot cores, $D_{\text{frac}}(\text{HCN})$ decreases generally from “off-core” to “on-core” positions, where temperatures vary significantly (Hatchell et al. 1998).

Among the observed sources, 12 sources exhibit lower limits of $D_{\text{frac}}(\text{HCO}^+)$, with only DCO⁺ 1-0 detections, possibly due to the lower critical density of 3.2×10^4 cm⁻³ for DCO⁺ 1-0 compared to 6.2×10^4 cm⁻³ for H¹³CO⁺ 1-0 at 10 K (Shirley 2015; Feng et al. 2020). Among these 12 sources, four sources exhibit particularly high D_{frac} values, namely G177.14-01.2, G181.84+00.3, G199.88+00.9 and G201.13+00.3 (see Figure 12), which deserve further study.

Conversely, there are 11 sources with upper limits of $D_{\text{frac}}(\text{HCO}^+)$, with only H¹³CO⁺ 1-0 detections, corresponding to low D_{frac} values. No significant differences in the number distributions of $T_{\text{ex}}(\text{CO})$ are found between sources with only DCO⁺ 1-0 detections, only H¹³CO⁺ 1-0 detections, and those with both detections (see Figure 12). The FWHM number distributions for sources with only DCO⁺ 1-0 detections, only H¹³CO⁺ 1-0 detections, and both detections show no significant differences, with FWHMs mainly within 1 km s⁻¹ (see Figure 7). It has been suggested that D_{frac} may decrease with increasing microturbulent velocity fields (Gerner et al. 2015; Li et al. 2022). However, our results do not reveal any trend between

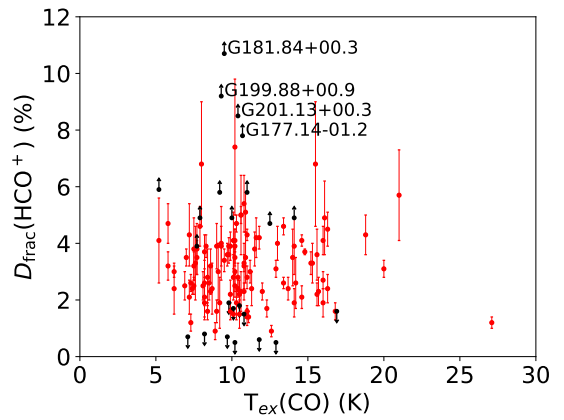


Fig. 12: The comparison of T_{ex} and $D_{\text{frac}}(\text{HCO}^+)$ (red points), including 3σ upper and lower limit value of $D_{\text{frac}}(\text{HCO}^+)$ (fire-brick points and arrows) for sources with only H¹³CO⁺ and only DCO⁺ detections, respectively.

D_{frac} and line widths for either DCO⁺ or H¹³CO⁺ 1-0 (see Figure 9). The limited range of FWHMs for these emission lines in Planck cold clumps makes it difficult to discuss the relationship between D_{frac} and FWHM.

Deuterium chemistry suggests that deuterium fractionation starts during the pre-collapse phase of molecular cloud evolution, when the gas becomes cold ($T \sim 10$ K) and dense ($n \geq 10^4$ cm⁻³) (Roberts & Millar 2000; Ceccarelli et al. 2001; Roberts & Millar 2007). This mechanism has been used to explain the high D_{frac} observed in cold molecular cores (Ceccarelli et al. 2001; Caselli et al. 2003). According to this framework, in the early stages of cold core formation ($T \sim 15$ -20 K, $n \sim 10^4$ cm⁻³), D_{frac} would remain too low ($\sim 10^{-4}$ - 10^{-3}) to produce detectable DCO⁺ 1-0, while H¹³CO⁺ 1-0 could be detected. However, among our 250 observed sources using the high velocity resolution mode (AROWS mode 13), DCO⁺ and H¹³CO⁺ 1-0 are detected in 58 and 57, with similar detection rates of 23.2% and 22.8%, respectively. More importantly, there are 46 sources with both DCO⁺ and H¹³CO⁺ 1-0 detections. DCO⁺ and H¹³CO⁺ 1-0 emissions are detected almost simultaneously in the same sources. Such results indicate that DCO⁺ can already be widespread in cold molecular clouds, rather than just beginning to become abundant. Thus, the phenomenon of high D_{frac} observed in cold cores may not be necessarily explained by cold core deuterium chemistry.

Moreover, the D_{frac} values for HCO⁺ and HCN, reflecting the enhancement of deuterium for these two species, are similar, range from 0.89% to 7.4% and 1.5% to 5.5%, respectively. Detection rates of DCN and H¹³CN 1-0, as 3.6% and 5.2% respectively, are significantly lower than those of DCO⁺ and H¹³CO⁺ 1-0, as 24.5% and 22.8% respectively. It is possibly due to the higher critical densities of DCN and H¹³CN 1-0 compared to those of DCO⁺ and H¹³CO⁺ 1-0, respectively. Thus, perhaps because the volume density is not high enough to excite DCO⁺ and DCN to $J=1$ energy level, DCO⁺ and DCN lines cannot be detected in diffuse gas. The method for testing the origin of DCO⁺ and DCN in diffuse molecular clouds is to observe the DCO⁺ and DCN absorption lines toward diffuse molecular clouds with background quasar emitting millimeter-wave continuum sources. The differences in D_{frac} during evolution of molecular clouds and late stages of star formation caused by the synthesis and depletion of deuterated molecules in different physical conditions. Thus, comparison with large-sample surveys of

deuterated molecular lines toward hot molecular cores at late stages of star formation, as well as updated astro-chemical models for these deuterated molecules, are needed to fully understand enhancement of deuterium in molecular clouds.

5. Summary

Aiming to understand the enhancement of deuterated molecules from diffuse molecular gas to cold cores, a single-pointing survey toward 559 Planck cold clumps of ECC for DCO⁺ and DCN 1-0 have been conducted using the ARO 12-m telescope. It included observations of 309 cores for DCO⁺ and DCN 1-0 simultaneously, followed by 71 of these cores where DCO⁺ 1-0 was detected for H¹³CO⁺ and H¹³CN 1-0 simultaneously, aiming to determine D_{frac} . Additionally, 250 cores were observed for DCO⁺, DCN, H¹³CO⁺, and H¹³CN 1-0 simultaneously. The observed parameters, including W , V_{LSR} and FWHM, were presented. The detection rates and D_{frac} for HCO⁺ and HCN are also presented. Potential reasons of the different detection rates and the similar D_{frac} for HCO⁺ and HCN in Planck cold clumps are discussed. The main results of this survey are as follows:

1. DCO⁺ and DCN 1-0 are detected in 79 and 11 out of 309 sources with the low velocity resolution mode (AROWS mode 3), which gives the detection rates of 25.6% and 3.6%, respectively. DCO⁺, DCN, H¹³CO⁺ and H¹³CN 1-0 detected in 58, 9, 57 and 13 out of 250 sources with the high velocity resolution mode (AROWS mode 13), which gives the detection rate of 23.2%, 3.6%, 22.8% and 5.2%, respectively. Overall, DCO⁺ and DCN 1-0 detected in 137 and 20 out of 559 sources, with detection rates of 24.5% and 3.6%, respectively, with about 6 minutes telescope time for each source.
2. $D_{\text{frac}}(\text{HCO}^+)$ values in 112 sources range from 0.89% to 7.4% with a median value of 3.1%, and $D_{\text{frac}}(\text{HCN})$ values in 11 sources range from 1.5% to 5.5% with median value of 2.3%.
3. The line widths (FWHMs) of DCO⁺ and H¹³CO⁺ 1-0 detections are mainly distributed within 1 km s⁻¹, with most measurements falling between 0.3 and 0.4 km s⁻¹.
4. Similar D_{frac} values for DCO⁺ and DCN suggest that the higher detection rate of DCO⁺ compared to DCN is due to the lower critical density of DCO⁺.
5. The nearly simultaneous detections of DCO⁺ and H¹³CO⁺ 1-0 in the same sources suggest that deuterium fractionation may start during diffuse molecular gas phase prior to cold core formation.

Acknowledgements

We would like to acknowledge the help of the staff of the ARO 12m for assistance with the observations. This work is supported by National Key R&D Program of China under grant 2023YFA1608204 and the National Natural Science Foundation of China grant 12173067.

References

Busquet, G., Palau, A., Estalella, R., et al. 2010, A&A, 517, L6. doi:10.1051/0004-6361/201014866
 Caselli, P. 2002, Planet. Space Sci., 50, 1133. doi:10.1016/S0032-0633(02)00074-0
 Caselli, P., van der Tak, F. F. S., Ceccarelli, C., et al. 2003, A&A, 403, L37. doi:10.1051/0004-6361:20030526
 Ceccarelli, C., Loinard, L., Castets, A., et al. 2001, A&A, 372, 998. doi:10.1051/0004-6361:20010559

Crapsi, A., Caselli, P., Walmsley, C. M., et al. 2005, ApJ, 619, 379. doi:10.1086/426472
 Feng, S., Li, D., Caselli, P., et al. 2020, ApJ, 901, 145. doi:10.3847/1538-4357/abada3
 Fontani, F., Caselli, P., Crapsi, A., et al. 2006, A&A, 460, 709. doi:10.1051/0004-6361:20066105
 Fontani, F., Palau, A., Caselli, P., et al. 2011, A&A, 529, L7. doi:10.1051/0004-6361/201116631
 Fontani, F., Sakai, T., Furuya, K., et al. 2014, MNRAS, 440, 448. doi:10.1093/mnras/stu298
 Fuente, A., Rizzo, J. R., Caselli, P., et al. 2005, A&A, 433, 535. doi:10.1051/0004-6361:20041914
 Gerner, T., Shirley, Y. L., Beuther, H., et al. 2015, A&A, 579, A80. doi:10.1051/0004-6361/201423989
 Guilloteau, S., Piétu, V., Dutrey, A., et al. 2006, A&A, 448, L5. doi:10.1051/0004-6361:200600005
 Hatchell, J., Millar, T. J., & Rodgers, S. D. 1998, A&A, 332, 695
 Herbst, E. 1982, A&A, 111, 76
 Hirota, T., Ikeda, M., & Yamamoto, S. 2001, ApJ, 547, 814. doi:10.1086/318380
 Hollis, J. M., Snyder, L. E., Lovas, F. J., et al. 1976, ApJ, 209, L83. doi:10.1086/182273
 Jefferts, K. B., Penzias, A. A., & Wilson, R. W. 1973, ApJ, 179, L57. doi:10.1086/181116
 Kim, G., Tatsumatsu, K., Liu, T., et al. 2020, ApJS, 249, 33. doi:10.3847/1538-4365/aba746
 Li, S., Sanhueza, P., Lu, X., et al. 2022, ApJ, 939, 102. doi:10.3847/1538-4357/ac94d4
 Li, Y., Wang, J., Li, J., et al. 2022, MNRAS, 512, 4934. doi:10.1093/mnras/stab3186
 Milam, S. N., Savage, C., Brewster, M. A., et al. 2005, ApJ, 634, 1126. doi:10.1086/497123
 Millar, T. J., Bennett, A., & Herbst, E. 1989, ApJ, 340, 906. doi:10.1086/167444
 Pillai, T., Wyrowski, F., Hatchell, J., et al. 2007, A&A, 467, 207. doi:10.1051/0004-6361:20065682
 Pillai, T., Kauffmann, J., Wyrowski, F., et al. 2011, A&A, 530, A118. doi:10.1051/0004-6361/201015899
 Planck Collaboration, Ade, P. A. R., Aghanim, N., et al. 2016, A&A, 594, A28. doi:10.1051/0004-6361/201525819
 Reid, M. J., Menten, K. M., Brunthaler, A., et al. 2019, ApJ, 885, 131. doi:10.3847/1538-4357/ab4a11
 Roberts, H. & Millar, T. J. 2007, A&A, 471, 849. doi:10.1051/0004-6361:20066608
 Roberts, H. & Millar, T. J. 2000, A&A, 361, 388
 Roberts, H., Fuller, G. A., Millar, T. J., et al. 2002, A&A, 381, 1026. doi:10.1051/0004-6361:20011596
 Roueff, E., Lis, D. C., van der Tak, F. F. S., et al. 2005, A&A, 438, 585. doi:10.1051/0004-6361:20052724
 Sakai, T., Sanhueza, P., Furuya, K., et al. 2022, ApJ, 925, 144. doi:10.3847/1538-4357/ac3d2e
 Schilke, P., Walmsley, C. M., Pineau Des Forets, G., et al. 1992, A&A, 256, 595
 Shirley, Y. L. 2015, PASP, 127, 299. doi:10.1086/680342
 Snell, R. L. & Wootten, H. A. 1977, ApJ, 216, L111. doi:10.1086/182522
 Snyder, L. E., Hollis, J. M., Buhl, D., et al. 1977, ApJ, 218, L61. doi:10.1086/182576
 Tafalla, M., Santiago-García, J., Myers, P. C., et al. 2006, A&A, 455, 577. doi:10.1051/0004-6361:20065311
 Tiné, S., Roueff, E., Falgarone, E., et al. 2000, A&A, 356, 1039
 Turner, B. E., Zuckerman, B., Morris, M., et al. 1978, ApJ, 219, L43. doi:10.1086/182603
 Turner, B. E. 2001, ApJS, 136, 579. doi:10.1086/322536
 van der Tak, F. F. S., Müller, H. S. P., Harding, M. E., et al. 2009, A&A, 507, 347. doi:10.1051/0004-6361/200912912
 Watson, W. D., Crutcher, R. M., & Dickel, J. R. 1975, ApJ, 201, 102. doi:10.1086/153864
 Watson, W. D. 1973, ApJ, 181, L129. doi:10.1086/181199
 Wu, Y., Liu, T., Meng, F., et al. 2012, ApJ, 756, 76. doi:10.1088/0004-637X/756/1/76
 Yang, K., Wang, J., Qiu, K., et al. 2024, ApJS, 270, 35. doi:10.3847/1538-4365/ad0e6f
 Yuan, J. and 9 colleagues 2016, VizieR Online Data Catalog: HCO+ and HCN obs. toward Planck Galactic Cold Clumps (Yuan+, 2016). VizieR Online Data Catalog 182.

Table 1: Detection rates of different molecular lines and observing modes.

Mode	Number of sources observed	Line	Number of sources with detections	Detection rate
low resolution mode (mode 3)	309	DCO ⁺ 1-0	79	25.6%
		DCN 1-0	11	3.6%
high resolution mode (mode 13)	250	DCO ⁺ 1-0	58	23.2%
		DCN 1-0	9	3.6%
		H ¹³ CO ⁺ 1-0	57	22.8%
		H ¹³ CN 1-0	13	5.2%
total	559	DCO ⁺ 1-0	137	24.5%
		DCN 1-0	20	3.6%

Table 2: Sources with detection of DCO⁺, DCN, H¹³CO⁺ or H¹³CN.

Source Name	R.A. (hh:mm:ss)	Dec (dd:mm:ss)	DCO ⁺	DCN	H ¹³ CO ⁺	H ¹³ CN	<i>D</i> (kpc)	<i>T</i> _{ex} (K)
G001.38+20.9	16:34:38.06	-15:46:40.71	Y	Y	Y	Y	1.1	14.8
G001.84+16.5	16:50:12.91	-18:04:22.37	Y	Y	Y	/	4.16	14.6
G003.73+16.3	16:55:21.78	-16:43:35.31	Y	/	Y	/	2.75	14.6
G003.73+18.3	16:48:54.69	-15:36:02.09	Y	/	Y	/	2.14	16.8
G004.46+16.6	16:56:11.73	-16:00:51.08	Y	/	Y	Y	2.23	15.6
G006.04+36.7	15:54:10.81	-02:50:56.32	Y	/	Y	Y	1.19	10.6
G006.32+20.4	16:47:40.85	-12:22:03.36	Y	/	Y	/	1.38	13.4
G006.41+20.5	16:47:28.67	-12:13:52.53	Y	/	Y	/	1.42	15.2
G006.70+20.6	16:47:46.71	-11:57:20.05	Y	/	Y	Y	1.17	12.3
G006.94+05.8	17:39:41.49	-19:58:05.07	Y	/	Y	/	2.37	10.1
G006.98+20.7	16:48:12.55	-11:42:10.17	Y	/	/	/	0.95	15.1
G007.14+05.9	17:39:47.47	-19:45:05.14	Y	/	Y	/	2.36	9.0
G008.52+21.8	16:47:48.42	-09:53:09.82	Y	/	Y	/	0.94	13.4
G008.67+22.1	16:47:07.71	-09:35:50.08	Y	/	Y	Y	0.84	14.1
G021.20+04.9	18:12:01.72	-08:05:27.73	Y	/	Y	Y	0.28	5.8
G021.66+03.7	18:17:06.23	-08:14:35.15	Y	Y	Y	/	0.62	9.8
G025.48+06.1	18:15:46.82	-03:45:19.28	Y	/	Y	Y	0.63	7.4
G026.85+06.7	18:16:10.50	-02:16:39.94	Y	Y	Y	Y	0.55	7.3
G027.66+05.7	18:21:28.05	-02:03:24.93	Y	/	Y	/	0.59	7.5
G028.45-06.3	19:06:09.21	-06:52:51.78	Y	Y	Y	Y	0.93	10.1
G028.71+03.8	18:29:55.29	-01:58:10.45	Y	Y	Y	Y	0.55	7.0
G028.87+04.2	18:28:56.46	-01:40:12.11	Y	/	Y	/	0.52	7.3
G030.43+02.3	18:38:30.46	-01:09:02.56	Y	/	Y	Y	0.64	10.8
G030.78+05.2	18:28:54.49	+00:28:40.02	Y	/	Y	Y	0.57	8.6
G031.44+04.1	18:33:50.27	+00:35:00.48	Y	/	Y	Y	0.78	7.5
G032.93+02.6	18:41:52.83	+01:13:45.39	Y	/	Y	Y	0.84	6.2
G038.36-00.9	19:04:45.73	+04:23:50.61	Y	/	Y	Y	1.11	11.0
G043.02+08.3	18:39:34.51	+12:44:43.47	Y	/	Y	/	0.15	10.1
G048.40-05.8	19:41:10.67	+10:56:50.84	Y	/	Y	/	0.57	7.7
G057.10+03.6	19:23:50.21	+23:07:48.89	Y	/	Y	/	0.77	12.0
G058.16+03.5	19:26:34.58	+23:59:17.87	Y	/	Y	Y	0.71	8.4
G060.75-01.2	19:50:13.23	+23:55:19.72	Y	/	Y	/	0.79	9.9
G065.43-03.1	20:08:19.49	+26:53:55.61	Y	/	/	/	0.35	7.6
G070.44-01.5	20:14:44.32	+31:57:59.95	Y	/	Y	/	1.25	15.7
G074.11+00.1	20:17:58.44	+35:56:15.15	Y	/	Y	/	5.23	10.4
★ G084.79-01.1	20:56:46.83	+43:42:17.88	Y	Y	Y	Y	2.22	11.8
G089.36-00.6	21:12:19.32	+47:24:19.39	Y	/	Y	/	0.73	9.9
G089.62+02.1	21:00:44.18	+49:30:29.76	Y	Y	Y	/	1.62	9.9
G089.93-07.0	21:39:51.55	+43:14:08.87	Y	/	Y	/		10.8
G091.29-38.1	23:08:26.74	+18:18:20.84	/	Y			2.82	8.6
G091.73+04.3	20:58:55.57	+52:32:37.12	Y	Y	Y	/	2.07	9.8
G092.02+03.9	21:02:17.26	+52:28:34.24	Y	/	Y	/	1.63	8.1
G092.26+03.8	21:03:58.96	+52:34:12.00	Y	/	Y	/	1.6	5.8
G093.20+09.5	20:37:09.59	+56:54:14.31	Y	/	/	/	1.46	6.2
G093.62-04.4	21:45:59.91	+47:35:50.06	Y	/	Y	/		10.8
G093.99-04.9	21:49:28.13	+47:28:37.93	Y	/	Y	/		8.2

Table 2: continue.

Source Name	R.A. (hh:mm:ss)	Dec (dd:mm:ss)	DCO ⁺	DCN	H ¹³ CO ⁺	H ¹³ CN	<i>D</i> (kpc)	<i>T_{ex}</i> (K)
G094.08+09.4	20:41:24.99	+57:33:22.41	Y	/	Y	/	0.98	8.2
G095.51+09.9	20:44:46.24	+58:59:14.74	Y	/	Y	/	1.37	9.0
G096.94+10.2	20:49:47.93	+60:16:24.52	Y	/	Y	/	1.26	10.2
G097.09+10.1	20:51:23.79	+60:18:36.21	Y	/	Y	/	1.27	7.7
G097.20+09.8	20:53:29.55	+60:14:26.34	Y	/	Y	/	1.22	7.9
G097.38+09.9	20:53:53.73	+60:25:22.60	Y	/	Y	/	1.17	8.2
G102.34+15.9	20:35:50.75	+67:53:21.94	Y	/	Y	/		10.2
G102.72+15.3	20:43:15.74	+67:50:41.15	Y	/	Y	Y	0.32	9.7
G103.90+13.9	21:02:23.20	+67:54:43.25	Y	/	Y	Y		11.1
G108.10+13.1	21:40:19.64	+70:20:25.48	Y	/	Y	/	1.06	8.6
G108.85-00.8	22:58:51.53	+58:57:27.12	Y	/	Y	/	5.4	15.3
G110.65+09.6	22:28:00.22	+69:01:48.14	Y	/	Y	/	0.84	11.2
G111.66+20.2	20:57:22.65	+77:35:01.72	Y	/	Y	Y	1.3	10.2
G113.75+14.9	22:24:16.19	+75:05:01.80	Y	/	/	/	0.88	8.6
G114.16+14.8	22:30:22.86	+75:13:16.60	Y	/	Y	/	0.77	10.4
G114.56+14.7	22:36:09.22	+75:21:18.22	Y	/	Y	/	0.79	9.2
G114.67+14.4	22:39:35.54	+75:11:34.02	Y	Y	Y	/	0.77	10.3
G115.81-03.5	23:56:35.69	+58:33:58.49	Y	/	Y	/	0.37	8.0
G116.23+20.3	21:57:06.33	+80:52:32.55	/	Y			1.09	5.6
G117.11+12.4	23:25:30.22	+74:19:06.45	Y	/	Y	/	0.11	10.8
G120.16+03.0	00:24:26.01	+65:49:27.56	Y	/	Y	/	2.0	13.7
G120.67+02.6	00:29:41.95	+65:26:40.02	Y	/	Y	/	1.82	16.3
G120.98+02.6	00:32:38.94	+65:28:07.05	Y	/	/	/	1.75	12.1
G121.35+03.3	00:35:48.66	+66:13:13.29	Y	/	Y	Y	0.72	7.5
G126.95-01.0	01:25:19.48	+61:32:36.24	Y	/			1.24	9.2
G127.66+13.9	02:09:18.76	+76:06:34.73	Y	/				7.2
G127.85+14.1	02:13:28.41	+76:15:01.14	Y	/				8.3
G127.88+02.6	01:38:39.10	+65:05:06.53	Y	/			1.16	12.6
G128.89+13.6	02:26:09.65	+75:27:12.35	Y	/			0.13	9.4
G130.36+11.2	02:32:13.50	+72:39:51.09	Y	/	Y	/	1.56	8.4
G132.03+08.9	02:39:33.57	+69:53:21.13	Y	/	Y	/	1.34	5.2
G133.48+09.0	02:54:44.49	+69:19:57.55	Y	/			1.68	12.8
G136.31-01.7	02:36:07.01	+58:21:09.13	Y	/			0.9	8.1
★ G142.29+07.6	03:58:53.93	+63:14:15.37	/	/	/	Y	1.43	9.1
G144.66+00.1	03:36:47.67	+55:53:53.31	Y	/	Y	/	0.85	10.9
G147.01+03.3	04:04:41.37	+56:56:16.82	Y	/			0.59	10.9
★ G150.44+03.9	04:25:07.08	+54:58:32.42	Y	/	Y	/	0.17	10.2
★ G151.08+04.4	04:30:42.88	+54:51:53.94	Y	/	Y	/	0.15	10.2
★ G156.20+05.2	04:57:00.65	+51:31:08.92	Y	/	Y	/	0.43	11.3
★ G157.54-04.0	04:20:48.94	+44:18:06.00	Y	Y	Y	Y	5.75	7.6
★ G158.20-20.2	03:29:19.31	+31:33:54.87	Y	/	Y	/	0.78	16.0
★ G158.22-20.1	03:29:47.61	+31:39:49.38	Y	/	Y	/	0.86	16.0
★ G158.37-20.7	03:28:41.99	+31:06:59.39	Y	/	Y	/	0.73	18.8
★ G159.01-08.4	04:09:55.13	+40:06:54.78	Y	/	Y	/	0.73	9.1
★ G159.21-20.1	03:32:23.18	+30:51:44.84	Y	/	Y	Y	0.71	14.1
★ G159.21-20.4	03:33:17.90	+31:06:48.54	Y	Y	Y	/	0.71	11.0
★ G159.23-34.4	02:56:04.75	+19:26:23.35	/	/	Y	/	1.17	10.2
★ G159.34+11.2	05:40:13.24	+52:17:44.74	/	Y	Y	Y	0.17	11.8
★ G159.65-19.6	03:36:04.66	+31:12:02.60	Y	/	Y	/	0.82	16.1
★ G160.53-09.8	04:10:37.94	+38:05:04.82	Y	/	Y	/	0.65	14.2
★ G160.64-35.0	02:58:48.02	+18:20:11.95	Y	Y	Y	Y	1.1	8.9
★ G161.85-35.7	03:00:26.79	+17:11:16.08	Y	Y	Y	Y	1.74	10.3
★ G161.85-08.6	04:19:31.10	+38:00:39.22	Y	/	/	/	0.47	9.2
★ G162.64-31.6	03:12:56.11	+20:04:33.85	/	Y	Y	Y	0.34	10.8
★ G163.32-08.4	04:25:31.80	+37:08:19.15	Y	/	/	/	0.41	7.9
★ G163.67-08.3	04:27:00.26	+36:56:18.24	Y	/	Y	/	0.44	7.2
★ G164.75-24.1	03:39:34.02	+24:42:59.94	Y	Y	Y	Y		12.6
★ G164.94-08.5	04:30:27.46	+35:51:45.39	Y	/	Y	/	0.24	8.3
★ G165.16-07.5	04:34:54.40	+36:23:13.28	/	/	Y	/	0.25	8.2
★ G165.69-09.1	04:30:51.85	+34:56:09.42	Y	/	/	/	0.24	5.2

Table 2: continue.

Source Name	R.A. (hh:mm:ss)	Dec (dd:mm:ss)	DCO ⁺	DCN	H ¹³ CO ⁺	H ¹³ CN	<i>D</i> (kpc)	<i>T</i> _{ex} (K)
★ G167.23-15.3	04:14:30.92	+29:35:16.09	Y	/	Y	/	1.06	8.5
★ G168.00-15.6	04:15:40.46	+28:48:00.55	/	/	Y	/	1.29	12.9
★ G168.13-16.3	04:13:47.56	+28:13:22.16	Y	/	Y	/	1.1	11.6
★ G168.72-15.4	04:18:34.58	+28:26:34.64	Y	/	Y	Y	1.29	12.9
★ G168.85-15.8	04:17:49.49	+28:06:39.04	Y	/	/	/	1.18	10.0
★ G169.32-16.1	04:18:07.30	+27:33:43.22	Y	/	Y	/	1.3	10.9
★ G169.43-16.1	04:18:23.08	+27:28:18.97	Y	/	Y	/	1.08	10.5
★ G169.76-16.1	04:19:25.47	+27:15:16.21	Y	/	Y	/	1.35	13.0
★ G169.98-18.9	04:10:57.74	+25:09:42.12	Y	/	Y	Y	1.58	11.0
★ G170.00-16.1	04:20:12.04	+27:05:52.89	Y	/	Y	/	1.36	7.2
★ G170.13-16.0	04:20:50.61	+27:03:29.08	/	/	Y	/	1.39	9.7
★ G170.26-16.0	04:21:21.47	+26:59:29.26	Y	/	Y	/	1.35	10.2
★ G170.99-15.8	04:24:10.41	+26:37:16.68	/	/	Y	/	1.41	7.1
★ G171.14-17.5	04:18:48.20	+25:18:55.88	Y	/	Y	/	1.66	10.6
★ G171.34-10.6	04:42:45.75	+29:44:27.70	Y	/	Y	/	1.37	6.2
★ G171.51-10.5	04:43:32.45	+29:39:25.68	Y	/	Y	Y	1.35	6.9
★ G171.84-05.2	05:04:08.91	+32:44:34.59	Y	/	Y	/	1.55	11.5
★ G177.14-01.2	05:33:52.81	+30:42:36.33	Y	/	/	/		10.7
★ G177.86+01.0	05:44:35.77	+31:17:57.39	Y	/	Y	/		8.7
★ G178.48-06.7	05:16:16.57	+26:29:58.11	Y	/	/	/	4.82	12.5
★ G178.98-06.7	05:17:37.38	+26:05:53.18	Y	/	Y	/	5.82	11.0
★ G181.84+00.3	05:51:10.62	+27:31:08.15	Y	/	/	/	8.99	9.5
★ G185.33-02.1	05:49:48.29	+23:16:02.13	Y	/	/	/	0.13	7.7
★ G191.00-04.5	05:53:00.77	+17:08:25.35	/	/	Y	/	0.37	10.5
★ G192.32-11.8	05:29:57.12	+12:16:50.79	Y	/	Y	/	3.43	20.0
★ G195.00-16.9	05:17:50.47	+07:24:43.08	Y	/	/	/	0.17	14.1
★ G195.09-16.4	05:19:53.82	+07:37:24.15	/	/	Y	/	0.12	16.9
★ G198.56-09.1	05:52:17.25	+08:23:18.98	Y	Y	Y	/	2.03	16.3
★ G199.88+00.9	06:30:41.17	+12:01:22.98	Y	/	/	/	0.97	9.3
★ G200.34-10.9	05:49:08.80	+05:56:35.00	Y	/	/	/	2.27	11.0
★ G201.13+00.3	06:30:49.51	+10:37:40.87	Y	/	/	/	0.79	10.4
★ G201.44+00.6	06:32:36.91	+10:30:37.66	Y	/	Y	/	0.98	10.6
★ G202.30-08.9	06:00:08.88	+05:15:06.16	Y	/	Y	Y	1.36	15.6
★ G203.20-11.2	05:53:46.20	+03:22:38.79	Y	/	Y	/	1.54	9.5
★ G204.49-11.3	05:55:43.23	+02:11:43.90	Y	/	Y	/	0.33	14.0
★ G206.10-15.7	05:43:00.61	-01:16:00.53	Y	/	Y	/	0.33	9.3
★ G207.35-19.8	05:30:50.16	-04:12:16.22	Y	/	Y	/	1.58	21.0
★ G209.28-19.6	05:34:52.22	-05:44:06.10	Y	/	Y	/	1.08	27.1
★ G211.48-19.2	05:39:52.49	-07:25:49.74	Y	/	Y	/	0.61	9.3
★ G212.10-19.1	05:41:20.21	-07:53:59.69	Y	/	Y	/	0.65	15.5
★ G213.96-19.6	05:42:38.05	-09:42:04.55	Y	/	Y	/	0.51	10.5
★ G214.43-19.9	05:42:26.71	-10:12:14.46	Y	/	Y	/	0.46	8.2
★ G215.00-15.1	06:00:51.24	-08:37:54.08	/	/	Y	/	1.43	9.8
★ G216.18-15.2	06:02:26.88	-09:42:47.78	/	/	Y	/	1.49	10.1
G359.31+17.0	16:42:30.08	-19:43:23.07	Y	/	Y	/		16.0

Note. Column 1: source name, the sources marked with “★” before source name were observed with the high velocity resolution mode (AROWS mode 13) and the rest were observed with the low velocity resolution mode (AROWS mode 3); Column 2: right ascension; Column 3: declination; Column 4~7: the emission corresponding to the table head in this source was detected (“Y”), observed but not detected(“/”) or not observed(“ ”); Column 8: kinematic distance, the data obtained from Wu et al. (2012); Column 9: excitation temperature derived from CO, obtained from Wu et al. (2012).

Table 3: Parameters of detected DCO⁺ 1-0.

Source Name	<i>W</i> (K·km s ⁻¹)	<i>V</i> _{LSR} (km s ⁻¹)	FWHM (km s ⁻¹)
G001.38+20.9	1.44 ± 0.04	0.8 ± 0.1	0.7 ± 0.1
G001.84+16.5	1.35 ± 0.04	5.8 ± 0.1	0.7 ± 0.1
G003.73+16.3	0.22 ± 0.03	6.0 ± 0.1	0.4 ± 0.1
G003.73+18.3	0.23 ± 0.04	4.2 ± 0.1	0.6 ± 0.1

Table 3: continue.

Source Name	W (K·km s ⁻¹)	V_{LSR} (km s ⁻¹)	FWHM (km s ⁻¹)
G004.46+16.6	0.16 ± 0.02	5.6 ± 0.1	0.3 ± 0.2
G006.04+36.7	1.03 ± 0.05	2.5 ± 0.1	0.8 ± 0.1
G006.32+20.4	0.77 ± 0.03	4.2 ± 0.1	0.6 ± 0.1
G006.41+20.5	0.48 ± 0.03	4.5 ± 0.1	0.7 ± 0.1
G006.70+20.6	0.34 ± 0.05	3.7 ± 0.1	0.8 ± 0.1
G006.94+05.8	0.23 ± 0.05	10.0 ± 0.1	0.9 ± 0.2
G006.98+20.7	0.14 ± 0.03	3.0 ± 0.1	0.4 ± 0.1
G007.14+05.9	0.4 ± 0.06	10.4 ± 0.1	1.1 ± 0.2
G008.52+21.8	0.48 ± 0.03	3.8 ± 0.1	0.5 ± 0.1
G008.67+22.1	0.22 ± 0.04	3.6 ± 0.1	0.4 ± 0.1
G021.20+04.9	0.39 ± 0.05	3.5 ± 0.1	0.6 ± 0.1
G021.66+03.7	1.14 ± 0.06	6.7 ± 0.1	0.8 ± 0.1
G025.48+06.1	0.57 ± 0.05	7.8 ± 0.1	0.6 ± 0.1
G026.85+06.7	0.45 ± 0.04	7.2 ± 0.1	0.7 ± 0.1
G027.66+05.7	0.33 ± 0.04	8.3 ± 0.1	0.7 ± 0.1
G028.45-06.3	0.43 ± 0.04	12.2 ± 0.1	0.8 ± 0.1
G028.71+03.8	0.96 ± 0.05	7.6 ± 0.1	0.9 ± 0.1
G028.87+04.2	0.16 ± 0.03	6.6 ± 0.1	0.4 ± 0.1
G030.43+02.3	0.37 ± 0.04	9.0 ± 0.1	0.8 ± 0.1
G030.78+05.2	1.1 ± 0.05	8.2 ± 0.1	1.1 ± 0.1
G031.44+04.1	0.42 ± 0.04	11.1 ± 0.1	0.7 ± 0.1
G032.93+02.6	0.78 ± 0.04	11.8 ± 0.1	0.8 ± 0.1
G038.36-00.9	0.67 ± 0.06	16.8 ± 0.1	1.3 ± 0.2
G043.02+08.3	0.21 ± 0.03	4.2 ± 0.1	0.6 ± 0.1
G048.40-05.8	0.25 ± 0.03	9.5 ± 0.1	0.7 ± 0.1
G057.10+03.6	0.49 ± 0.05	11.8 ± 0.1	1.3 ± 0.1
G058.16+03.5	0.21 ± 0.03	9.9 ± 0.1	0.5 ± 0.1
G060.75-01.2	0.25 ± 0.04	10.8 ± 0.1	0.9 ± 0.2
G065.43-03.1	0.2 ± 0.06	5.8 ± 0.3	1.7 ± 0.5
G070.44-01.5	0.43 ± 0.07	10.8 ± 0.2	2.2 ± 0.4
G074.11+00.1	0.74 ± 0.06	-1.1 ± 0.1	2.5 ± 0.2
★ G084.79-01.1	2.37 ± 0.19	2.0 ± 0.1	1.2 ± 0.1
G089.36-00.6	0.3 ± 0.04	2.7 ± 0.1	0.9 ± 0.1
G089.62+02.1	0.58 ± 0.04	-0.3 ± 0.1	0.8 ± 0.1
G089.93-07.0	0.18 ± 0.03	12.8 ± 0.1	0.6 ± 0.1
G091.73+04.3	1.17 ± 0.05	-4.4 ± 0.1	1.0 ± 0.1
G092.02+03.9	0.26 ± 0.04	-1.9 ± 0.1	1.0 ± 0.2
G092.26+03.8	0.53 ± 0.04	-1.8 ± 0.1	1.3 ± 0.1
G093.20+09.5	0.18 ± 0.04	-1.8 ± 0.1	0.5 ± 0.3
G093.62-04.4	0.53 ± 0.05	3.7 ± 0.1	1.1 ± 0.1
G093.99-04.9	0.23 ± 0.05	4.7 ± 0.1	0.9 ± 0.2
G094.08+09.4	0.36 ± 0.05	0.1 ± 0.1	0.8 ± 0.1
G095.51+09.9	0.12 ± 0.02	-2.6 ± 0.1	0.4 ± 0.1
G096.94+10.2	0.36 ± 0.04	-2.6 ± 0.1	0.5 ± 0.1
G097.09+10.1	0.31 ± 0.04	-2.6 ± 0.1	0.7 ± 0.1
G097.20+09.8	0.54 ± 0.05	-2.2 ± 0.1	0.9 ± 0.1
G097.38+09.9	0.2 ± 0.05	-2.4 ± 0.1	1.0 ± 0.3
G102.34+15.9	0.63 ± 0.04	2.5 ± 0.1	0.7 ± 0.1
G102.72+15.3	0.44 ± 0.04	1.3 ± 0.1	0.6 ± 0.1
G103.90+13.9	0.3 ± 0.04	2.9 ± 0.1	0.7 ± 0.1
G108.10+13.1	0.36 ± 0.04	-5.5 ± 0.1	0.6 ± 0.1
G108.85-00.8	0.41 ± 0.05	-49.5 ± 0.1	1.3 ± 0.2
G110.65+09.6	0.78 ± 0.05	-4.5 ± 0.1	0.9 ± 0.1
G111.66+20.2	0.91 ± 0.05	-8.2 ± 0.1	0.9 ± 0.1
G113.75+14.9	0.1 ± 0.03	-5.0 ± 0.1	0.4 ± 0.1
G114.16+14.8	0.35 ± 0.04	-4.1 ± 0.1	0.7 ± 0.1
G114.56+14.7	0.11 ± 0.03	-4.4 ± 0.1	0.4 ± 0.3
G114.67+14.4	2.12 ± 0.06	-4.6 ± 0.1	1.2 ± 0.1
G115.81-03.5	0.35 ± 0.04	-1.0 ± 0.1	0.6 ± 0.1
G117.11+12.4	0.63 ± 0.04	4.0 ± 0.1	0.7 ± 0.1

Table 3: continue.

Source Name	W (K·km s ⁻¹)	V_{LSR} (km s ⁻¹)	FWHM (km s ⁻¹)
G120.16+03.0	0.67 ± 0.06	-19.5 ± 0.1	2.1 ± 0.2
G120.67+02.6	0.38 ± 0.06	-18.0 ± 0.2	2.2 ± 0.4
G120.98+02.6	0.17 ± 0.05	-17.2 ± 0.2	1.4 ± 0.3
G121.35+03.3	0.29 ± 0.04	-5.3 ± 0.1	0.7 ± 0.1
G126.95-01.0	0.21 ± 0.04	-12.1 ± 0.1	0.7 ± 0.1
G127.66+13.9	0.34 ± 0.06	3.3 ± 0.1	0.9 ± 0.2
G127.85+14.1	0.35 ± 0.06	2.7 ± 0.1	0.6 ± 0.1
G127.88+02.6	0.26 ± 0.07	-11.1 ± 0.1	0.9 ± 0.4
G128.89+13.6	0.8 ± 0.04	3.9 ± 0.1	0.7 ± 0.1
G130.36+11.2	0.23 ± 0.06	-15.9 ± 0.3	1.6 ± 0.4
G132.03+08.9	0.21 ± 0.04	-13.3 ± 0.1	0.6 ± 0.1
G133.48+09.0	0.74 ± 0.13	-16.8 ± 0.2	2.3 ± 0.6
G136.31-01.7	0.27 ± 0.05	-8.6 ± 0.1	1.1 ± 0.2
G144.66+00.1	0.32 ± 0.05	-8.0 ± 0.1	0.7 ± 0.1
G147.01+03.3	0.44 ± 0.05	-4.7 ± 0.1	0.6 ± 0.1
★ G150.44+03.9	0.38 ± 0.05	3.5 ± 0.1	0.6 ± 0.1
★ G151.08+04.4	0.29 ± 0.05	3.1 ± 0.1	0.5 ± 0.1
★ G156.20+05.2	0.27 ± 0.05	5.1 ± 0.1	0.6 ± 0.1
★ G157.54-04.0	0.12 ± 0.03	-31.0 ± 0.1	0.2 ± 0.1
★ G158.20-20.2	0.69 ± 0.06	7.5 ± 0.1	0.5 ± 0.1
★ G158.22-20.1	0.13 ± 0.03	8.2 ± 0.1	0.2 ± 0.1
★ G158.37-20.7	0.68 ± 0.08	6.8 ± 0.1	1.4 ± 0.2
★ G159.01-08.4	0.17 ± 0.03	-4.8 ± 0.1	0.2 ± 0.1
★ G159.21-20.4	0.18 ± 0.04	6.5 ± 0.1	0.3 ± 0.1
★ G159.21-20.1	2.2 ± 0.05	6.1 ± 0.1	0.8 ± 0.1
★ G159.65-19.6	0.3 ± 0.06	7.4 ± 0.1	0.5 ± 0.1
★ G160.53-09.8	0.19 ± 0.03	-3.9 ± 0.1	0.3 ± 0.1
★ G160.64-35.0	0.06 ± 0.02	-4.5 ± 0.1	0.2 ± 0.1
★ G161.85-35.7	0.19 ± 0.05	-6.6 ± 0.1	0.5 ± 0.1
★ G161.85-08.6	0.21 ± 0.05	-2.7 ± 0.1	0.5 ± 0.2
★ G163.32-08.4	0.1 ± 0.03	-2.3 ± 0.1	0.3 ± 0.2
★ G163.67-08.3	0.17 ± 0.04	-2.1 ± 0.1	0.3 ± 0.1
★ G164.75-24.1	0.1 ± 0.02	1.1 ± 0.1	0.2 ± 0.1
★ G164.94-08.5	1.01 ± 0.07	-0.8 ± 0.1	0.8 ± 0.1
★ G165.69-09.1	0.27 ± 0.06	-0.8 ± 0.1	0.5 ± 0.1
★ G167.23-15.3	0.29 ± 0.05	6.5 ± 0.1	0.7 ± 0.1
★ G168.13-16.3	0.47 ± 0.05	6.1 ± 0.1	0.5 ± 0.1
★ G168.72-15.4	0.73 ± 0.06	7.0 ± 0.1	0.7 ± 0.1
★ G168.85-15.8	0.15 ± 0.04	5.8 ± 0.1	0.4 ± 0.1
★ G169.32-16.1	0.76 ± 0.06	6.7 ± 0.1	0.7 ± 0.1
★ G169.43-16.1	0.15 ± 0.04	5.4 ± 0.1	0.2 ± 0.1
★ G169.76-16.1	0.54 ± 0.06	6.5 ± 0.1	0.6 ± 0.1
★ G169.98-18.9	0.22 ± 0.04	7.4 ± 0.1	0.3 ± 0.1
★ G170.00-16.1	0.31 ± 0.04	6.5 ± 0.1	0.4 ± 0.1
★ G170.26-16.0	0.48 ± 0.06	6.3 ± 0.1	0.5 ± 0.1
★ G171.14-17.5	0.21 ± 0.05	7.2 ± 0.1	0.4 ± 0.1
★ G171.34-10.6	0.16 ± 0.05	5.9 ± 0.1	0.4 ± 0.2
★ G171.51-10.5	0.23 ± 0.04	5.6 ± 0.1	0.4 ± 0.1
★ G171.84-05.2	0.47 ± 0.05	6.7 ± 0.1	0.5 ± 0.1
★ G177.14-01.2	0.32 ± 0.06	-17.6 ± 0.1	0.7 ± 0.2
★ G177.86+01.0	0.17 ± 0.05	-18.7 ± 0.1	0.5 ± 0.2
★ G178.48-06.7	0.12 ± 0.03	7.3 ± 0.1	0.3 ± 0.1
★ G178.98-06.7	0.45 ± 0.05	7.2 ± 0.1	0.5 ± 0.1
★ G181.84+00.3	0.44 ± 0.06	2.9 ± 0.1	0.8 ± 0.1
★ G185.33-02.1	0.16 ± 0.05	-0.9 ± 0.1	0.6 ± 0.2
★ G192.32-11.8	0.77 ± 0.06	11.2 ± 0.1	0.9 ± 0.1
★ G195.00-16.9	0.15 ± 0.04	-2.3 ± 0.1	0.3 ± 0.1
★ G198.56-09.1	0.44 ± 0.04	10.5 ± 0.1	0.7 ± 0.1
★ G199.88+00.9	0.47 ± 0.06	5.1 ± 0.1	0.9 ± 0.1
★ G200.34-10.9	0.12 ± 0.03	12.8 ± 0.1	0.2 ± 0.1

Table 3: continue.

Source Name	W (K·km s ⁻¹)	V_{LSR} (km s ⁻¹)	FWHM (km s ⁻¹)
★ G201.13+00.3	0.39 ± 0.07	4.4 ± 0.1	1.1 ± 0.2
★ G201.44+00.6	0.49 ± 0.05	5.8 ± 0.1	0.6 ± 0.1
★ G202.30-08.9	0.26 ± 0.05	11.4 ± 0.1	0.4 ± 0.1
★ G203.20-11.2	1.06 ± 0.07	9.6 ± 0.1	1.3 ± 0.1
★ G204.49-11.3	0.2 ± 0.04	1.0 ± 0.1	0.5 ± 0.1
★ G206.10-15.7	0.27 ± 0.06	1.0 ± 0.1	0.5 ± 0.1
¹	0.37 ± 0.05	8.7 ± 0.1	0.4 ± 0.1
★ G207.35-19.8	0.38 ± 0.06	10.6 ± 0.1	0.7 ± 0.1
★ G209.28-19.6 ²	0.62 ± 0.08
★ G211.48-19.2	0.62 ± 0.08	3.3 ± 0.1	0.9 ± 0.1
★ G212.10-19.1	0.59 ± 0.09	3.7 ± 0.1	0.8 ± 0.1
★ G213.96-19.6	0.27 ± 0.05	2.7 ± 0.1	0.4 ± 0.1
★ G214.43-19.9	0.2 ± 0.05	2.1 ± 0.1	0.3 ± 0.1
G359.31+17.0	0.47 ± 0.04	5.4 ± 0.1	0.5 ± 0.1

Note. Column 1: source name, the sources marked with “★” before source name were observed with the high velocity resolution mode (AROWS mode 13) and the rest were observed with the low velocity resolution mode (AROWS mode 3); Column 2: velocity integrated intensity; Column 3: local standard of rest velocity; Column 4: full width at half maximum.

Table 4: Parameters of detected DCN 1-0.

Source Name	W (K·km s ⁻¹)	V_{LSR} (km s ⁻¹)	FWHM (km s ⁻¹)
G001.38+20.9	0.23 ± 0.05	0.6 ± 0.1	0.4 ± 0.1
G001.84+16.5	0.13 ± 0.03	5.8 ± 0.1	0.4 ± 0.1
G021.66+03.7	0.21 ± 0.06	6.8 ± 0.1	0.8 ± 0.2
G026.85+06.7	0.15 ± 0.04	7.0 ± 0.1	0.9 ± 0.3
G028.45-06.3	0.1 ± 0.03	12.2 ± 0.1	0.4 ± 0.1
G028.71+03.8	0.19 ± 0.03	7.4 ± 0.1	0.4 ± 0.1
★ G084.79-01.1	0.44 ± 0.08	1.8 ± 0.1	1.1 ± 0.2
G089.62+02.1	0.14 ± 0.04	-0.4 ± 0.1	0.5 ± 0.2
G091.29-38.1	0.17 ± 0.05	-3.9 ± 0.1	1.0 ± 0.4
G091.73+04.3	0.25 ± 0.05	-4.4 ± 0.1	1.2 ± 0.2
G114.67+14.4	0.28 ± 0.06	-4.5 ± 0.1	1.1 ± 0.2
G116.23+20.3	0.11 ± 0.02	-7.9 ± 0.1	0.4 ± 0.1
★ G157.54-04.0	0.12 ± 0.03	-31.1 ± 0.1	0.3 ± 0.1
★ G159.21-20.1	0.34 ± 0.04	6.1 ± 0.1	0.6 ± 0.1
★ G159.34+11.2	0.13 ± 0.03	2.5 ± 0.1	0.2 ± 0.1
★ G160.64-35.0	0.14 ± 0.03	-4.4 ± 0.1	0.2 ± 0.1
★ G161.85-35.7	0.13 ± 0.03	-6.6 ± 0.1	0.2 ± 0.1
★ G162.64-31.6	0.12 ± 0.03	-0.9 ± 0.1	0.2 ± 0.1
★ G164.75-24.1	0.2 ± 0.03	1.1 ± 0.1	0.2 ± 0.1
★ G198.56-09.1	0.1 ± 0.02	10.6 ± 0.1	0.2 ± 0.1

Note. Column 1: source name, the sources marked with “★” before source name were observed with the high velocity resolution mode (AROWS mode 13) and the rest were observed with the low velocity resolution mode (AROWS mode 3); Column 2: velocity integrated intensity; Column 3: local standard of rest velocity; Column 4: full width at half maximum.

Table 5: Parameters of detected H¹³CO⁺ 1-0

Source Name	W (K·km s ⁻¹)	V_{LSR} (km s ⁻¹)	FWHM (km s ⁻¹)
G001.38+20.9	0.76 ± 0.02	0.6 ± 0.1	0.6 ± 0.1
G001.84+16.5	0.64 ± 0.02	5.8 ± 0.1	0.6 ± 0.1
G003.73+16.3	0.2 ± 0.02	6.1 ± 0.1	0.4 ± 0.1
G003.73+18.3	0.28 ± 0.02	4.2 ± 0.1	0.5 ± 0.1
G004.46+16.6	0.14 ± 0.02	5.5 ± 0.1	0.4 ± 0.1

¹ G206.10-15.7 contains 2 velocity components, and the parameters are derived from double-component Gaussian fitting.

² The profile of the line in G209.28-19.6 is not Gaussian, so V_{LSR} and FWHM are not provided.

Table 5: continue.

Source Name	W (K·km s ⁻¹)	V_{LSR} (km s ⁻¹)	FWHM (km s ⁻¹)
G006.04+36.7	0.4 ± 0.02	2.4 ± 0.1	0.5 ± 0.1
G006.32+20.4	0.33 ± 0.02	4.2 ± 0.1	0.4 ± 0.1
G006.41+20.5	0.28 ± 0.03	4.5 ± 0.1	0.7 ± 0.1
G006.70+20.6	0.39 ± 0.03	3.6 ± 0.1	1.0 ± 0.1
G006.94+05.8	0.16 ± 0.03	9.9 ± 0.1	0.7 ± 0.1
G007.14+05.9	0.2 ± 0.03	10.3 ± 0.1	0.8 ± 0.2
G008.52+21.8	0.36 ± 0.02	3.7 ± 0.1	0.4 ± 0.1
G008.67+22.1	0.11 ± 0.02	3.3 ± 0.1	0.3 ± 0.1
G021.20+04.9	0.24 ± 0.02	3.5 ± 0.1	0.5 ± 0.1
G021.66+03.7	0.61 ± 0.03	6.6 ± 0.1	0.7 ± 0.1
G025.48+06.1	0.46 ± 0.02	7.7 ± 0.1	0.5 ± 0.1
G026.85+06.7	0.34 ± 0.02	7.1 ± 0.1	0.5 ± 0.1
G027.66+05.7	0.2 ± 0.02	8.2 ± 0.1	0.7 ± 0.1
G028.45-06.3	0.57 ± 0.02	12.1 ± 0.1	0.7 ± 0.1
G028.71+03.8	0.53 ± 0.03	7.5 ± 0.1	1.0 ± 0.1
G028.87+04.2	0.25 ± 0.03	6.9 ± 0.1	1.6 ± 0.3
G030.43+02.3	0.32 ± 0.03	9.1 ± 0.1	0.9 ± 0.1
G030.78+05.2	0.93 ± 0.03	8.2 ± 0.1	1.2 ± 0.1
G031.44+04.1	0.33 ± 0.02	11.1 ± 0.1	0.6 ± 0.1
G032.93+02.6	0.51 ± 0.03	11.8 ± 0.1	0.9 ± 0.1
G038.36-00.9	0.81 ± 0.04	16.5 ± 0.1	1.5 ± 0.1
G043.02+08.3	0.1 ± 0.02	4.1 ± 0.1	0.4 ± 0.1
G048.40-05.8	0.14 ± 0.02	9.6 ± 0.1	0.5 ± 0.1
G057.10+03.6	0.41 ± 0.03	11.8 ± 0.1	1.5 ± 0.1
G058.16+03.5	0.25 ± 0.02	9.9 ± 0.1	0.6 ± 0.1
G060.75-01.2	0.3 ± 0.04	10.8 ± 0.1	0.9 ± 0.2
G070.44-01.5	0.36 ± 0.04	10.9 ± 0.1	2.0 ± 0.3
G074.11+00.1	0.6 ± 0.06	-0.9 ± 0.1	2.4 ± 0.3
★ G084.79-01.1	1.11 ± 0.06	...	1.6 ± 0.1
G089.36-00.6	0.26 ± 0.04	2.7 ± 0.1	1.1 ± 0.3
G089.62+02.1	0.29 ± 0.03	-0.3 ± 0.1	0.9 ± 0.1
G089.93-07.0	0.11 ± 0.02	12.8 ± 0.1	0.4 ± 0.1
G091.73+04.3	0.58 ± 0.04	-4.4 ± 0.1	0.9 ± 0.1
G092.02+03.9	0.2 ± 0.03	-2.0 ± 0.1	0.7 ± 0.1
G092.26+03.8	0.22 ± 0.03	-1.6 ± 0.1	0.7 ± 0.2
G093.62-04.4	0.19 ± 0.03	3.7 ± 0.1	0.8 ± 0.1
G093.99-04.9	0.24 ± 0.05	4.6 ± 0.2	2.0 ± 0.5
G094.08+09.4	0.19 ± 0.02	0.0 ± 0.1	0.7 ± 0.1
G095.51+09.9	0.15 ± 0.03	-2.6 ± 0.1	0.6 ± 0.1
G096.94+10.2	0.18 ± 0.02	-2.5 ± 0.1	0.4 ± 0.1
G097.09+10.1	0.16 ± 0.03	-2.6 ± 0.1	0.5 ± 0.1
G097.20+09.8	0.23 ± 0.03	-2.2 ± 0.1	0.6 ± 0.1
G097.38+09.9	0.15 ± 0.03	-2.4 ± 0.1	0.5 ± 0.1
G102.34+15.9	0.35 ± 0.02	2.6 ± 0.1	0.6 ± 0.1
G102.72+15.3	0.24 ± 0.02	1.2 ± 0.1	0.5 ± 0.1
G103.90+13.9	0.41 ± 0.02	2.8 ± 0.1	0.8 ± 0.1
G108.10+13.1	0.22 ± 0.03	-5.4 ± 0.1	0.4 ± 0.1
G108.85-00.8	0.24 ± 0.04	-49.7 ± 0.1	1.3 ± 0.2
G110.65+09.6	0.5 ± 0.05	-4.5 ± 0.1	1.0 ± 0.1
G111.66+20.2	0.43 ± 0.03	-8.1 ± 0.1	0.8 ± 0.1
G114.16+14.8	0.24 ± 0.03	-4.0 ± 0.1	0.6 ± 0.1
G114.56+14.7	0.11 ± 0.04	-4.7 ± 0.1	0.7 ± 0.3
G114.67+14.4	0.88 ± 0.04	-4.5 ± 0.1	1.1 ± 0.1
G115.81-03.5	0.1 ± 0.03	-0.9 ± 0.1	0.3 ± 0.1
G117.11+12.4	0.37 ± 0.03	4.0 ± 0.1	0.5 ± 0.1
G120.16+03.0	0.54 ± 0.07	-19.3 ± 0.1	2.3 ± 0.3
G120.67+02.6	0.31 ± 0.05	-18.2 ± 0.1	1.8 ± 0.3
G121.35+03.3	0.15 ± 0.04	-5.2 ± 0.1	0.6 ± 0.2
G130.36+11.2	0.16 ± 0.04	-15.7 ± 0.1	0.9 ± 0.3
G132.03+08.9	0.1 ± 0.03	-13.4 ± 0.1	0.6 ± 0.2

Table 5: continue.

Source Name	W (K·km s ⁻¹)	V_{LSR} (km s ⁻¹)	FWHM (km s ⁻¹)
G144.66+00.1	0.18 ± 0.04	-7.7 ± 0.1	0.7 ± 0.2
★ G150.44+03.9	0.1 ± 0.03	...	0.3 ± 0.1
★ G151.08+04.4	0.19 ± 0.03	...	0.3 ± 0.1
★ G156.20+05.2	0.22 ± 0.03	...	0.5 ± 0.1
★ G157.54-04.0	0.07 ± 0.02	...	0.2 ± 0.1
★ G158.20-20.2	0.33 ± 0.03	...	0.5 ± 0.1
★ G158.22-20.1	0.13 ± 0.02	...	0.3 ± 0.1
★ G158.37-20.7	0.31 ± 0.04	...	0.7 ± 0.1
★ G159.01-08.4	0.11 ± 0.03	...	0.5 ± 0.1
★ G159.21-20.4	0.18 ± 0.03	...	0.5 ± 0.1
★ G159.21-20.1	1.0 ± 0.04	...	0.9 ± 0.1
★ G159.23-34.4	0.28 ± 0.03	...	0.5 ± 0.1
★ G159.34+11.2	0.19 ± 0.02	...	0.2 ± 0.1
★ G159.65-19.6	0.12 ± 0.02	...	0.4 ± 0.1
★ G160.53-09.8	0.14 ± 0.04	...	0.6 ± 0.2
★ G160.64-35.0	0.13 ± 0.02	...	0.2 ± 0.1
★ G161.85-35.7	0.2 ± 0.03	...	0.2 ± 0.1
★ G162.64-31.6	0.08 ± 0.02	...	0.2 ± 0.1
★ G163.67-08.3	0.16 ± 0.03	...	0.4 ± 0.1
★ G164.75-24.1	0.22 ± 0.02	...	0.2 ± 0.1
★ G164.94-08.5	0.51 ± 0.04	...	0.7 ± 0.1
★ G165.16-07.5	0.22 ± 0.03	...	0.6 ± 0.1
★ G167.23-15.3	0.22 ± 0.04	...	0.8 ± 0.2
★ G168.00-15.6	0.42 ± 0.03	...	0.5 ± 0.1
★ G168.13-16.3	0.22 ± 0.03	...	0.3 ± 0.1
★ G168.72-15.4	0.46 ± 0.03	...	0.5 ± 0.1
★ G169.32-16.1	0.29 ± 0.03	...	0.7 ± 0.1
★ G169.43-16.1	0.19 ± 0.04	...	0.8 ± 0.2
★ G169.76-16.1	0.26 ± 0.03	...	0.5 ± 0.1
★ G169.98-18.9	0.31 ± 0.03	...	0.3 ± 0.1
★ G170.00-16.1	0.14 ± 0.03	...	0.4 ± 0.1
★ G170.13-16.0	0.42 ± 0.04	...	0.8 ± 0.1
★ G170.26-16.0	0.38 ± 0.04	...	0.5 ± 0.1
★ G170.99-15.8	0.31 ± 0.04	...	0.5 ± 0.1
★ G171.14-17.5	0.18 ± 0.03	...	0.3 ± 0.1
★ G171.34-10.6	0.13 ± 0.03	...	0.4 ± 0.1
★ G171.51-10.5	0.18 ± 0.02	...	0.2 ± 0.1
★ G171.84-05.2	0.24 ± 0.03	...	0.3 ± 0.1
★ G177.86+01.0	0.14 ± 0.03	...	0.5 ± 0.1
★ G178.98-06.7	0.31 ± 0.02	...	0.3 ± 0.1
★ G191.00-04.5	0.1 ± 0.02	...	0.3 ± 0.1
★ G192.32-11.8	0.49 ± 0.04	...	0.7 ± 0.1
★ G195.09-16.4	0.06 ± 0.02	...	0.1 ± 0.1
★ G198.56-09.1	0.19 ± 0.02	...	0.5 ± 0.1
★ G201.44+00.6	0.19 ± 0.05	...	0.5 ± 0.2
★ G202.30-08.9	0.14 ± 0.02	...	0.2 ± 0.1
★ G203.20-11.2	0.6 ± 0.05	...	1.1 ± 0.1
★ G204.49-11.3	0.11 ± 0.02	...	0.4 ± 0.1
★ G206.10-15.7	0.13 ± 0.03	...	0.4 ± 0.1
¹	0.22 ± 0.03	...	0.4 ± 0.1
★ G207.35-19.8	0.13 ± 0.03	...	0.3 ± 0.1
★ G209.28-19.6 ²	0.99 ± 0.06
★ G211.48-19.2	0.31 ± 0.04	...	0.8 ± 0.1
★ G212.10-19.1	0.17 ± 0.05	...	0.4 ± 0.2
★ G213.96-19.6	0.24 ± 0.04	...	0.6 ± 0.1
★ G214.43-19.9	0.19 ± 0.04	...	0.4 ± 0.1
★ G215.00-15.1	0.08 ± 0.02	...	0.2 ± 0.1

¹ G206.10-15.7 contains 2 velocity components, and the parameters are derived from double-component Gaussian fitting.² The profile of the line in G209.28-19.6 is not Gaussian, so V_{LSR} and FWHM are not provided.

Table 5: continue.

Source Name	W (K·km s ⁻¹)	V_{LSR} (km s ⁻¹)	FWHM (km s ⁻¹)
★ G216.18-15.2	0.15 ± 0.04	...	0.6 ± 0.2
G359.31+17.0	0.34 ± 0.02	5.4 ± 0.1	0.4 ± 0.1

Note. Column 1: source name, the sources marked with “★” before source name were observed with the high velocity resolution mode (AROWS mode 13) and the rest were observed with the low velocity resolution mode (AROWS mode 3); Column 2: velocity integrated intensity; Column 3: local standard of rest velocity; Column 4: full width at half maximum. In the high velocity resolution mode (AROWS mode 13) observations, due to errors in the Doppler tracking for different sidebands during the shared risking period, the V_{LSR} measurements of H¹³CO⁺ and H¹³CN 1-0 have an uncertainty of 1 to 7 km s⁻¹, while the other parameters are corrected. Therefore, the V_{LSR} values are not provided here and not used for scientific discussions.

Table 6: Parameters of detected H¹³CN 1-0.

Source Name	W (K·km s ⁻¹)	V_{LSR} (km s ⁻¹)	FWHM (km s ⁻¹)
G001.38+20.9	0.08 ± 0.02	0.9 ± 0.1	0.5 ± 0.1
G004.46+16.6	0.09 ± 0.03	5.3 ± 0.2	0.8 ± 0.3
G006.04+36.7	0.06 ± 0.02	2.6 ± 0.1	0.3 ± 0.2
G006.70+20.6	0.06 ± 0.02	3.9 ± 0.1	0.4 ± 0.1
G008.67+22.1	0.06 ± 0.02	3.7 ± 0.1	0.4 ± 0.2
G021.20+04.9	0.07 ± 0.02	3.7 ± 0.1	0.6 ± 0.2
G025.48+06.1	0.1 ± 0.02	7.7 ± 0.1	0.5 ± 0.1
G026.85+06.7	0.07 ± 0.02	7.3 ± 0.1	0.7 ± 0.2
G028.45-06.3	0.07 ± 0.02	12.2 ± 0.1	0.4 ± 0.2
G028.71+03.8	0.15 ± 0.02	7.7 ± 0.1	1.0 ± 0.2
G030.43+02.3	0.05 ± 0.02	9.1 ± 0.1	0.4 ± 0.2
G030.78+05.2	0.28 ± 0.04	8.0 ± 0.1	1.5 ± 0.2
G031.44+04.1	0.05 ± 0.02	11.2 ± 0.1	0.4 ± 0.2
G032.93+02.6	0.07 ± 0.03	11.6 ± 0.1	0.7 ± 0.4
G038.36-00.9	0.16 ± 0.03	16.8 ± 0.1	1.3 ± 0.2
G058.16+03.5	0.05 ± 0.02	10.0 ± 0.1	0.3 ± 0.1
★ G084.79-01.1	0.24 ± 0.04	...	1.1 ± 0.2
G102.72+15.3	0.05 ± 0.02	1.2 ± 0.1	0.4 ± 0.1
G103.90+13.9	0.15 ± 0.03	2.8 ± 0.1	0.8 ± 0.2
G111.66+20.2	0.11 ± 0.03	-8.0 ± 0.1	0.9 ± 0.3
G121.35+03.3	0.07 ± 0.02	-5.9 ± 0.1	0.5 ± 0.2
★ G142.29+07.6	0.09 ± 0.02	...	0.2 ± 0.1
★ G157.54-04.0	0.11 ± 0.03	...	0.3 ± 0.1
★ G159.21-20.4	0.13 ± 0.03	...	0.4 ± 0.1
★ G159.34+11.2	0.16 ± 0.02	...	0.2 ± 0.1
★ G160.64-35.0	0.13 ± 0.02	...	0.2 ± 0.1
★ G161.85-35.7	0.17 ± 0.02	...	0.2 ± 0.1
★ G162.64-31.6	0.1 ± 0.03	...	0.3 ± 0.1
★ G164.75-24.1	0.21 ± 0.02	...	0.2 ± 0.1
★ G168.72-15.4	0.14 ± 0.04	...	0.6 ± 0.2
★ G169.98-18.9	0.1 ± 0.03	...	0.2 ± 0.1
★ G171.51-10.5	0.07 ± 0.02	...	0.2 ± 0.1
★ G202.30-08.9	0.13 ± 0.03	...	0.2 ± 0.1

Note. Column 1: source name, the sources marked with “★” before source name were observed with the high velocity resolution mode (AROWS mode 13) and the rest were observed with the low velocity resolution mode (AROWS mode 3); Column 2: velocity integrated intensity; Column 3: local standard of rest velocity; Column 4: full width at half maximum. The V_{LSR} values are not provided here, as described in the notes for Table 5.

Table 7: $D_{\text{frac}}(\text{HCO}^+)$ and $D_{\text{frac}}(\text{HCN})$.

Source Name	$W(\text{DCO}^+)$ (K·km s ⁻¹)	$W(\text{DCN})$ (K·km s ⁻¹)	$W(\text{H}^{13}\text{CO}^+)$ (K·km s ⁻¹)	$W(\text{H}^{13}\text{CN})$ (K·km s ⁻¹)	$D_{\text{frac}}(\text{HCO}^+)$ %	$D_{\text{frac}}(\text{HCN})$ %
G001.38+20.9	1.44 ± 0.04	0.23 ± 0.05	0.76 ± 0.02	0.08 ± 0.02	3.7 ± 0.1	5.5 ± 1.8
G001.84+16.5	1.35 ± 0.04	0.13 ± 0.03	0.64 ± 0.02	≤0.04	4.1 ± 0.2	≥6.2
G003.73+16.3	0.22 ± 0.03	≤0.06	0.2 ± 0.02	≤0.04	2.1 ± 0.4	
G003.73+18.3	0.23 ± 0.04	≤0.07	0.28 ± 0.02	≤0.04	1.6 ± 0.3	
G004.46+16.6	0.16 ± 0.02	≤0.05	0.14 ± 0.02	0.09 ± 0.03	2.2 ± 0.4	≤1.1
G006.04+36.7	1.03 ± 0.05	≤0.11	0.4 ± 0.02	0.06 ± 0.02	5.0 ± 0.3	≤3.5
G006.32+20.4	0.77 ± 0.03	≤0.06	0.33 ± 0.02	≤0.04	4.6 ± 0.3	
G006.41+20.5	0.48 ± 0.03	≤0.07	0.28 ± 0.03	≤0.05	3.3 ± 0.4	
G006.70+20.6	0.34 ± 0.05	≤0.1	0.39 ± 0.03	0.06 ± 0.02	1.7 ± 0.3	≤3.2
G006.94+05.8	0.23 ± 0.05	≤0.11	0.16 ± 0.03	≤0.07	2.8 ± 0.8	
G006.98+20.7	0.14 ± 0.03	≤0.07				
G007.14+05.9	0.4 ± 0.06	≤0.12	0.2 ± 0.03	≤0.06	3.9 ± 0.8	
G008.52+21.8	0.48 ± 0.03	≤0.07	0.36 ± 0.02	≤0.04	2.6 ± 0.2	
G008.67+22.1	0.22 ± 0.04	≤0.07	0.11 ± 0.02	0.06 ± 0.02	3.9 ± 1.0	≤2.2
G021.20+04.9	0.39 ± 0.05	≤0.11	0.24 ± 0.02	0.07 ± 0.02	3.2 ± 0.5	≤3.0
G021.66+03.7	1.14 ± 0.06	0.21 ± 0.06	0.61 ± 0.03	≤0.05	3.6 ± 0.3	≥8.1
G025.48+06.1	0.57 ± 0.05	≤0.09	0.46 ± 0.02	0.1 ± 0.02	2.4 ± 0.2	≤1.7
G026.85+06.7	0.45 ± 0.04	0.15 ± 0.04	0.34 ± 0.02	0.07 ± 0.02	2.6 ± 0.3	4.1 ± 1.6
G027.66+05.7	0.33 ± 0.04	≤0.08	0.2 ± 0.02	≤0.04	3.2 ± 0.5	
G028.45-06.3	0.43 ± 0.04	0.1 ± 0.03	0.57 ± 0.02	0.07 ± 0.02	1.5 ± 0.1	2.7 ± 1.1
G028.71+03.8	0.96 ± 0.05	0.19 ± 0.03	0.53 ± 0.03	0.15 ± 0.02	3.5 ± 0.3	2.4 ± 0.5
G028.87+04.2	0.16 ± 0.03	≤0.04	0.25 ± 0.03	≤0.08	1.2 ± 0.3	
G030.43+02.3	0.37 ± 0.04	≤0.08	0.32 ± 0.03	0.05 ± 0.02	2.3 ± 0.3	≤3.1
G030.78+05.2	1.1 ± 0.05	≤0.11	0.93 ± 0.03	0.28 ± 0.04	2.3 ± 0.1	≤0.8
G031.44+04.1	0.42 ± 0.04	≤0.09	0.33 ± 0.02	0.05 ± 0.02	2.5 ± 0.3	≤3.5
G032.93+02.6	0.78 ± 0.04	≤0.09	0.51 ± 0.03	0.07 ± 0.03	3.0 ± 0.2	≤2.5
G038.36-00.9	0.67 ± 0.06	≤0.16	0.81 ± 0.04	0.16 ± 0.03	1.6 ± 0.2	≤1.9
G043.02+08.3	0.21 ± 0.03	≤0.06	0.1 ± 0.02	≤0.03	4.1 ± 1.0	
G048.40-05.8	0.25 ± 0.03	≤0.06	0.14 ± 0.02	≤0.03	3.5 ± 0.6	
G057.10+03.6	0.49 ± 0.05	≤0.09	0.41 ± 0.03	≤0.07	2.3 ± 0.3	
G058.16+03.5	0.21 ± 0.03	≤0.06	0.25 ± 0.02	0.05 ± 0.02	1.6 ± 0.3	≤2.3
G060.75-01.2	0.25 ± 0.04	≤0.09	0.3 ± 0.04	≤0.06	1.6 ± 0.3	
G065.43-03.1	0.2 ± 0.06	≤0.14				
G070.44-01.5	0.43 ± 0.07	≤0.12	0.36 ± 0.04	≤0.08	2.3 ± 0.5	
G074.11+00.1	0.74 ± 0.06	≤0.16	0.6 ± 0.06	≤0.12	2.4 ± 0.3	
G084.79-01.1	2.37 ± 0.19	0.44 ± 0.08	1.11 ± 0.06	0.24 ± 0.04	4.2 ± 0.4	3.5 ± 0.9
G089.36-00.6	0.3 ± 0.04	≤0.08	0.26 ± 0.04	≤0.07	2.2 ± 0.5	
G089.62+02.1	0.58 ± 0.04	0.14 ± 0.04	0.29 ± 0.03	≤0.06	3.9 ± 0.5	≥4.5
G089.93-07.0	0.18 ± 0.03	≤0.07	0.11 ± 0.02	≤0.04	3.2 ± 0.8	
G091.29-38.1	≤0.09	0.17 ± 0.05				
G091.73+04.3	1.17 ± 0.05	0.25 ± 0.05	0.58 ± 0.04	≤0.07	3.9 ± 0.3	≥6.9
G092.02+03.9	0.26 ± 0.04	≤0.09	0.2 ± 0.03	≤0.06	2.5 ± 0.5	
G092.26+03.8	0.53 ± 0.04	≤0.11	0.22 ± 0.03	≤0.07	4.7 ± 0.7	
G093.20+09.5	0.18 ± 0.04	≤0.07				
G093.62-04.4	0.53 ± 0.05	≤0.09	0.19 ± 0.03	≤0.07	5.4 ± 1.0	
G093.99-04.9	0.23 ± 0.05	≤0.1	0.24 ± 0.05	≤0.12	1.9 ± 0.6	
G094.08+09.4	0.36 ± 0.05	≤0.1	0.19 ± 0.02	≤0.05	3.7 ± 0.6	
G095.51+09.9	0.12 ± 0.02	≤0.05	0.15 ± 0.03	≤0.05	1.6 ± 0.4	
G096.94+10.2	0.36 ± 0.04	≤0.07	0.18 ± 0.02	≤0.05	3.9 ± 0.6	
G097.09+10.1	0.31 ± 0.04	≤0.09	0.16 ± 0.03	≤0.05	3.8 ± 0.9	
G097.20+09.8	0.54 ± 0.05	≤0.08	0.23 ± 0.03	≤0.06	4.6 ± 0.7	
G097.38+09.9	0.2 ± 0.05	≤0.1	0.15 ± 0.03	≤0.06	2.6 ± 0.8	
G102.34+15.9	0.63 ± 0.04	≤0.08	0.35 ± 0.02	≤0.05	3.5 ± 0.3	
G102.72+15.3	0.44 ± 0.04	≤0.08	0.24 ± 0.02	0.05 ± 0.02	3.6 ± 0.4	≤3.1
G103.90+13.9	0.3 ± 0.04	≤0.08	0.41 ± 0.02	0.15 ± 0.03	1.4 ± 0.2	≤1.0
G108.10+13.1	0.36 ± 0.04	≤0.08	0.22 ± 0.03	≤0.05	3.2 ± 0.6	
G108.85-00.8	0.41 ± 0.05	≤0.1	0.24 ± 0.04	≤0.09	3.3 ± 0.7	
G110.65+09.6	0.78 ± 0.05	≤0.1	0.5 ± 0.05	≤0.09	3.0 ± 0.4	
G111.66+20.2	0.91 ± 0.05	≤0.13	0.43 ± 0.03	0.11 ± 0.03	4.1 ± 0.4	≤2.3

Table 7: continue.

Source Name	W(DCO ⁺) (K·km s ⁻¹)	W(DCN) (K·km s ⁻¹)	W(H ¹³ CO ⁺) (K·km s ⁻¹)	W(H ¹³ CN) (K·km s ⁻¹)	$D_{\text{frac}}(\text{HCO}^+)$ %	$D_{\text{frac}}(\text{HCN})$ %
G113.75+14.9	0.1 ± 0.03	≤0.08				
G114.16+14.8	0.35 ± 0.04	≤0.1	0.24 ± 0.03	≤0.05	2.8 ± 0.5	
G114.56+14.7	0.11 ± 0.03	≤0.07	0.11 ± 0.04	≤0.08	1.9 ± 0.9	
G114.67+14.4	2.12 ± 0.06	0.28 ± 0.06	0.88 ± 0.04	≤0.08	4.7 ± 0.3	≥6.7
G115.81-03.5	0.35 ± 0.04	≤0.09	0.1 ± 0.03	≤0.05	6.8 ± 2.2	
G116.23+20.3	≤0.08	0.11 ± 0.02				
G117.11+12.4	0.63 ± 0.04	≤0.11	0.37 ± 0.03	≤0.06	3.3 ± 0.3	
G120.16+03.0	0.67 ± 0.06	≤0.15	0.54 ± 0.07	≤0.13	2.4 ± 0.4	
G120.67+02.6	0.38 ± 0.06	≤0.12	0.31 ± 0.05	≤0.1	2.4 ± 0.5	
G120.98+02.6	0.17 ± 0.05	≤0.1				
G121.35+03.3	0.29 ± 0.04	≤0.07	0.15 ± 0.04	0.07 ± 0.02	3.8 ± 1.1	≤1.9
G126.95-01.0	0.21 ± 0.04	≤0.09				
G127.66+13.9	0.34 ± 0.06	≤0.12				
G127.85+14.1	0.35 ± 0.06	≤0.1				
G127.88+02.6	0.26 ± 0.07	≤0.12				
G128.89+13.6	0.8 ± 0.04	≤0.08				
G130.36+11.2	0.23 ± 0.06	≤0.16	0.16 ± 0.04	≤0.08	2.8 ± 1.0	
G132.03+08.9	0.21 ± 0.04	≤0.08	0.1 ± 0.03	≤0.07	4.1 ± 1.5	
G133.48+09.0	0.74 ± 0.13	≤0.21				
G136.31-01.7	0.27 ± 0.05	≤0.12				
G142.29+07.6	≤0.06	≤0.05	≤0.04	0.09 ± 0.02		≤1.1
G144.66+00.1	0.32 ± 0.05	≤0.1	0.18 ± 0.04	≤0.09	3.5 ± 0.9	
G147.01+03.3	0.44 ± 0.05	≤0.09				
G150.44+03.9	0.38 ± 0.05	≤0.1	0.1 ± 0.03	≤0.06	7.4 ± 2.4	
G151.08+04.4	0.29 ± 0.05	≤0.09	0.19 ± 0.03	≤0.06	3.0 ± 0.7	
G156.20+05.2	0.27 ± 0.05	≤0.1	0.22 ± 0.03	≤0.07	2.4 ± 0.6	
G157.54-04.0	0.12 ± 0.03	0.12 ± 0.03	0.07 ± 0.02	0.11 ± 0.03	3.3 ± 1.3	2.1 ± 0.8
G158.20-20.2	0.69 ± 0.06	≤0.09	0.33 ± 0.03	≤0.07	4.1 ± 0.5	
G158.22-20.1	0.13 ± 0.03	≤0.05	0.13 ± 0.02	≤0.05	1.9 ± 0.5	
G158.37-20.7	0.68 ± 0.08	≤0.15	0.31 ± 0.04	≤0.08	4.3 ± 0.7	
G159.01-08.4	0.17 ± 0.03	≤0.06	0.11 ± 0.03	≤0.07	3.0 ± 1.0	
G159.21-20.4	0.18 ± 0.04	≤0.07	0.18 ± 0.03	0.13 ± 0.03	1.9 ± 0.5	≤1.0
G159.21-20.1	2.2 ± 0.05	0.34 ± 0.04	1.0 ± 0.04	≤0.09	4.3 ± 0.2	≥7.3
G159.23-34.4	≤0.07	≤0.07	0.28 ± 0.03	≤0.06	≤0.5	
G159.34+11.2	≤0.06	0.13 ± 0.03	0.19 ± 0.02	0.16 ± 0.02	≤0.6	1.6 ± 0.4
G159.65-19.6	0.3 ± 0.06	≤0.08	0.12 ± 0.02	≤0.06	4.9 ± 1.3	
G160.53-09.8	0.19 ± 0.03	≤0.06	0.14 ± 0.04	≤0.06	2.6 ± 0.9	
G160.64-35.0	0.06 ± 0.02	0.14 ± 0.03	0.13 ± 0.02	0.13 ± 0.02	0.9 ± 0.3	2.1 ± 0.5
G161.85-35.7	0.19 ± 0.05	0.13 ± 0.03	0.2 ± 0.03	0.17 ± 0.02	1.9 ± 0.6	1.5 ± 0.4
G161.85-08.6	0.21 ± 0.05	≤0.09	≤0.07	≤0.07	≥5.8	
G162.64-31.6	≤0.06	0.12 ± 0.03	0.08 ± 0.02	0.1 ± 0.03	≤1.5	2.3 ± 0.9
G163.32-08.4	0.1 ± 0.03	≤0.05	≤0.04	≤0.04	≥4.9	
G163.67-08.3	0.17 ± 0.04	≤0.07	0.16 ± 0.03	≤0.07	2.1 ± 0.6	
G164.75-24.1	0.1 ± 0.02	0.2 ± 0.03	0.22 ± 0.02	0.21 ± 0.02	0.9 ± 0.2	1.8 ± 0.3
G164.94-08.5	1.01 ± 0.07	≤0.12	0.51 ± 0.04	≤0.09	3.9 ± 0.4	
G165.16-07.5	≤0.09	≤0.09	0.22 ± 0.03	≤0.09	≤0.8	
G165.69-09.1	0.27 ± 0.06	≤0.09	≤0.09	≤0.09	≥5.9	
G167.23-15.3	0.29 ± 0.05	≤0.11	0.22 ± 0.04	≤0.09	2.6 ± 0.6	
G168.00-15.6	≤0.1	≤0.09	0.42 ± 0.03	≤0.08	≤0.5	
G168.13-16.3	0.47 ± 0.05	≤0.09	0.22 ± 0.03	≤0.06	4.2 ± 0.7	
G168.72-15.4	0.73 ± 0.06	≤0.11	0.46 ± 0.03	0.14 ± 0.04	3.1 ± 0.3	≤1.5
G168.85-15.8	0.15 ± 0.04	≤0.08	≤0.06	≤0.06	≥4.9	
G169.32-16.1	0.76 ± 0.06	≤0.11	0.29 ± 0.03	≤0.08	5.1 ± 0.7	
G169.43-16.1	0.15 ± 0.04	≤0.06	0.19 ± 0.04	≤0.09	1.5 ± 0.5	
G169.76-16.1	0.54 ± 0.06	≤0.09	0.26 ± 0.03	≤0.06	4.0 ± 0.6	
G169.98-18.9	0.22 ± 0.04	≤0.09	0.31 ± 0.03	0.1 ± 0.03	1.4 ± 0.3	≤1.7
G170.00-16.1	0.31 ± 0.04	≤0.08	0.14 ± 0.03	≤0.06	4.3 ± 1.1	
G170.13-16.0	≤0.14	≤0.11	0.42 ± 0.04	≤0.09	≤0.7	
G170.26-16.0	0.48 ± 0.06	≤0.09	0.38 ± 0.04	≤0.08	2.5 ± 0.4	
G170.99-15.8	≤0.11	≤0.1	0.31 ± 0.04	≤0.08	≤0.7	

Table 7: continue.

Source Name	$W(\text{DCO}^+)$ (K·km s ⁻¹)	$W(\text{DCN})$ (K·km s ⁻¹)	$W(\text{H}^{13}\text{CO}^+)$ (K·km s ⁻¹)	$W(\text{H}^{13}\text{CN})$ (K·km s ⁻¹)	$D_{\text{frac}}(\text{HCO}^+)$ %	$D_{\text{frac}}(\text{HCN})$ %
G171.14-17.5	0.21 ± 0.05	≤ 0.09	0.18 ± 0.03	≤ 0.06	2.3 ± 0.7	
G171.34-10.6	0.16 ± 0.05	≤ 0.08	0.13 ± 0.03	≤ 0.06	2.4 ± 0.9	
G171.51-10.5	0.23 ± 0.04	≤ 0.08	0.18 ± 0.02	0.07 ± 0.02	2.5 ± 0.5	≤ 2.2
G171.84-05.2	0.47 ± 0.05	≤ 0.1	0.24 ± 0.03	≤ 0.06	3.8 ± 0.6	
G177.14-01.2	0.32 ± 0.06	≤ 0.11	≤ 0.08	≤ 0.08	≥ 7.8	
G177.86+01.0	0.17 ± 0.05	≤ 0.09	0.14 ± 0.03	≤ 0.08	2.4 ± 0.9	
G178.48-06.7	0.12 ± 0.03	≤ 0.06	≤ 0.05	≤ 0.05	≥ 4.7	
G178.98-06.7	0.45 ± 0.05	≤ 0.06	0.31 ± 0.02	≤ 0.05	2.8 ± 0.4	
G181.84+00.3	0.44 ± 0.06	≤ 0.11	≤ 0.08	≤ 0.08	≥ 10.7	
G185.33-02.1	0.16 ± 0.05	≤ 0.1	≤ 0.08	≤ 0.09	≥ 3.9	
G191.00-04.5	≤ 0.09	≤ 0.07	0.1 ± 0.02	≤ 0.07	≤ 1.8	
G192.32-11.8	0.77 ± 0.06	≤ 0.13	0.49 ± 0.04	≤ 0.09	3.1 ± 0.3	
G195.00-16.9	0.15 ± 0.04	≤ 0.08	≤ 0.06	≤ 0.06	≥ 4.9	
G195.09-16.4	≤ 0.05	≤ 0.05	0.06 ± 0.02	≤ 0.04	≤ 1.6	
G198.56-09.1	0.44 ± 0.04	0.1 ± 0.02	0.19 ± 0.02	≤ 0.06	4.5 ± 0.6	≥ 3.2
G199.88+00.9	0.47 ± 0.06	≤ 0.13	≤ 0.1	≤ 0.1	≥ 9.2	
G200.34-10.9	0.12 ± 0.03	≤ 0.05	≤ 0.04	≤ 0.04	≥ 5.8	
G201.13+00.3	0.39 ± 0.07	≤ 0.13	≤ 0.09	≤ 0.09	≥ 8.5	
G201.44+00.6	0.49 ± 0.05	≤ 0.1	0.19 ± 0.05	≤ 0.06	5.0 ± 1.4	
G202.30-08.9	0.26 ± 0.05	≤ 0.08	0.14 ± 0.02	0.13 ± 0.03	3.6 ± 0.9	≤ 1.2
G203.20-11.2	1.06 ± 0.07	≤ 0.14	0.6 ± 0.05	≤ 0.11	3.4 ± 0.4	
G204.49-11.3	0.2 ± 0.04	≤ 0.06	0.11 ± 0.02	≤ 0.05	3.5 ± 1.0	
G206.10-15.7 ¹	0.27 ± 0.06	≤ 0.08	0.13 ± 0.03	≤ 0.06	4.0 ± 1.3	
	0.37 ± 0.05	≤ 0.1	0.22 ± 0.03	≤ 0.07	3.3 ± 0.6	
G207.35-19.8	0.38 ± 0.06	≤ 0.11	0.13 ± 0.03	≤ 0.06	5.7 ± 1.6	
G209.28-19.6	0.62 ± 0.08	≤ 0.0	0.99 ± 0.06	≤ 0.0	1.2 ± 0.2	
G211.48-19.2	0.62 ± 0.08	≤ 0.11	0.31 ± 0.04	≤ 0.1	3.9 ± 0.7	
G212.10-19.1	0.59 ± 0.09	≤ 0.14	0.17 ± 0.05	≤ 0.08	6.8 ± 2.2	
G213.96-19.6	0.27 ± 0.05	≤ 0.09	0.24 ± 0.04	≤ 0.1	2.2 ± 0.5	
G214.43-19.9	0.2 ± 0.05	≤ 0.09	0.19 ± 0.04	≤ 0.08	2.1 ± 0.7	
G215.00-15.1	≤ 0.08	≤ 0.07	0.08 ± 0.02	≤ 0.06	≤ 1.9	
G216.18-15.2	≤ 0.13	≤ 0.12	0.15 ± 0.04	≤ 0.08	≤ 1.7	
G359.31+17.0	0.47 ± 0.04	≤ 0.06	0.34 ± 0.02	≤ 0.05	2.7 ± 0.3	

Note. Column 1: source name; Column 2~5: velocity integrated intensity or The 3σ upper limit value of DCO^+ , DCN , H^{13}CN and H^{13}CO^+ 1-0; Column 6~7: deuterated fraction of HCO^+ and HCN .

¹ G206.10-15.7 contains 2 velocity components

Appendix A: High spectral resolution supplementary observations with AROWS mode 5

As described in Section 2, high spectral resolution supplementary observations with AROWS mode 5 were conducted for DCO⁺ 1-0 narrow lines toward 32 sources. The fluxes of DCO⁺ 1-0 observed with the high velocity resolution mode (AROWS mode 5) are similar to those observed with the low velocity resolution mode (AROWS mode 3) (see Table A.1).

The FWHMs of DCO⁺ 1-0 using the high velocity resolution mode (AROWS mode 5) are compared with those using the low velocity resolution mode (AROWS mode 3) in Figure A1, showing similar values within the error bars. Therefore, even though the FWHMs from low spectral resolution observations may not be precise, they are still useful as a reference.

Table A.1: High spectral resolution DCO⁺ 1-0 observed with the high velocity resolution mode (AROWS mode 5).

Source Name	W (K·km s ⁻¹)	V_{LSR} (km s ⁻¹)	FWHM (km s ⁻¹)	$W(\text{DCO}^+)$ with mode 3 (K·km s ⁻¹)	$\frac{W(\text{DCO}^+) \text{ with mode 5}}{W(\text{DCO}^+) \text{ with mode 3}}$ ratio
G001.38+20.9	1.57 ± 0.04	0.7 ± 0.1	0.6 ± 0.1	1.44 ± 0.04	1.09 ± 0.04
G001.84+16.5	1.46 ± 0.05	5.8 ± 0.1	0.6 ± 0.1	1.35 ± 0.04	1.08 ± 0.05
G003.73+16.3	0.25 ± 0.04	6.0 ± 0.1	0.4 ± 0.1	0.22 ± 0.03	1.14 ± 0.21
G003.73+18.3	0.31 ± 0.05	4.3 ± 0.1	0.7 ± 0.1	0.23 ± 0.04	1.35 ± 0.24
G004.46+16.6	0.27 ± 0.04	5.6 ± 0.1	0.5 ± 0.1	0.16 ± 0.02	1.69 ± 0.19
G006.04+36.7	1.18 ± 0.04	2.5 ± 0.1	0.6 ± 0.1	1.03 ± 0.05	1.15 ± 0.06
G006.32+20.4	0.77 ± 0.04	4.2 ± 0.1	0.5 ± 0.1	0.77 ± 0.03	1.0 ± 0.06
G006.41+20.5	0.57 ± 0.04	4.4 ± 0.1	0.6 ± 0.1	0.48 ± 0.03	1.19 ± 0.09
G006.70+20.6	0.36 ± 0.04	3.5 ± 0.1	0.6 ± 0.1	0.34 ± 0.05	1.06 ± 0.18
G007.14+05.9	0.51 ± 0.07	10.3 ± 0.1	0.9 ± 0.1	0.4 ± 0.06	1.27 ± 0.2
G008.52+21.8	0.52 ± 0.03	3.8 ± 0.1	0.4 ± 0.1	0.48 ± 0.03	1.08 ± 0.09
G008.67+22.1	0.27 ± 0.03	3.5 ± 0.1	0.3 ± 0.1	0.22 ± 0.04	1.23 ± 0.21
G021.20+04.9	0.53 ± 0.04	3.5 ± 0.1	0.5 ± 0.1	0.39 ± 0.05	1.36 ± 0.15
G021.66+03.7	1.18 ± 0.05	6.7 ± 0.1	0.7 ± 0.1	1.14 ± 0.06	1.04 ± 0.07
G025.48+06.1	0.55 ± 0.04	7.7 ± 0.1	0.6 ± 0.1	0.57 ± 0.05	0.96 ± 0.11
G026.85+06.7	0.49 ± 0.04	7.1 ± 0.1	0.6 ± 0.1	0.45 ± 0.04	1.09 ± 0.12
G027.66+05.7	0.3 ± 0.04	8.2 ± 0.1	0.6 ± 0.1	0.33 ± 0.04	0.91 ± 0.18
G028.45-06.3	0.55 ± 0.04	12.2 ± 0.1	0.6 ± 0.1	0.43 ± 0.04	1.28 ± 0.12
G028.71+03.8	1.16 ± 0.05	7.6 ± 0.1	0.9 ± 0.1	0.96 ± 0.05	1.21 ± 0.07
G028.87+04.2	0.25 ± 0.04	6.6 ± 0.1	0.6 ± 0.1	0.16 ± 0.03	1.56 ± 0.25
G030.43+02.3	0.37 ± 0.05	9.1 ± 0.1	0.9 ± 0.1	0.37 ± 0.04	1.0 ± 0.17
G030.78+05.2	1.08 ± 0.05	8.2 ± 0.1	1.1 ± 0.1	1.1 ± 0.05	0.98 ± 0.06
G031.44+04.1	0.41 ± 0.04	11.0 ± 0.1	0.7 ± 0.1	0.42 ± 0.04	0.98 ± 0.14
G032.93+02.6	0.63 ± 0.04	11.7 ± 0.1	0.5 ± 0.1	0.78 ± 0.04	0.81 ± 0.08
G038.36-00.9	0.63 ± 0.05	16.6 ± 0.1	1.2 ± 0.1	0.67 ± 0.06	0.94 ± 0.12
G043.02+08.3	0.16 ± 0.02	4.0 ± 0.1	0.3 ± 0.1	0.21 ± 0.03	0.76 ± 0.19
G048.40-05.8	0.27 ± 0.03	9.6 ± 0.1	0.5 ± 0.1	0.25 ± 0.03	1.08 ± 0.16
G057.10+03.6	0.52 ± 0.05	11.7 ± 0.1	1.3 ± 0.1	0.49 ± 0.05	1.06 ± 0.14
G058.16+03.5	0.4 ± 0.04	9.9 ± 0.1	0.6 ± 0.1	0.21 ± 0.03	1.9 ± 0.17
G060.75-01.2	0.27 ± 0.04	10.8 ± 0.1	0.5 ± 0.1	0.25 ± 0.04	1.08 ± 0.22
G065.43-03.1	0.13 ± 0.03	6.2 ± 0.1	0.3 ± 0.1	0.2 ± 0.06	0.65 ± 0.38
G070.44-01.5	0.34 ± 0.06	11.0 ± 0.1	1.5 ± 0.2	0.43 ± 0.07	0.79 ± 0.24

Note. Column 1: source name; Column 2: velocity integrated intensity of DCO⁺ 1-0 with the high velocity resolution mode (AROWS mode 5); Column 3: local standard of rest velocity; Column 4: full width at half maximum; Column 5: velocity integrated intensity of DCO⁺ 1-0 with the low velocity resolution mode (AROWS mode 3); Column 6: ratio of velocity integrated intensity of DCO⁺ 1-0 with AROWS mode 5 to which with mode 3.

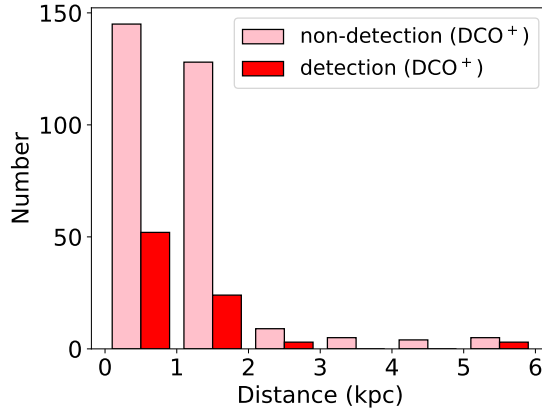


Fig. B1: Distribution of kinematic distance of sources where DCO⁺ 1-0 is detected or not.

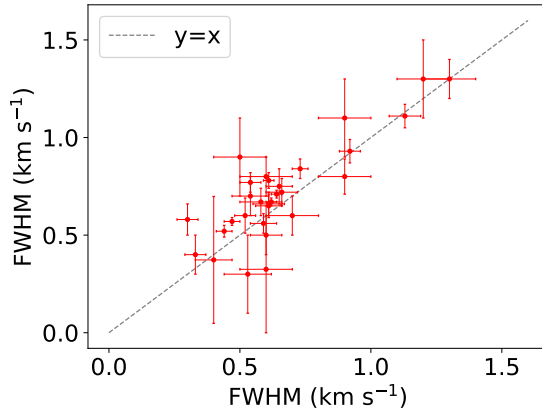


Fig. A1: Comparison between FWHM of DCO⁺ with velocity resolution $\sim 0.081 \text{ km s}^{-1}$ with mode 5 and FWHM of DCO⁺ with velocity resolution $\sim 0.32 \text{ km s}^{-1}$ with mode 3. There are 32 points in the plot.

Appendix B: The relationships of the kinematic distances of sources and detection results

To determine whether DCO⁺ 1-0 detection is limited by distance, the distributions of kinematic distances for sources with and without DCO⁺ 1-0 detections are shown in Figure B1. To reduce uncertainty in kinematic distances, sources located at galactic longitudes $0^\circ \pm 15^\circ$ and $90^\circ \pm 15^\circ$, as well as those with a galactic scale height greater than 1 kpc, were excluded. Among the observed sources, the kinematic distances for 378 sources that meet the coordinate requirements are from Wu et al. (2012). The kinematic distances of these sources, regardless of DCO⁺ 1-0 detection, show a similar distribution (see Figure B1). The kinematic distances of 82 sources with DCO⁺ 1-0 detections range from 0.11 to 5.75 kpc, with a mean of 1.08 kpc and a median value of 0.81 kpc. For the 296 sources without DCO⁺ 1-0 detections, kinematic distances range from 0.10 to 5.42 kpc, with a mean of 1.11 kpc and a median value of 1.01 kpc. The kinematic distances of sources with and without detections show similar distributions, means, and medians, which rules out the effect of beam dilution on the detection or non-detection status.

Appendix C: The sources without any detection

A total of 228 sources were observed for DCO⁺ and DCN 1-0 using the low velocity resolution mode (AROWS mode 3), with no detections of either molecule. The details for these 228 sources, including name, R.A., and Decl., are provided in Table C1. Additionally, Table C2 lists details for 180 sources observed with the high velocity resolution mode (AROWS mode 13) that showed no detection of DCO⁺, DCN, H¹³CO⁺, or H¹³CN 1-0.

Table C1: 228 sources without DCO⁺ or DCN 1-0 detection with the low velocity resolution mode (AROWS mode 3).

Source Name	R.A. (hh:mm:ss)	Decl. (dd:mm:ss)	Source Name	R.A. (hh:mm:ss)	Decl. (dd:mm:ss)
G004.02+16.6	16:55:10.45	-16:21:23.27	G004.15+35.7	15:53:29.82	-04:38:52.39
G004.17+36.6	15:50:42.66	-04:04:20.84	G004.19+18.0	16:50:42.47	-15:22:25.13
G004.41+15.9	16:58:35.99	-16:28:36.07	G004.54+36.7	15:51:14.27	-03:47:40.14

Table C1: continue.

Source Name	R.A. (hh:mm:ss)	Decl. (dd:mm:ss)	Source Name	R.A. (hh:mm:ss)	Decl. (dd:mm:ss)
G004.81+37.0	15:50:52.79	-03:27:20.38	G004.92+17.9	16:52:50.41	-14:53:40.51
G005.03+19.0	16:49:19.74	-14:09:20.80	G005.29+11.0	17:17:19.97	-18:30:57.71
G005.29+14.4	17:05:31.09	-16:36:07.96	G005.31+10.7	17:18:23.02	-18:39:22.30
G005.69+36.8	15:53:11.88	-03:00:56.50	G005.80+19.9	16:48:13.56	-13:04:14.26
G006.08+20.2	16:47:44.35	-12:39:21.78	G006.96+00.8	17:57:59.28	-22:29:20.42
G007.53+21.1	16:48:08.77	-11:03:53.56	G007.80+21.1	16:48:43.20	-10:51:47.54
G008.43+36.3	16:00:02.55	-01:32:25.18	G009.62+21.2	16:52:01.63	-09:21:33.98
G011.09+03.4	17:57:24.13	-17:38:42.83	G011.40+36.1	16:06:03.58	+00:19:32.84
G013.86+04.5	17:59:03.17	-14:41:26.77	G014.74+04.0	18:02:34.88	-14:09:59.84
G014.87+19.6	17:08:24.20	-06:07:18.26	G015.16+07.2	17:52:06.35	-12:14:27.93
G016.67-02.7	18:31:16.07	-15:42:41.22	G017.22-01.4	18:27:35.34	-14:37:44.09
G018.39+19.3	17:16:04.31	-03:24:13.42	G018.61+08.8	17:53:10.33	-08:27:42.53
G019.86+20.4	17:15:20.84	-01:41:55.70	G020.52+01.6	18:22:24.56	-10:14:01.42
G021.26+12.1	17:46:54.19	-04:35:51.36	G023.33+11.8	17:51:52.37	-02:58:23.38
G023.37+08.2	18:04:38.79	-04:38:50.91	G023.68+07.5	18:07:37.30	-04:41:59.16
G026.45+08.0	18:11:02.76	-02:02:51.60	G026.93-20.6	19:56:07.08	-14:21:30.47
G027.09-20.7	19:56:26.08	-14:14:06.47	G027.70-21.0	19:58:36.21	-13:50:25.40
G028.56-00.2	18:44:19.42	-03:59:49.18	G031.26-05.3	19:07:35.28	-03:55:38.37
G032.38-15.2	19:45:07.40	-07:22:03.75	G033.70-00.0	18:52:54.94	+00:40:49.67
G034.69-06.5	19:18:04.25	-01:26:07.30	G035.13+11.3	18:14:42.06	+07:05:34.57
G037.51+44.5	16:10:54.35	+21:45:37.26	G046.75-07.6	19:44:32.57	+08:36:47.86
G047.74-05.5	19:38:56.88	+10:30:04.67	G048.25-05.7	19:40:32.47	+10:51:33.54
G048.82-03.8	19:34:50.76	+12:16:54.25	G049.06-04.1	19:36:35.77	+12:19:16.42
G049.76-07.2	19:48:57.29	+11:25:36.57	G052.99+03.0	19:17:48.77	+19:13:58.55
G054.03-02.3	19:40:07.84	+17:31:24.94	G056.84+04.8	19:18:50.12	+23:26:16.08
G057.08+04.4	19:20:41.76	+23:29:11.33	G057.17+03.4	19:24:54.22	+23:04:26.60
G057.26+04.0	19:22:47.03	+23:25:56.16	G058.02+03.0	19:28:10.41	+23:38:31.75
G058.97-01.6	19:47:54.71	+22:10:14.34	G061.76-10.8	20:27:23.05	+19:38:21.54
G065.30-08.4	20:27:28.71	+23:51:10.63	G070.72-00.6	20:11:52.55	+32:42:33.25
G084.11+15.5	19:30:41.46	+52:11:22.10	G089.03-41.2	23:08:43.43	+14:43:35.71
G089.29+04.0	20:50:37.89	+50:27:04.95	G089.64-06.5	21:37:06.74	+43:22:02.80
G089.64-06.8	21:38:04.87	+43:10:20.80	G089.75-02.1	21:20:13.68	+46:39:03.34
G089.93-01.9	21:20:01.36	+46:56:00.17	G090.76-04.5	21:34:00.07	+45:37:39.81
G092.48-02.6	21:33:49.01	+48:11:19.11	G092.79+09.1	20:37:43.27	+56:20:13.73
G092.83-11.0	22:05:41.29	+41:56:59.39	G093.12-10.4	22:04:52.01	+42:37:09.24
G093.16+09.6	20:36:31.49	+56:54:48.32	G093.22-04.5	21:44:47.75	+47:13:40.19
G093.31-11.6	22:09:47.90	+41:42:41.79	G093.36-12.0	22:11:10.90	+41:25:42.25
G093.44-04.6	21:46:03.92	+47:18:45.57	G093.51-04.3	21:45:00.01	+47:37:34.10
G093.66+04.6	21:05:57.29	+54:11:19.51	G093.69+09.9	20:36:30.71	+57:33:22.77
G093.75-04.5	21:47:09.99	+47:34:03.01	G093.91+10.0	20:37:13.90	+57:45:13.58
G095.11+06.5	21:03:02.13	+56:29:14.76	G095.29-09.6	22:12:00.39	+44:28:46.38
G095.75+08.1	20:56:39.58	+58:03:19.36	G095.97+08.1	20:57:43.02	+58:13:20.01
G096.30+10.0	20:48:15.70	+59:37:39.53	G096.37+10.2	20:46:47.60	+59:51:10.72
G097.71+15.3	20:17:47.47	+63:46:21.34	G097.77+08.5	21:04:16.83	+59:50:45.96
G097.80+15.2	20:19:05.20	+63:47:07.60	G097.84+15.3	20:18:23.05	+63:52:53.91
G098.06+13.9	20:29:40.72	+63:20:29.47	G098.10+15.8	20:15:36.11	+64:21:24.43
G098.50-03.2	22:05:00.08	+51:33:11.74	G098.52+13.8	20:32:37.51	+63:39:38.00
G098.96+13.6	20:36:14.53	+63:54:15.88	G099.11+13.9	20:34:50.84	+64:11:26.96
G099.97+14.7	20:33:04.55	+65:19:14.44	G100.32+14.8	20:34:17.00	+65:38:45.35
G100.45+14.9	20:34:02.37	+65:48:58.56	G101.14-15.2	22:54:59.56	+42:36:10.85
G101.49+16.8	20:23:43.33	+67:38:41.41	G101.62-28.8	23:24:47.63	+30:25:04.98
G101.88+15.1	20:40:04.56	+67:04:28.98	G102.17+07.2	21:37:08.54	+62:02:13.09
G102.19+15.2	20:41:10.70	+67:21:44.30	G102.70+15.1	20:44:37.79	+67:43:34.88
G102.72-25.9	23:24:03.29	+33:26:00.51	G103.18-17.0	23:08:44.22	+41:48:19.98
G103.22-15.2	23:04:48.15	+43:31:27.62	G103.49+13.0	21:06:51.57	+67:01:15.21
G103.77+13.9	21:02:09.15	+67:45:51.82	G104.06+12.1	21:17:20.80	+66:51:02.09
G104.88+11.4	21:27:31.69	+66:52:14.83	G105.55+10.4	21:40:37.38	+66:36:13.43
G106.30+13.5	21:22:40.15	+69:23:07.62	G106.89+16.7	20:58:22.50	+71:52:40.57
G107.51-09.3	23:13:52.32	+50:33:37.76	G107.64-09.2	23:14:27.39	+50:40:44.41
G108.23+15.6	21:20:05.68	+72:08:51.84	G110.41+11.5	22:13:42.51	+70:27:51.52

Table C1: continue.

Source Name	R.A. (hh:mm:ss)	Decl. (dd:mm:ss)	Source Name	R.A. (hh:mm:ss)	Decl. (dd:mm:ss)
G110.52+19.1	21:00:37.84	+76:06:21.30	G110.54+11.9	22:12:18.79	+70:50:58.56
G110.76+19.4	20:59:29.33	+76:26:33.85	G110.76+20.1	20:48:51.71	+76:52:51.23
G110.96+19.4	21:00:35.97	+76:37:38.72	G111.46+20.1	20:55:39.95	+77:25:18.28
G111.68+19.7	21:04:19.81	+77:19:35.11	G111.77+13.7	22:10:39.25	+73:04:17.94
G111.77+20.2	20:57:36.58	+77:42:08.09	G111.97+20.5	20:55:40.82	+78:00:13.92
G112.03+17.8	21:32:42.81	+76:21:26.12	G112.25+13.8	22:15:37.52	+73:22:36.95
G112.52+08.3	22:52:47.61	+68:49:28.29	G112.60+08.5	22:52:54.76	+68:59:53.89
G112.63+20.8	20:58:19.23	+78:40:03.24	G113.42+16.9	21:59:58.99	+76:34:08.73
G113.62+15.0	22:21:37.31	+75:06:33.49	G114.41-13.9	00:01:41.52	+48:06:29.81
G115.92+09.4	23:24:04.62	+71:08:08.73	G116.01+09.1	23:26:27.92	+70:50:36.54
G116.08-02.3	23:56:41.78	+59:45:13.21	G116.12+08.9	23:28:14.03	+70:45:12.43
G116.25+20.1	22:00:24.54	+80:45:10.68	G116.30+12.2	23:15:19.75	+73:54:48.36
G118.14+08.8	23:52:17.36	+71:09:30.48	G118.25-52.7	00:39:55.42	+10:03:41.94
G118.34+08.6	23:55:06.71	+71:02:12.60	G118.36+21.7	22:16:54.81	+83:11:56.16
G121.57+23.3	23:37:23.24	+86:04:27.40	G121.99+24.2	23:45:20.96	+86:59:07.74
G122.73+09.6	00:48:54.75	+72:29:01.64	G123.66+24.8	01:57:28.86	+87:40:07.76
G123.74+24.7	02:01:24.04	+87:31:40.15	G125.17+11.6	01:24:12.50	+74:22:20.01
G125.70+12.5	01:33:57.65	+75:09:47.66	G126.62+24.5	04:23:16.95	+85:47:11.88
G126.65-71.4	00:56:13.82	-08:36:07.67	G127.31-70.0	00:57:27.24	-07:16:29.84
G128.25+20.7	03:25:46.87	+82:00:25.06	G128.95-00.1	01:43:15.17	+62:04:39.07
G128.95+04.4	01:52:32.86	+66:35:51.19	G129.90+11.6	02:28:23.83	+73:10:13.46
G129.94+11.7	02:29:32.62	+73:15:36.66	G129.96+13.7	02:41:53.27	+75:07:36.03
G130.14+11.0	02:28:35.31	+72:34:12.58	G130.14+11.6	02:31:43.16	+73:08:00.74
G130.14+13.7	02:44:17.12	+75:03:12.38	G130.56+11.5	02:35:56.34	+72:48:55.42
G131.35-45.7	01:15:57.51	+16:44:08.07	G131.72+09.7	02:39:57.52	+70:42:11.57
G132.07+08.8	02:39:18.18	+69:44:01.08	G142.49+07.4	03:59:13.57	+62:58:52.39
G142.62+07.2	03:59:00.65	+62:45:12.55	G144.44+08.5	04:17:58.86	+62:26:51.41
G144.66+06.1	04:05:12.80	+60:31:21.52	G144.84+00.7	03:40:20.81	+56:16:28.14
G146.71+02.0	03:56:37.15	+56:07:23.12	G147.96-08.0	03:24:02.12	+47:17:29.48
G150.35-38.0	02:22:11.93	+19:55:36.57	G151.58-38.5	02:24:53.06	+19:01:47.06
G111.33+19.9	20:57:51.09	+77:10:53.64	G058.07+03.2	19:27:32.78	+23:46:10.07
G111.04+14.0	22:00:56.89	+72:50:36.21	G111.42+19.8	21:00:27.72	+77:10:37.45
G118.08-09.6	00:19:40.63	+52:53:01.30	G121.50-20.9	00:44:17.38	+41:55:48.07
G121.88-08.7	00:44:21.66	+54:05:40.39	G121.90-01.5	00:42:52.65	+61:18:23.22
G121.92-07.6	00:44:27.19	+55:11:17.99	G122.01-07.4	00:45:01.81	+55:22:43.33
G122.18-10.2	00:46:37.80	+52:35:20.75	G122.62-12.1	00:49:34.09	+50:43:53.45
G125.66-00.5	01:14:52.21	+62:11:16.63	G125.77+04.1	01:20:18.22	+66:50:16.42
G126.27+05.1	01:26:45.93	+67:45:33.07	G126.49-01.3	01:21:14.55	+61:21:34.60
G126.73+06.1	01:33:23.87	+68:44:47.63	G127.79+13.6	02:09:57.71	+75:48:51.99
G128.21+13.7	02:16:18.66	+75:42:10.64	G129.22+15.1	02:40:47.35	+76:41:22.13
G132.07+13.6	03:08:01.25	+74:01:34.48	G132.27+13.2	03:07:42.40	+73:36:53.35
G132.29+09.3	02:44:21.76	+70:09:28.58	G133.28+08.8	02:51:42.23	+69:14:13.43
G133.72-45.3	01:23:04.84	+16:53:32.68	G135.08+12.9	03:35:45.37	+71:47:59.17
G135.28+12.9	03:37:34.32	+71:40:05.98	G143.85+11.4	04:33:38.01	+64:53:16.90
G144.49+08.7	04:19:10.27	+62:31:24.89	G145.81+10.9	04:41:31.46	+63:06:01.71
G146.18+08.8	04:29:36.20	+61:22:56.86	G148.00+00.0	03:54:48.04	+53:47:19.87
G148.24+00.4	03:57:26.19	+53:52:36.34	G149.52-01.2	03:56:52.62	+51:48:01.74
G149.58+03.4	04:18:23.92	+55:13:30.60	G154.48-15.1	03:30:19.60	+37:46:39.05
G154.68-15.3	03:30:35.18	+37:31:28.11	G154.95-15.1	03:32:04.91	+37:29:53.83
G155.45-14.5	03:35:51.95	+37:41:02.89	G359.97+21.9	16:28:06.76	-16:12:17.13
G159.52+03.2	04:59:55.06	+47:40:52.24	G127.22-02.2	01:26:10.18	+60:19:29.25

Table C2: 180 sources without DCO⁺, DCN, H¹³CO⁺ and H¹³CN 1-0 detection with the high velocity resolution mode (AROWS mode 13).

Source Name	R.A. (hh:mm:ss)	Decl. (dd:mm:ss)	Source Name	R.A. (hh:mm:ss)	Decl. (dd:mm:ss)
G121.92-01.7	00:43:06.34	+61:08:21.60	G140.97+05.7	03:39:23.31	+62:33:59.78
G149.23+03.0	04:14:48.52	+55:12:03.26	G149.41+03.3	04:17:09.05	+55:17:39.36

Table C2: continue.

Source Name	R.A. (hh:mm:ss)	Decl. (dd:mm:ss)	Source Name	R.A. (hh:mm:ss)	Decl. (dd:mm:ss)
G149.65+03.5	04:19:11.24	+55:14:44.38	G150.22+03.9	04:23:51.69	+55:06:22.47
G151.45+03.9	04:29:56.24	+54:14:51.71	G153.34-08.0	03:48:42.73	+44:08:46.62
G153.34+11.2	05:19:01.04	+57:19:44.78	G153.74+35.9	08:36:34.59	+62:26:27.09
G154.07+05.0	04:47:23.37	+53:03:31.39	G154.07+05.2	04:47:57.79	+53:07:51.21
G154.55-01.2	04:19:58.35	+48:23:32.14	G154.90+04.6	04:48:27.03	+52:06:30.37
G155.52-08.9	03:54:34.60	+42:03:48.96	G155.67+05.1	04:54:08.58	+51:50:10.93
G156.04+06.0	05:00:19.24	+52:06:45.62	G156.42+32.5	08:06:27.98	+60:34:20.05
G156.53-08.6	03:59:41.99	+41:38:26.63	G156.90-08.4	04:01:38.87	+41:29:43.41
G156.92-09.7	03:57:26.44	+40:33:29.15	G157.10-08.7	04:01:41.53	+41:12:37.45
G157.12-11.5	03:51:59.15	+39:01:55.10	G157.19-08.8	04:01:38.24	+41:04:05.05
G157.25-01.0	04:32:09.45	+46:37:25.02	G157.58-08.8	04:02:54.80	+40:45:04.96
G157.60-12.1	03:51:49.54	+38:15:38.76	G157.91-08.2	04:06:32.28	+41:01:15.73
G158.24-21.8	03:25:13.67	+30:19:30.39	G158.40-21.8	03:25:35.50	+30:11:29.55
G158.77-33.3	02:57:33.29	+20:38:31.01	G158.86-21.6	03:27:54.15	+30:08:33.87
G158.88-34.1	02:55:48.23	+19:51:50.97	G158.97-33.0	02:58:50.03	+20:47:23.13
G159.03-08.3	04:10:28.53	+40:11:46.78	G159.14-08.7	04:09:20.14	+39:48:21.73
G159.16-05.5	04:21:08.38	+42:04:14.47	G159.34-24.3	03:21:51.73	+27:38:19.30
G159.36+03.7	05:01:43.99	+48:06:42.77	G159.41-34.3	02:56:54.67	+19:28:15.70
G159.58-32.8	03:01:05.17	+20:38:43.23	G159.65+11.3	05:42:16.93	+52:07:48.14
G159.67-05.7	04:22:32.37	+41:37:15.79	G159.67-34.3	02:57:46.94	+19:23:09.02
G159.76-19.6	03:36:37.75	+31:10:57.96	G159.78-24.8	03:22:11.99	+27:04:15.40
G159.82-10.4	04:05:49.63	+38:05:19.15	G160.33+03.2	05:02:45.93	+47:01:41.07
G160.35-06.3	04:22:34.71	+40:40:40.18	G160.51-16.8	03:47:34.31	+32:53:12.17
G160.51-17.0	03:46:51.18	+32:42:28.95	G160.53-19.7	03:38:58.11	+30:39:04.72
G160.62-16.7	03:48:22.46	+32:55:21.25	G160.83-09.4	04:13:04.61	+38:08:51.19
G161.08-21.7	03:34:51.38	+28:43:51.87	G161.21-08.7	04:17:02.75	+38:24:57.50
G161.34-09.3	04:15:21.52	+37:53:39.42	G161.43-35.5	02:59:41.08	+17:30:58.04
G161.60-08.3	04:19:49.16	+38:24:23.05	G162.24-09.0	04:19:33.27	+37:28:03.29
G162.46-08.7	04:21:32.60	+37:33:04.74	G162.79+01.3	05:02:42.86	+43:55:05.65
G162.83-18.4	03:50:32.04	+30:13:17.24	G162.86-05.2	04:35:48.53	+39:38:08.62
G162.90-08.6	04:23:20.51	+37:17:33.45	G163.21-08.4	04:25:13.29	+37:13:48.93
G163.82-08.3	04:27:35.71	+36:50:26.29	G164.13-08.8	04:26:43.25	+36:15:25.18
G164.57-24.4	03:38:12.61	+24:36:13.41	G164.81-05.6	04:40:47.51	+37:53:40.02
G164.92-12.6	04:16:04.53	+33:03:27.18	G164.94-05.7	04:41:05.14	+37:46:15.50
G165.34-07.5	04:35:37.43	+36:16:57.13	G165.91-44.0	02:50:21.82	+08:41:43.64
G166.70-15.0	04:13:45.64	+30:08:25.67	G166.99-15.3	04:13:42.01	+29:44:26.31
G168.46-17.9	04:09:48.87	+26:55:07.96	G168.85-14.7	04:21:32.29	+28:52:48.43
G169.14-01.1	05:12:20.07	+37:20:57.12	G169.82-19.3	04:09:12.03	+24:58:39.00
G169.84-07.6	04:49:23.31	+32:49:47.26	G169.98-04.2	05:02:22.42	+34:48:06.81
G170.57-07.8	04:50:38.52	+32:07:05.91	G170.77-08.5	04:48:49.00	+31:33:00.09
G170.81-18.3	04:15:23.21	+25:01:23.84	G170.83-15.9	04:23:24.42	+26:39:55.87
G170.88-10.9	04:40:32.71	+29:55:42.61	G171.03+02.6	05:33:35.42	+37:56:42.68
G171.32+04.4	05:41:51.47	+38:37:50.74	G171.34+02.5	05:34:06.95	+37:38:47.28
G171.43-17.3	04:20:19.19	+25:15:38.94	G171.78-08.4	04:52:01.90	+30:49:13.60
G171.80-09.7	04:47:15.73	+29:57:33.86	G172.15-09.9	04:47:43.89	+29:35:43.25
G172.30-09.9	04:48:14.33	+29:29:23.26	G172.85+02.2	05:36:51.80	+36:11:58.25
G172.94-05.4	05:06:15.78	+31:42:39.02	G173.10+07.2	05:58:56.30	+38:31:58.92
G173.18-09.1	04:53:34.39	+29:18:35.60	G173.45-05.4	05:07:52.92	+31:20:25.45
G173.78-05.2	05:09:25.64	+31:10:33.56	G174.81+05.9	05:57:31.74	+36:25:24.39
G174.99-04.8	05:14:20.24	+30:27:09.32	G175.20+01.2	05:38:55.10	+33:41:05.90
G175.53+01.3	05:39:59.24	+33:26:08.78	G176.17-02.1	05:27:55.18	+31:01:35.04
G176.35+01.9	05:44:23.17	+33:02:58.95	G176.37-02.0	05:28:38.86	+30:53:34.32
G176.94+04.6	05:57:00.76	+33:55:16.25	G177.09+02.8	05:50:02.13	+32:53:35.85
G178.28-00.6	05:39:03.83	+30:04:05.92	G178.72-07.0	05:15:59.71	+26:09:46.55
G179.14-06.2	05:19:43.91	+26:14:18.94	G179.29+04.2	06:00:44.85	+31:40:15.04
G179.40+04.0	06:00:27.95	+31:30:39.71	G180.92+04.5	06:05:48.75	+30:25:11.40
G181.16+04.3	06:05:31.15	+30:06:33.65	G181.42-03.7	05:34:46.40	+25:44:48.16
G181.71+04.1	06:06:03.83	+29:32:54.89	G181.88+04.4	06:07:48.53	+29:33:27.39
G182.02-00.1	05:49:42.48	+27:07:10.01	G182.04+00.4	05:51:59.62	+27:23:47.47
G182.54-25.3	04:23:04.85	+12:13:03.09	G185.29-02.2	05:49:08.92	+23:13:41.99

Table C2: continue.

Source Name	R.A. (hh:mm:ss)	Decl. (dd:mm:ss)	Source Name	R.A. (hh:mm:ss)	Decl. (dd:mm:ss)
G188.04-03.7	05:49:52.71	+20:08:09.75	G190.08-13.5	05:19:28.71	+13:15:43.32
G190.15-14.3	05:16:45.83	+12:45:44.57	G190.17-13.7	05:18:44.25	+13:02:43.23
G190.50-02.2	06:00:19.46	+18:43:31.95	G191.03-16.7	05:10:23.30	+10:45:03.71
G191.51-00.7	06:08:02.75	+18:35:43.91	G192.12-10.9	05:32:55.83	+12:57:08.60
G192.28-11.3	05:31:43.36	+12:35:44.79	G192.54-11.5	05:31:28.55	+12:15:22.39
G192.94-03.7	06:00:08.12	+15:53:50.85	G194.69-16.8	05:17:37.50	+07:43:26.85
G194.80-03.4	06:05:04.24	+14:25:43.04	G194.94-16.7	05:18:26.83	+07:34:38.62
G196.21-15.5	05:25:17.29	+07:10:11.87	G196.65+13.9	07:13:49.08	+20:37:45.73
G198.03-15.2	05:29:45.07	+05:46:55.24	G198.96+01.4	06:30:41.93	+13:03:55.51
G201.26+00.4	06:31:36.70	+10:34:48.62	G201.84+02.8	06:41:11.23	+11:09:07.32
G202.21-09.1	05:59:02.91	+05:12:05.39	G202.58-08.7	06:01:25.31	+05:06:09.99
G203.00-03.6	06:19:58.41	+07:06:23.11	G203.11-08.7	06:02:25.08	+04:38:39.70
G203.57-30.0	04:47:58.28	-05:56:06.84	G203.75-08.4	06:04:20.98	+04:11:17.07
G204.82-13.8	05:47:22.03	+00:42:34.83	G205.29-06.0	06:16:00.65	+04:00:29.07
G205.42-08.1	06:08:40.02	+02:53:24.34	G205.57-08.2	06:08:37.14	+02:42:41.26
G206.05-08.3	06:09:06.85	+02:14:08.74	G206.21-08.4	06:09:11.90	+02:04:29.29
G206.34-08.5	06:08:54.46	+01:53:20.73	G206.54-14.4	05:48:27.03	-01:01:42.28
G206.60-14.4	05:48:46.44	-01:03:28.63	G206.87-04.3	06:24:47.70	+03:22:44.35
G208.56+02.3	06:51:55.20	+04:57:58.38	G209.20+02.1	06:52:12.86	+04:17:19.67
G210.01-20.1	05:34:10.53	-06:35:04.69	G210.30-00.0	06:46:30.11	+02:19:29.76
G210.67-36.7	04:34:00.52	-14:10:28.57	G210.89-36.5	04:35:10.69	-14:14:37.73
G211.70-12.1	06:05:47.39	-04:26:58.01	G213.92-13.6	06:04:31.04	-07:01:33.60
G214.21-13.4	06:05:46.53	-07:10:53.95	G214.69-19.9	05:42:43.77	-10:26:42.40
G215.41-16.3	05:56:57.94	-09:32:27.84	G215.70-15.0	06:02:20.00	-09:12:32.57
G215.88-17.5	05:53:22.51	-10:27:04.58	G215.92-15.3	06:01:43.10	-09:31:03.11
G216.01-15.9	05:59:35.96	-09:51:42.95	G216.32-15.7	06:00:58.21	-10:01:42.75
G216.51-13.8	06:08:00.58	-09:24:24.66	G216.69-13.8	06:08:18.64	-09:33:37.84
G216.76-16.0	06:00:25.70	-10:33:36.89	G217.13-12.5	06:13:57.69	-09:21:40.44

Appendix D: The spectral lines of DCO⁺, DCN, H¹³CO⁺ and H¹³CN 1-0

The spectra of deuterated molecules (black lines) and the spectra of ¹³C-isotopologue counterparts (red lines) are presented in the following figures, grouped by HCO⁺ and HCN respectively.

Figures D1~D3 show the spectral lines of DCO⁺ 1-0. Figure D1 displays the spectra for 8 sources where DCO⁺ 1-0 was detected using the low velocity resolution mode (AROWS mode 3), but H¹³CO⁺ 1-0 was not observed. Figure D2 presents spectra for 5 sources with DCO⁺ 1-0 detections and no H¹³CO⁺ 1-0 detections using the low velocity resolution mode (AROWS mode 3). Figure D3 shows spectra for 12 sources with DCO⁺ 1-0 detections and no H¹³CO⁺ 1-0 detections using the high velocity resolution mode (AROWS mode 13).

Figures D4~D6 show the spectral lines of DCN 1-0. Figure D4 shows spectra for 2 sources with DCN 1-0 detection and no H¹³CN 1-0 observation using the low velocity resolution mode (AROWS mode 3). Figure D5 shows spectra for 5 sources with DCN 1-0 detections but without H¹³CN 1-0 detections using the low velocity resolution mode (AROWS mode 3). Figure D6 presents spectra for 2 sources with DCN 1-0 detections and no H¹³CN 1-0 detections using the high velocity resolution mode (AROWS mode 13).

Figure D7 displays the spectral lines of H¹³CO⁺ 1-0, with 11 sources showing H¹³CO⁺ 1-0 detections but without DCO⁺ 1-0 detections with the high velocity resolution mode (AROWS mode 13).

Figures D8 and D9 show the spectral lines of H¹³CN 1-0. Figure D8 shows spectra for 16 sources with H¹³CN 1-0 detections but no DCO⁺ 1-0 detections using the low velocity resolution mode (AROWS mode 3). Figure D9 shows spectra for 6 sources with H¹³CN 1-0 detections and no DCN 1-0 detections using the high velocity resolution mode (AROWS mode 13).

Figures D10 and D11 show the spectral lines of both DCO⁺ and H¹³CO⁺ 1-0. Figure D10 shows spectra for 66 sources with detections of both DCO⁺ and H¹³CO⁺ 1-0 using the low velocity resolution mode (AROWS mode 3). Figure D11 displays spectra for 46 sources with detections of both species using the high velocity resolution mode (AROWS mode 13). Due to errors in the Doppler tracking with mode 13, H¹³CO⁺ 1-0 lines were manually aligned with DCO⁺ 1-0 lines in Figure D11.

Figures D12 and D13 show the spectral lines of DCN and H¹³CN 1-0. Figure D12 includes spectra for 4 sources with both DCN and H¹³CN 1-0 detections using the low velocity resolution mode (AROWS mode 3). Figure D13 presents spectra for 7 sources with both detections using the high velocity resolution mode (AROWS mode 13). Due to errors in the Doppler tracking with mode 13, H¹³CN 1-0 lines were manually aligned with DCN 1-0 lines in Figure D13.

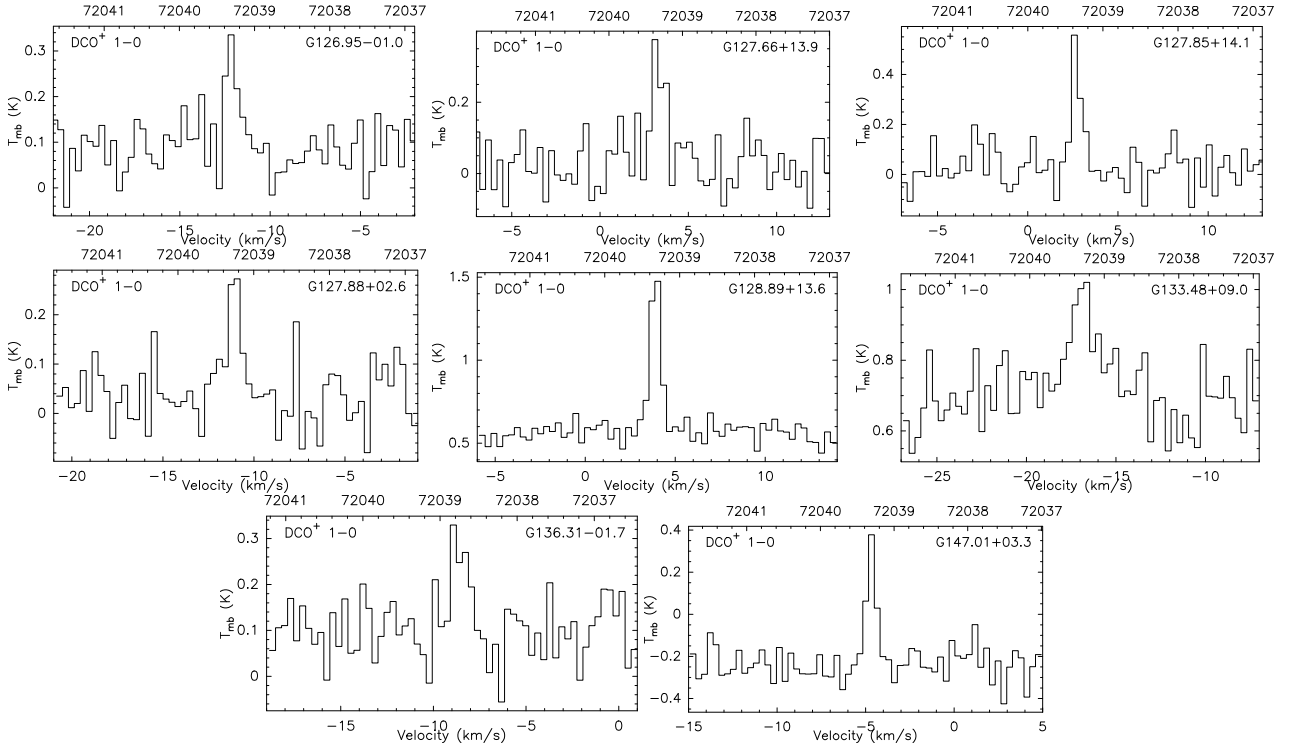


Fig. D1: Line profiles of DCO⁺ 1-0 with the low velocity resolution mode (AROWS mode 3). The transitions of H¹³CO⁺ 1-0 have not been observed in these sources.

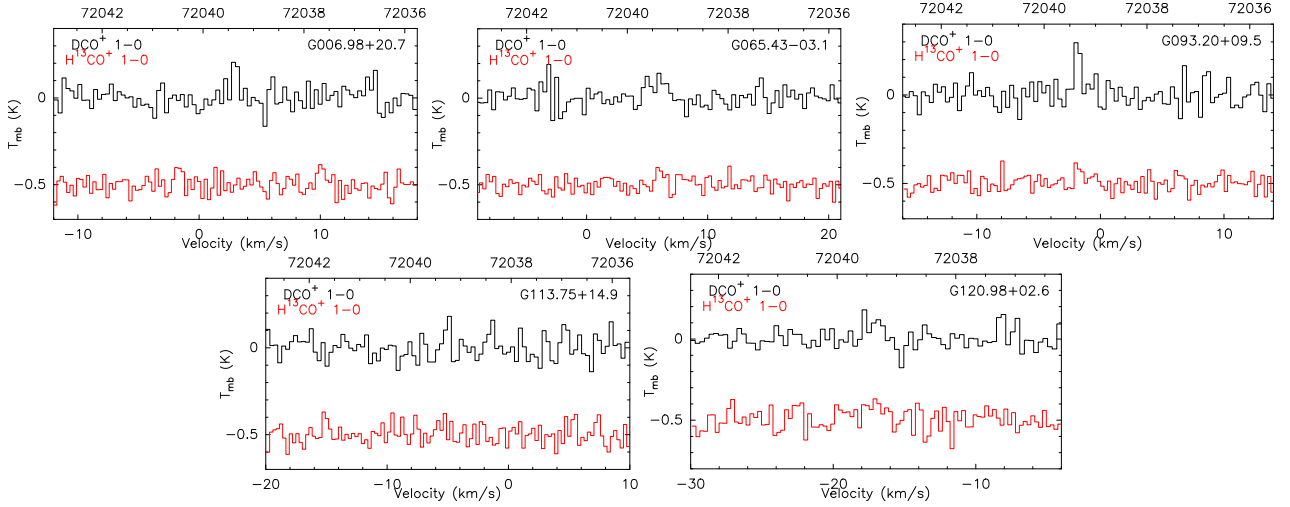


Fig. D2: Line profiles of DCO⁺ 1-0 with the low velocity resolution mode (AROWS mode 3). The transitions of H¹³CO⁺ 1-0 have been observed but not detected in these sources.

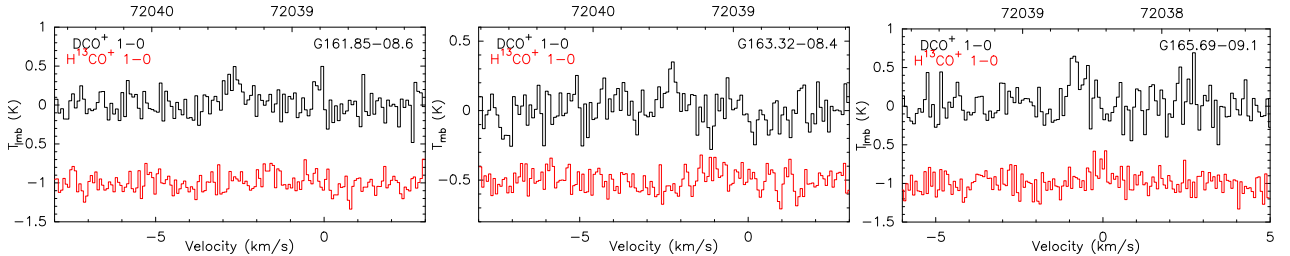


Fig. D3: Line profiles of DCO⁺ 1-0 with the high velocity resolution mode (AROWS mode 13). The transitions of H¹³CO⁺ 1-0 have been observed but not detected in these sources.

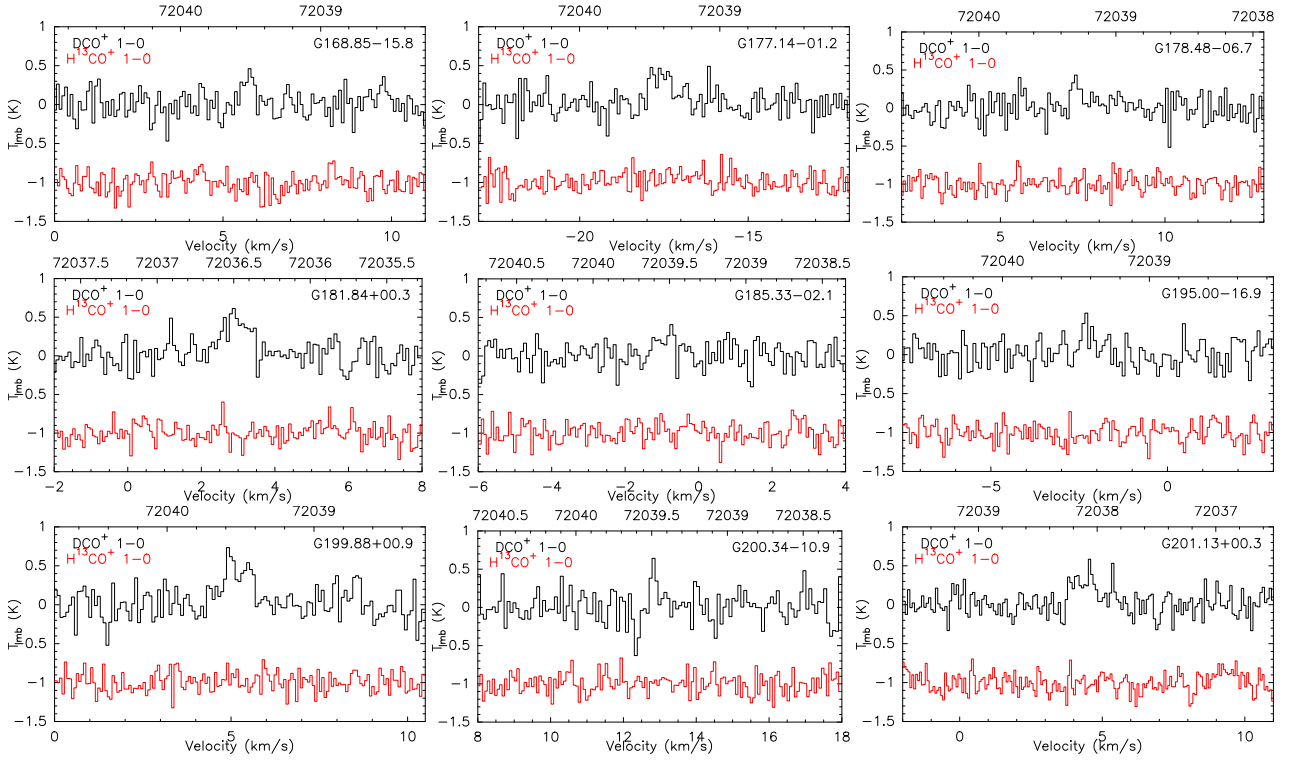
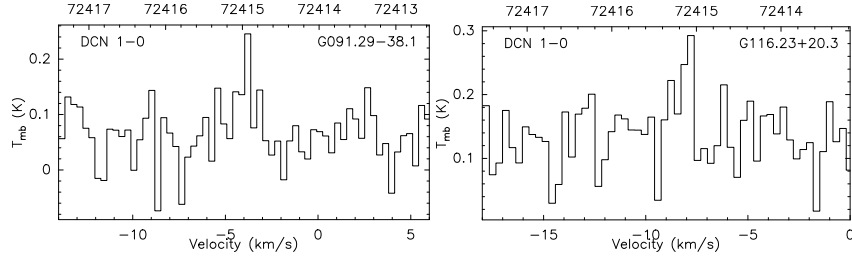
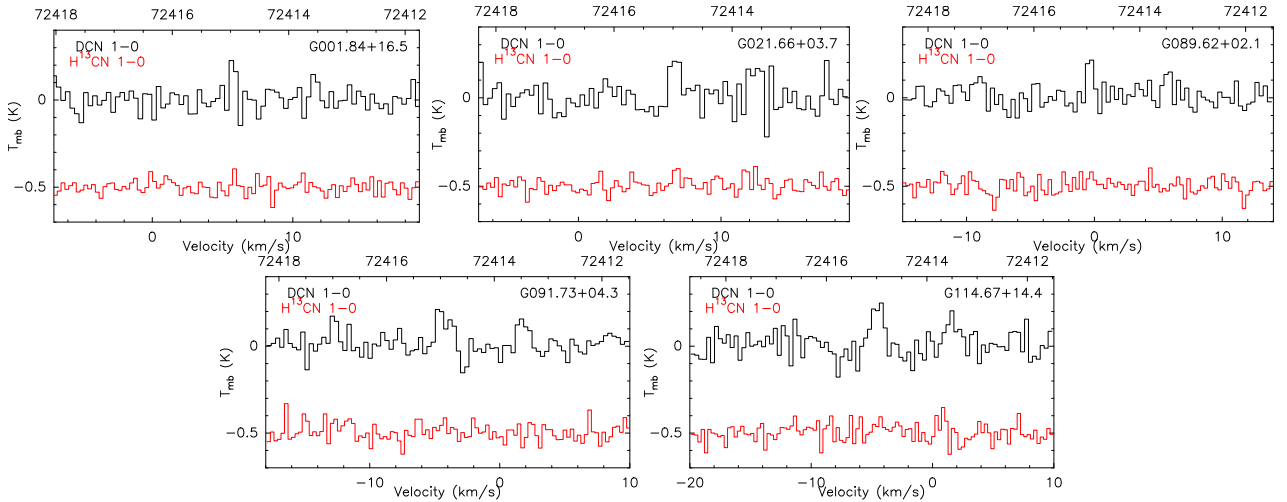


Fig. D3: Continued.


Fig. D4: Line profiles of DCN 1-0 with the low velocity resolution mode (AROWS mode 3). The transitions of H^{13}CN 1-0 have not been observed in these sources.

Fig. D5: Line profiles of DCN 1-0 with the low velocity resolution mode (AROWS mode 3). The transitions of H^{13}CN 1-0 have been observed but not detected in these sources.

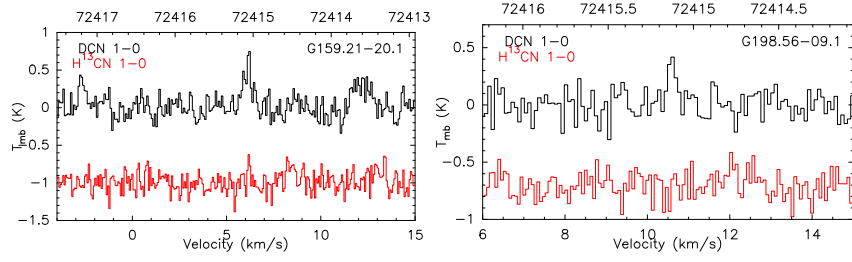


Fig. D6: Line profiles of DCN 1-0 with the high velocity resolution mode (AROWS mode 13). The transitions of H¹³CN 1-0 have been observed but not detected in these sources.

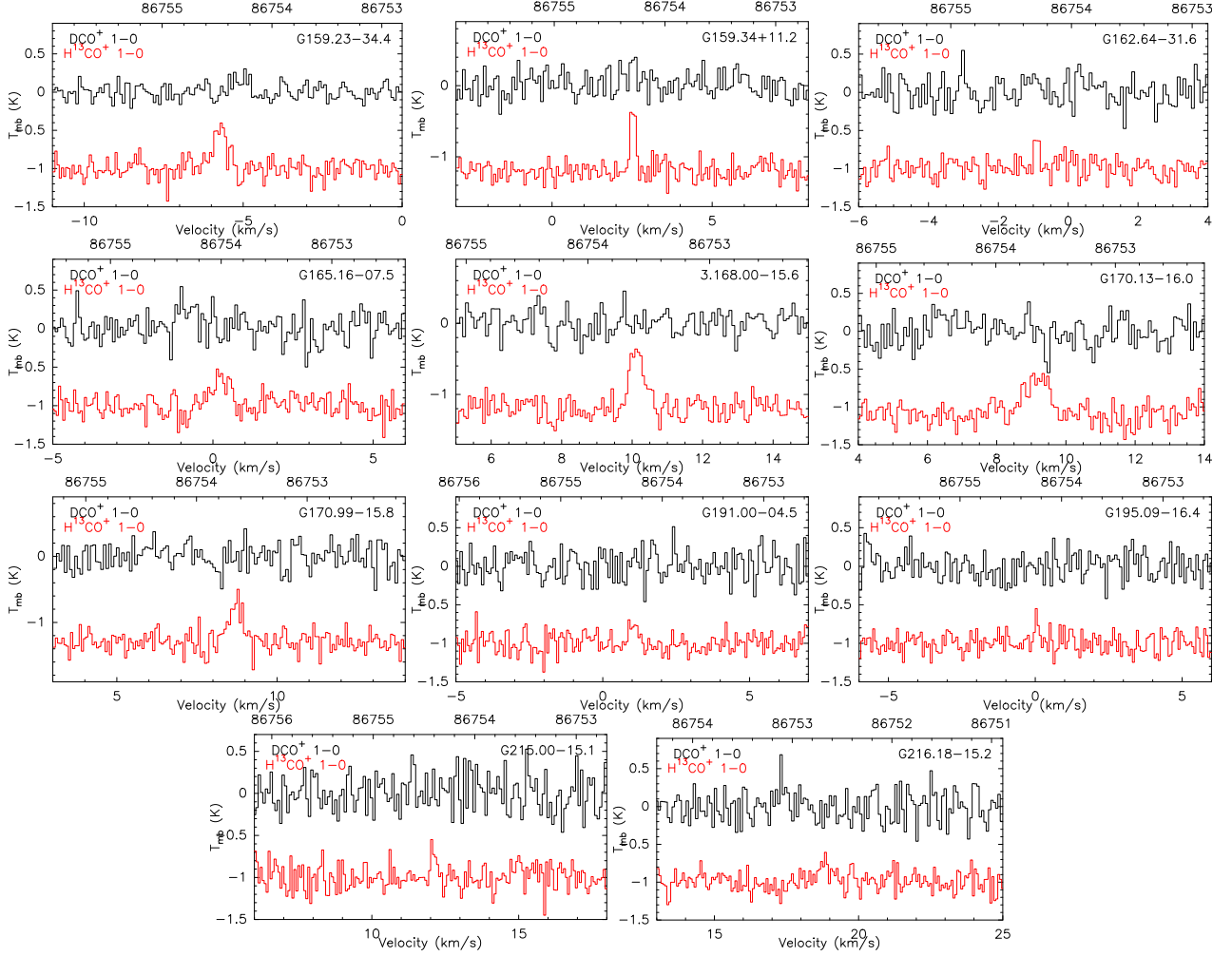


Fig. D7: Line profiles of H¹³CO⁺ 1-0 with the high velocity resolution mode (AROWS mode 13). The transitions of DCO⁺ 1-0 have been observed but not detected in these sources.

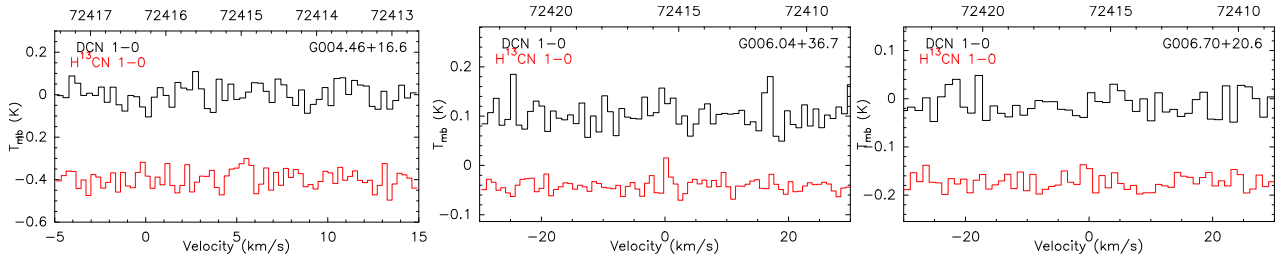


Fig. D8: Line profiles of H¹³CN 1-0 with the low velocity resolution mode (AROWS mode 3). The transitions of DCN 1-0 have been observed but not detected in these sources.

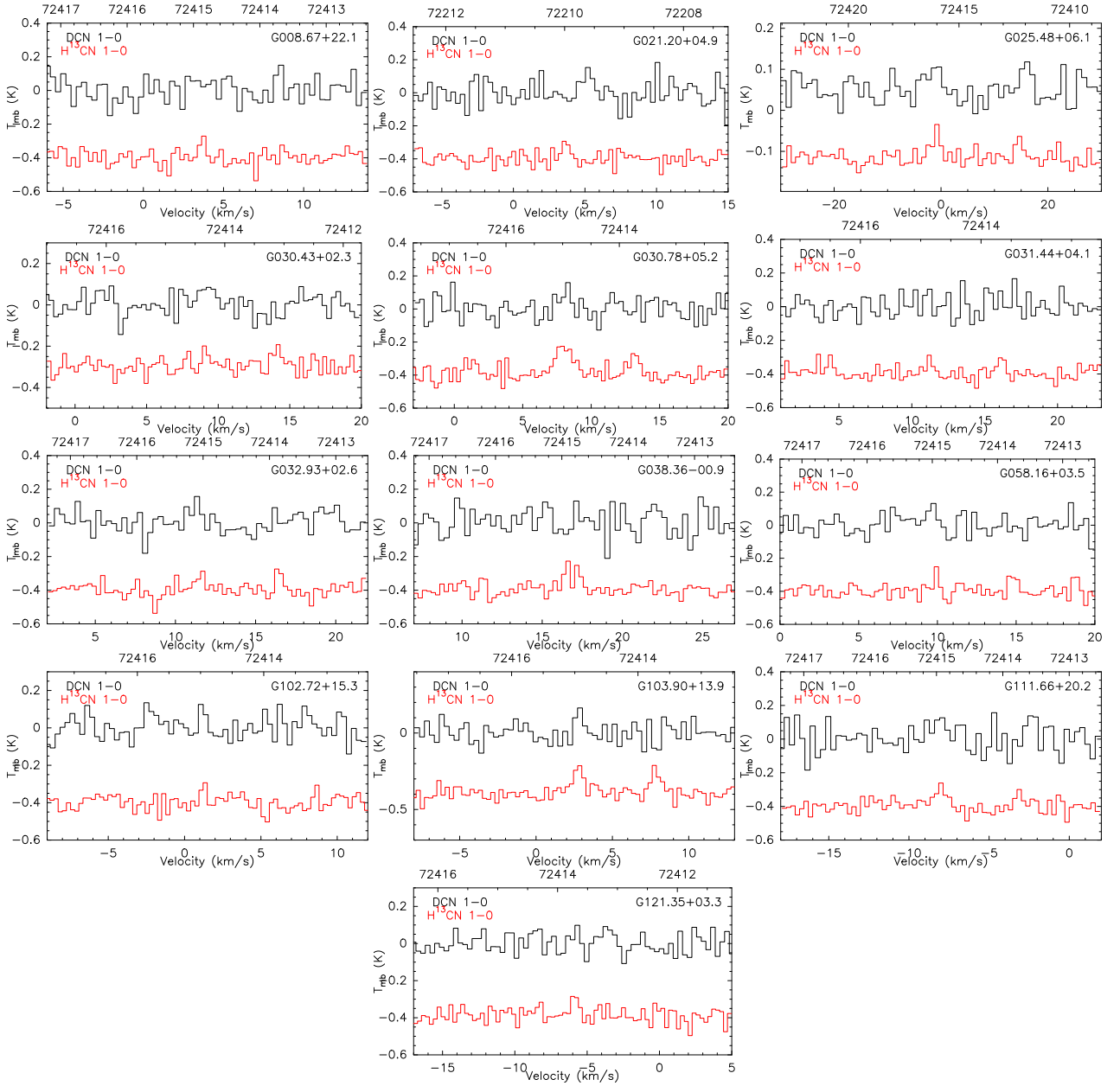


Fig. D8: Continued.

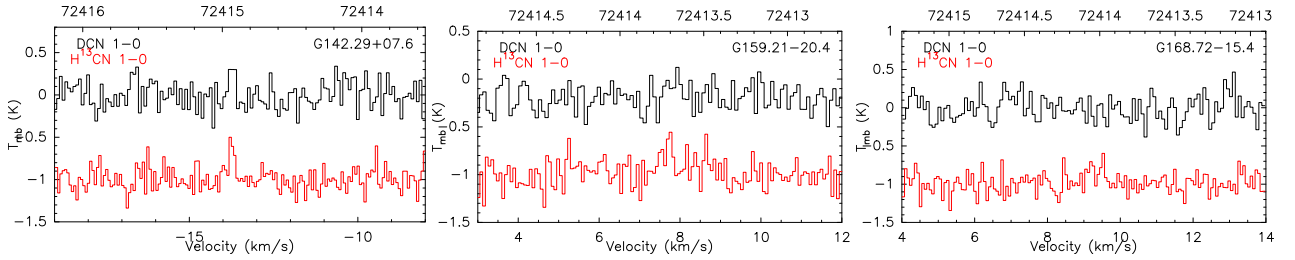


Fig. D9: Line profiles of H^{13}CN 1-0 with the high velocity resolution mode (AROWS mode 13). The transitions of DCN 1-0 have been observed but not detected in these sources.

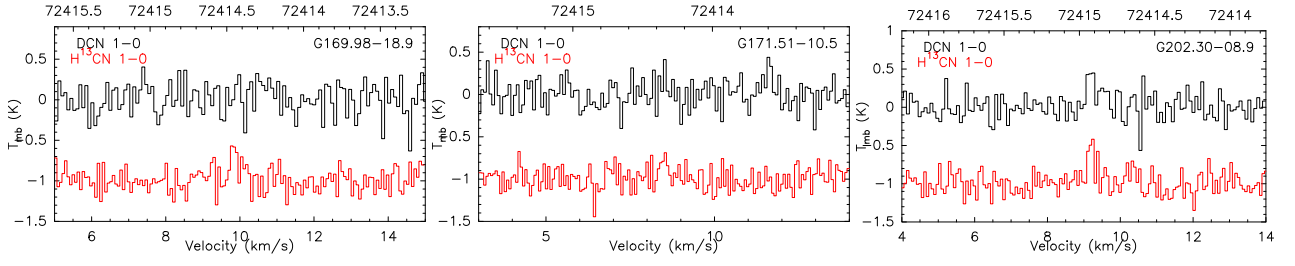
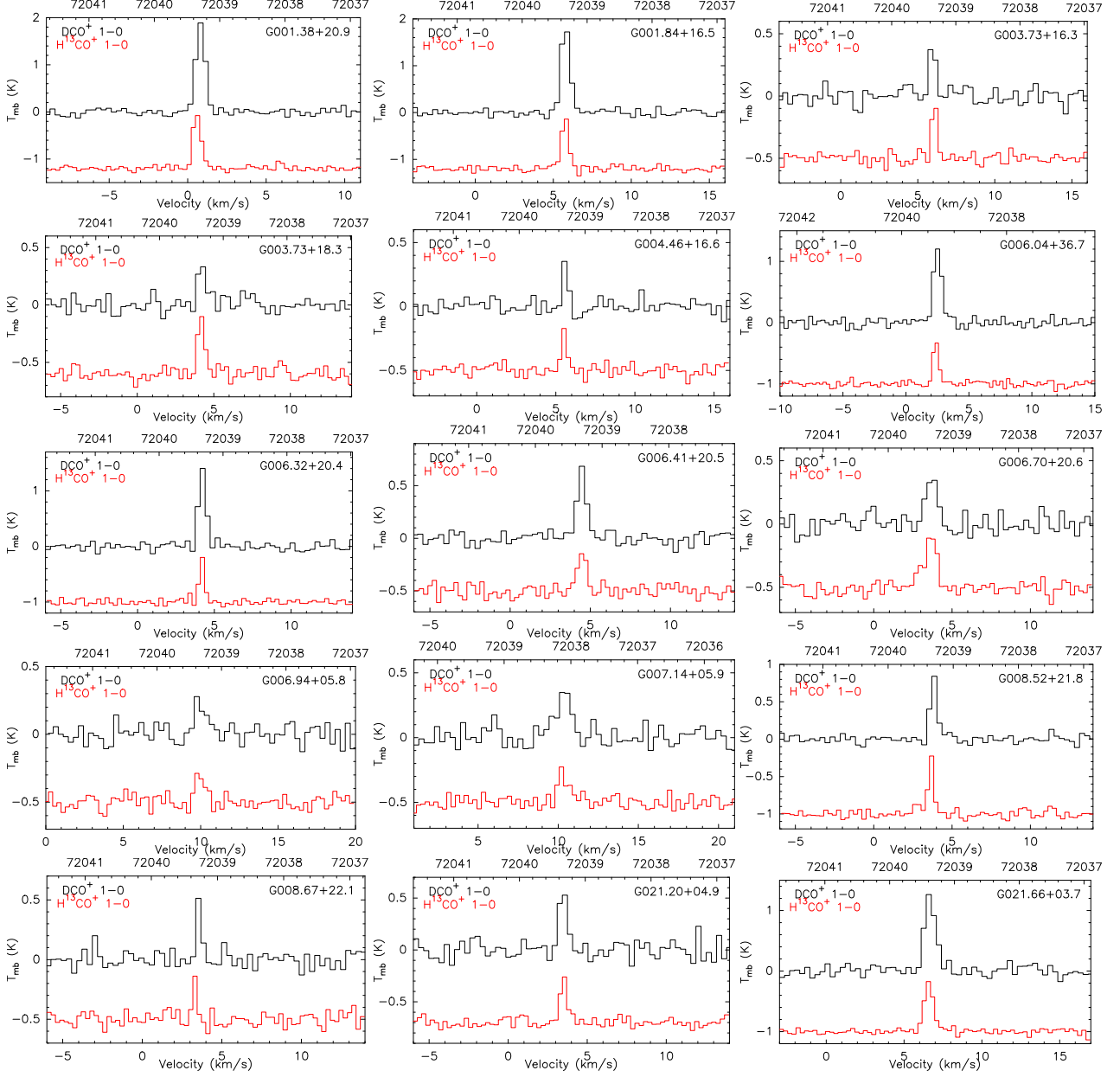


Fig. D9: Continued.


Fig. D10: Line profiles of DCO⁺ and H¹³CO⁺ 1-0 with the low velocity resolution mode (AROWS mode 3).

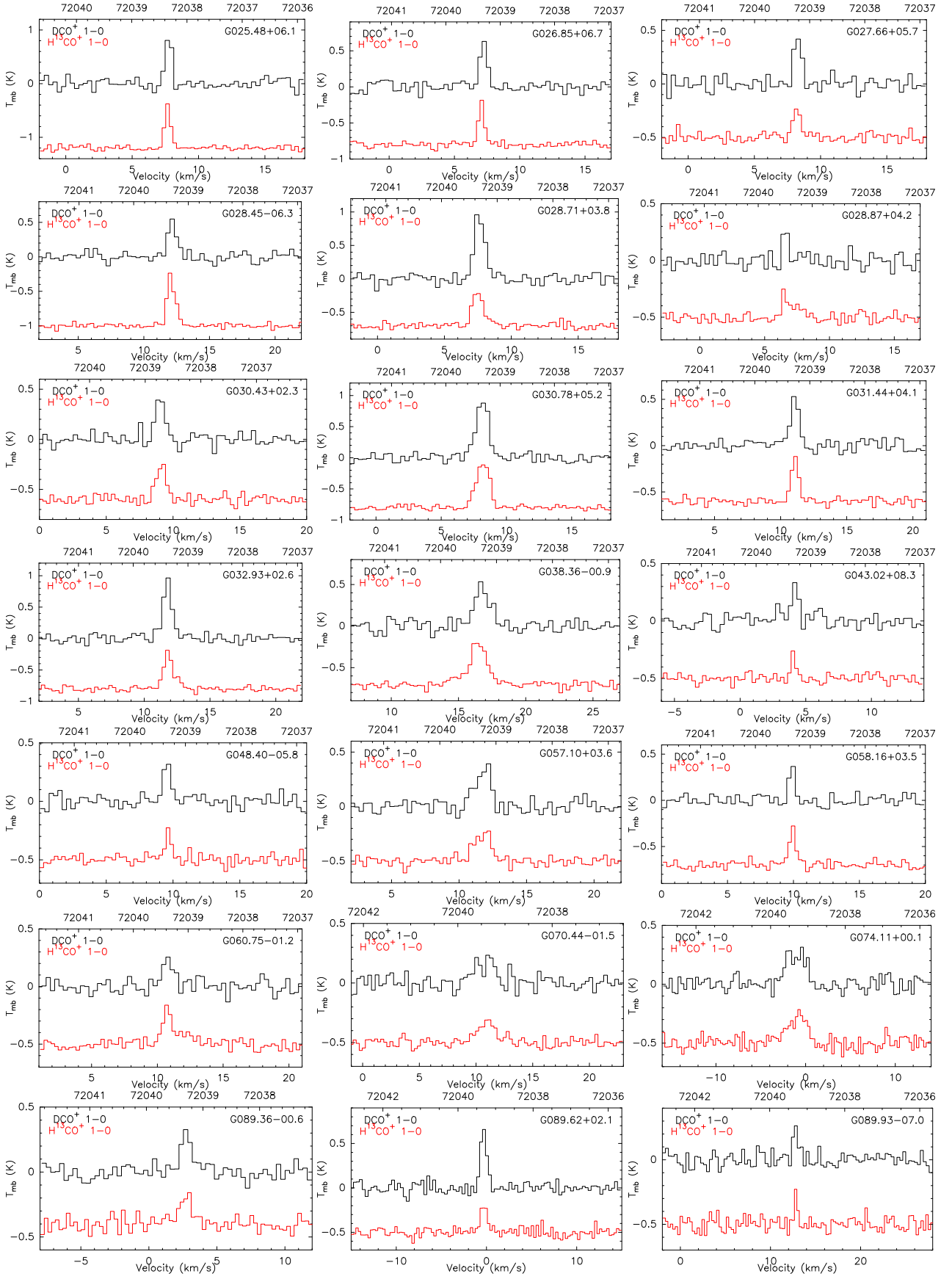


Fig. D10: Continued.

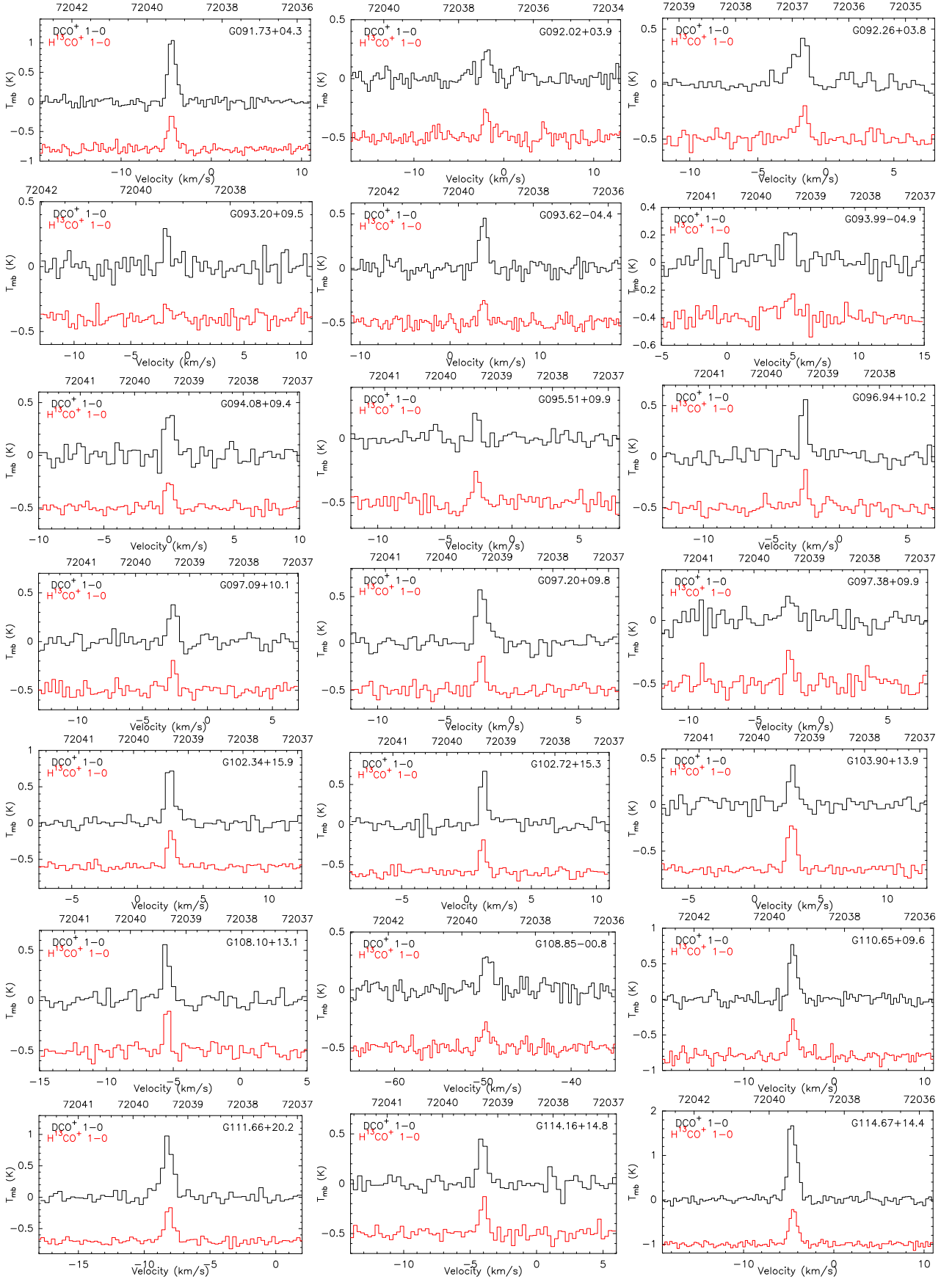


Fig. D10: Continued.

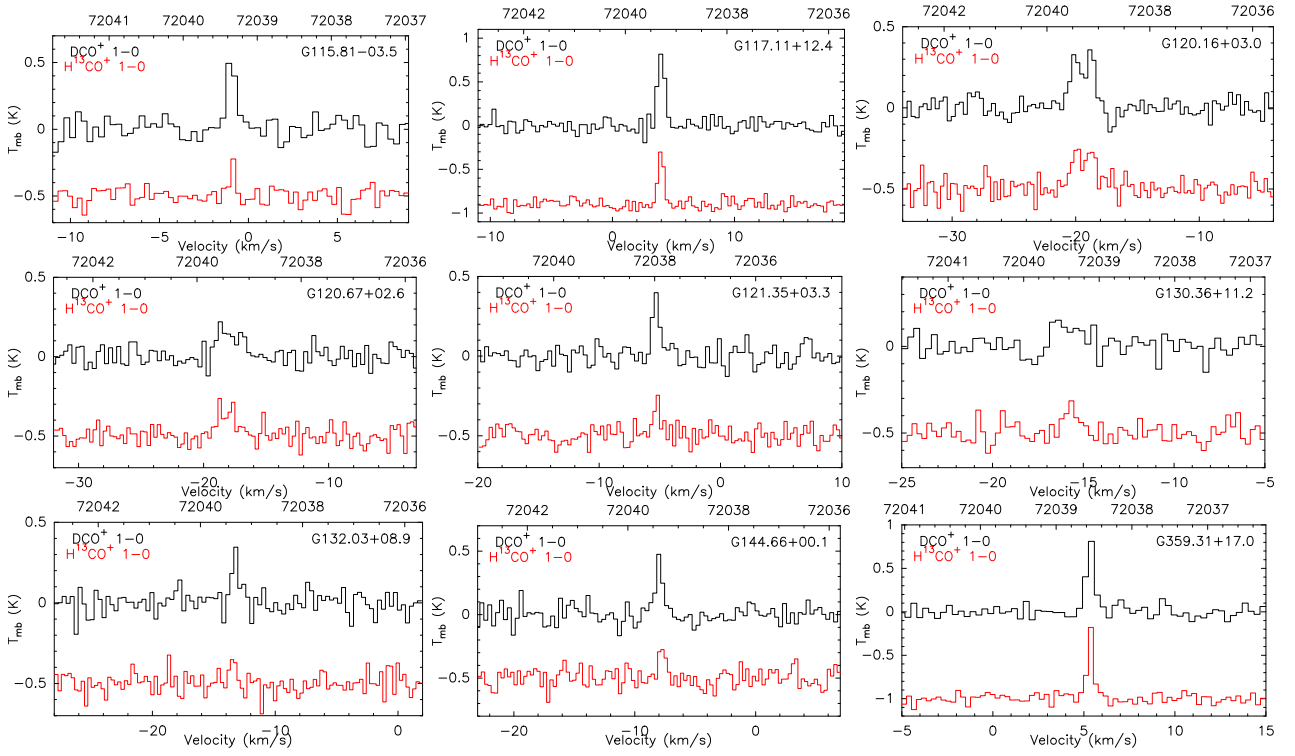


Fig. D10: Continued.

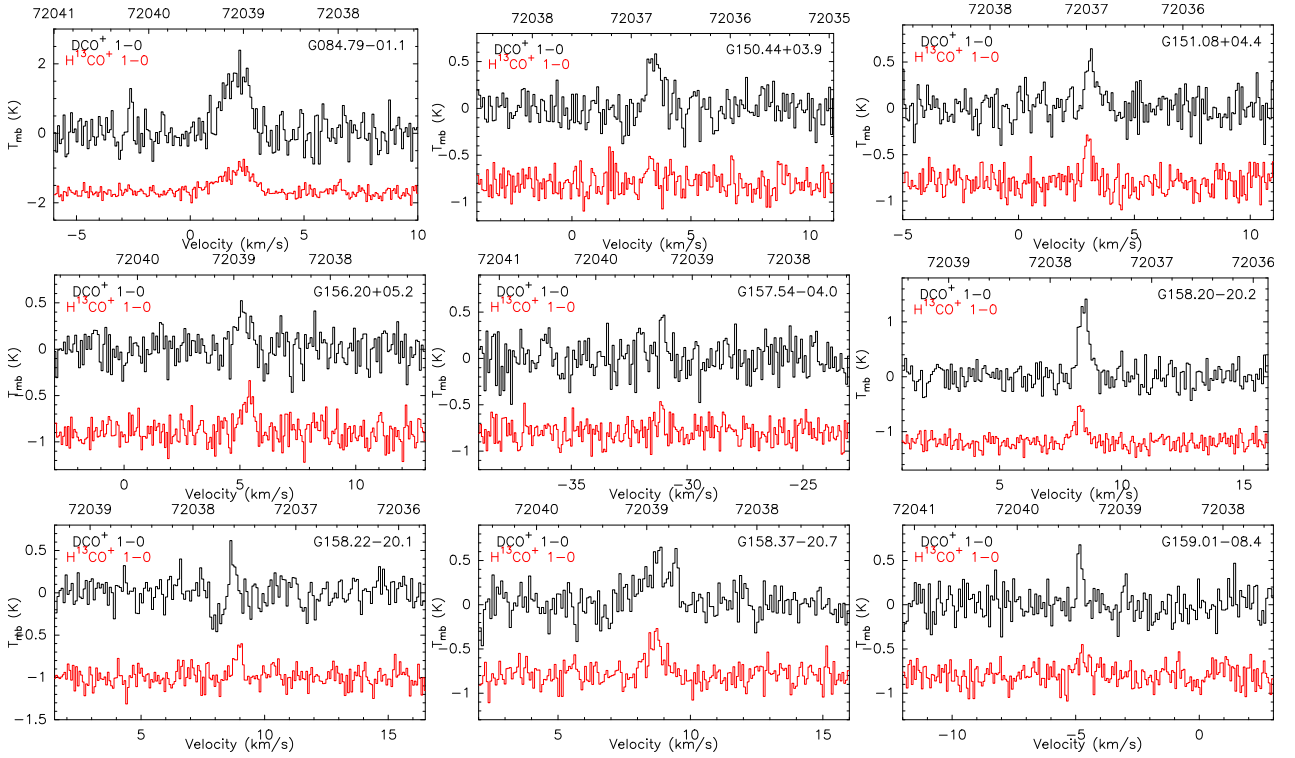


Fig. D11: Line profiles of DCO⁺ and H¹³CO⁺ 1-0 with the high velocity resolution mode (AROWS mode 13). H¹³CO⁺ 1-0 lines were manually aligned with DCO⁺ 1-0 lines, due to errors in the Doppler tracking.

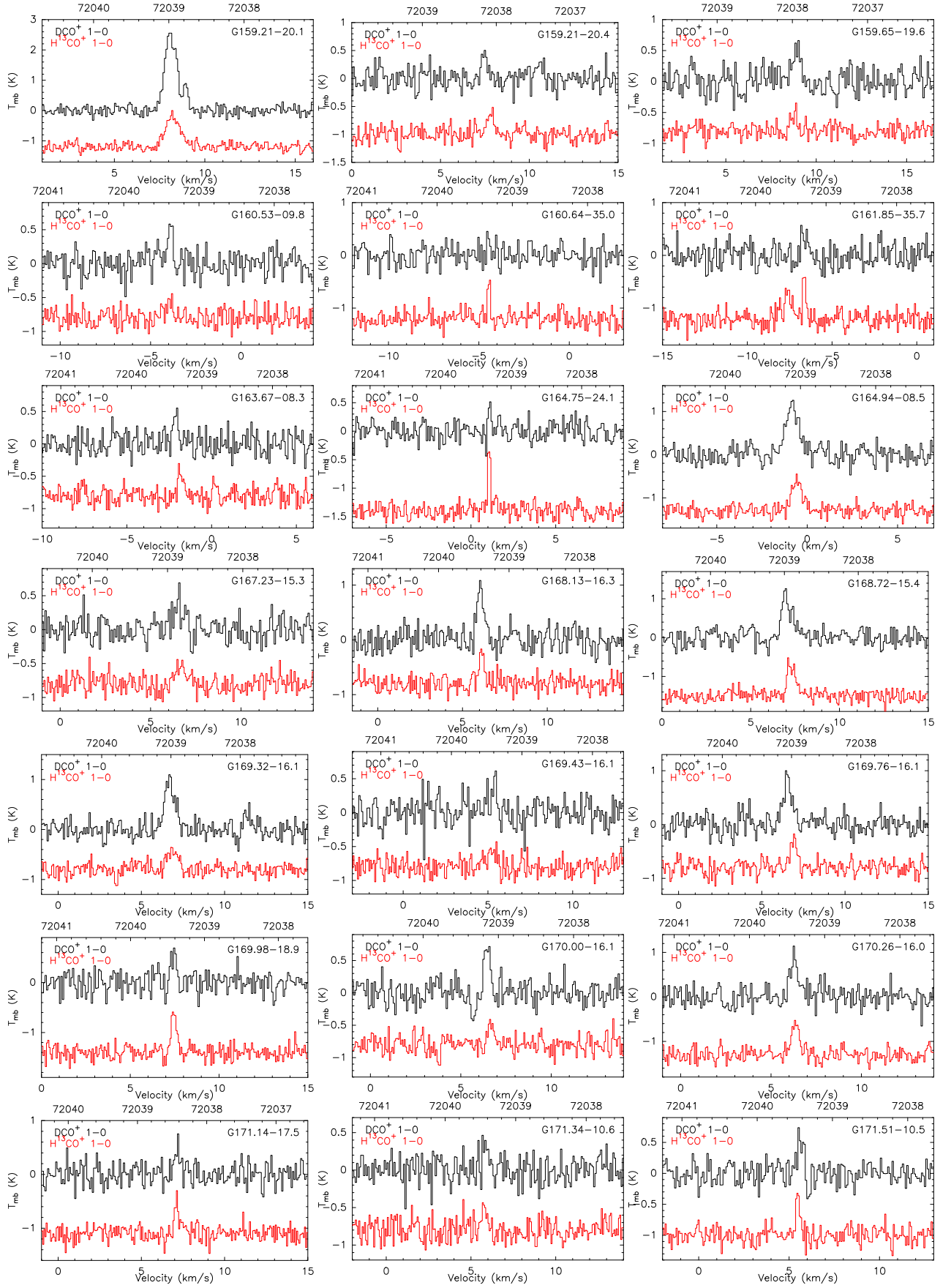


Fig. D11: Continued.

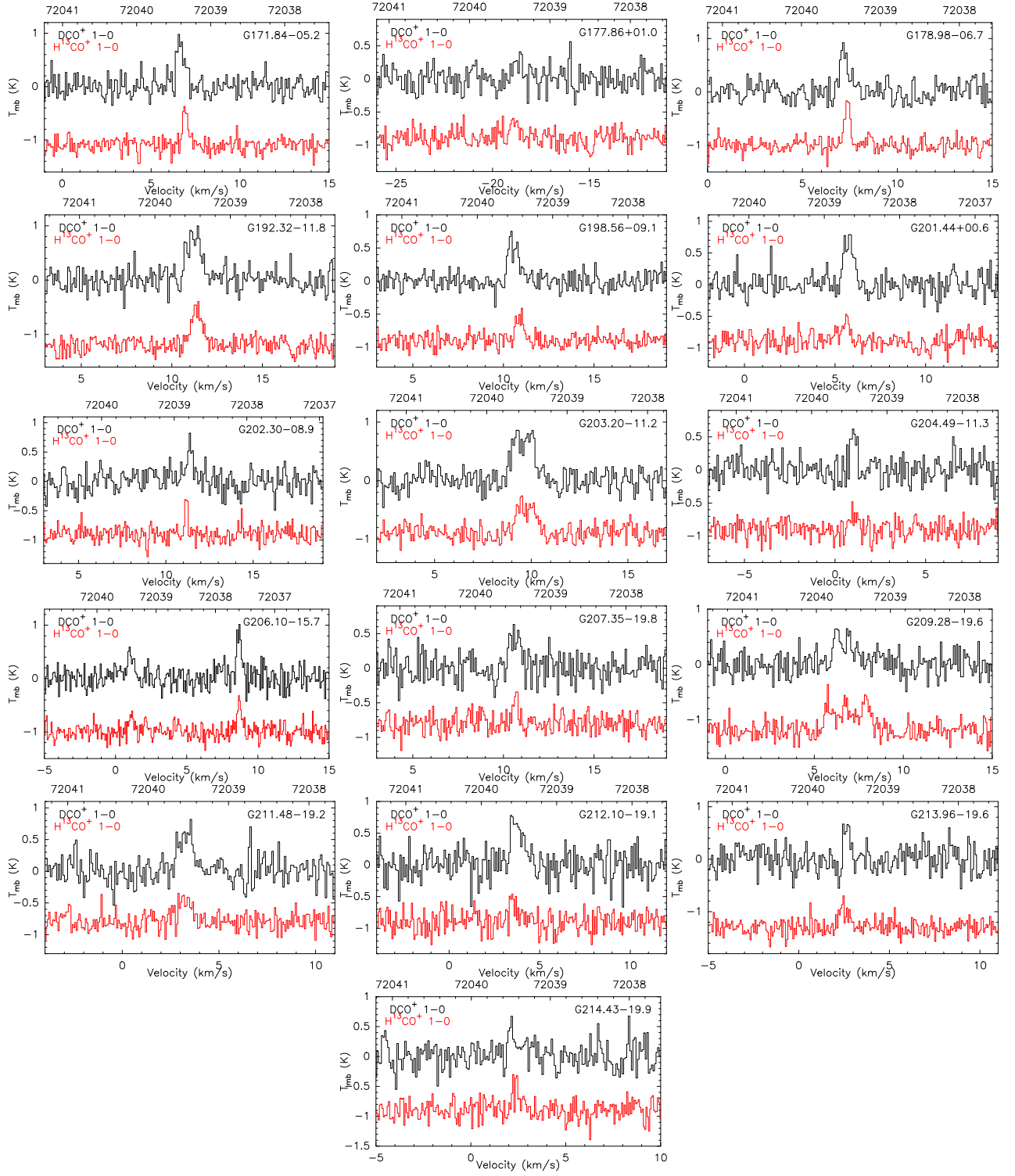


Fig. D11: Continued.

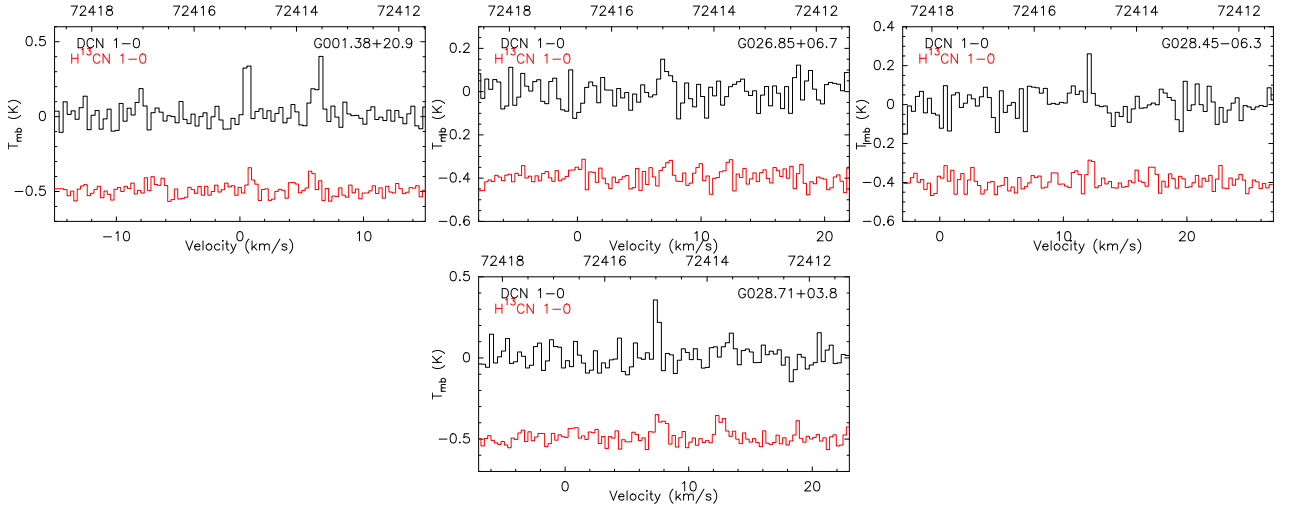


Fig. D12: Line profiles of DCN and H¹³CN 1-0 with the low velocity resolution mode (AROWS mode 3).

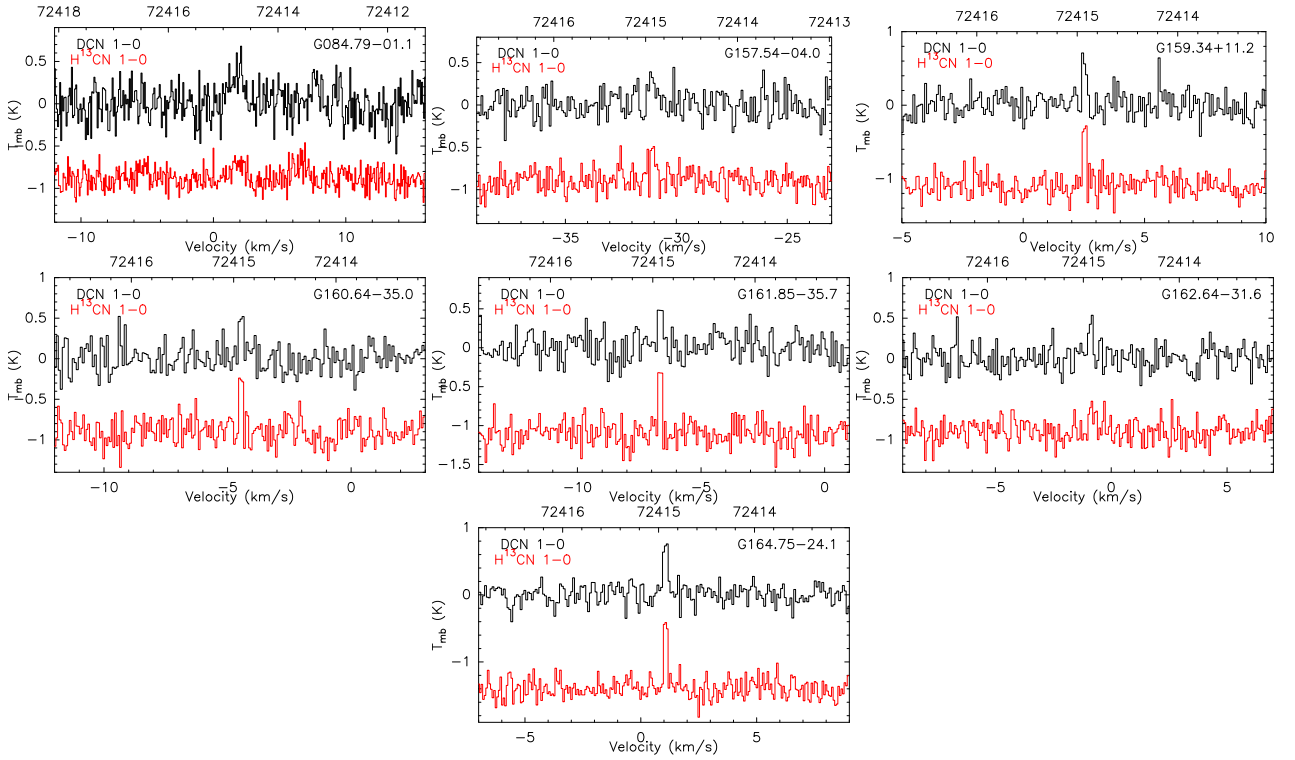


Fig. D13: Line profiles of DCN and H¹³CN 1-0 with the high velocity resolution mode (AROWS mode 13). H¹³CN 1-0 lines were manually aligned with DCN 1-0 lines, due to errors in the Doppler tracking.